

RENSIT:

RadioElectronics. NanoSystems. Information Technologies

Journal "Radioelectronics. Nanosystems. Information Technologies" (short RENSIT) publishes original articles, reviews and brief reports, not previously published, on topical problems in **radioelectronics (including biomedical) and fundamentals of information, nano- and biotechnologies and adjacent areas of physics and mathematics.**

Designed for **researchers, graduate students, physics students of senior courses and teachers.**

It turns out **2 times a year** (that includes 2 issues)

Authors of journal are academicians, corresponding members and foreign members of Russian Academy of Natural Sciences (RANS) and their colleagues,

as well as other russian and foreign authors on presentation of their manuscripts by the members of RANS, which can be obtained by authors before sending articles to editors.

And also after its receiving - on recommendation of a member of editorial board of journal, or another member of Academy of Natural Sciences, that gave her opinion on article at request of editor.

The editors will accept articles in both **Russian and English** languages.

Articles are internally peer reviewed (**double-blind peer review**) by members of the Editorial Board.

Some articles undergo external review, if necessary.

Journal RENSIT is included in the **DB SCOPUS, EBSCO Publishing**, in the international abstracts database - **Ulrich's International Periodicals Directory**, (USA, New York, <http://www.ulrichsweb.com>), in the **AJ and DB VINITI RAS** (<http://www.viniti.ru>), and DB **Russian Science Citation Index (RSCI)** http://elibrary.ru/project_risc.asp).

Full-text content is posted in the DB of the **Russian Scientific Electronic Library** - information resource on the Internet <http://elibrary.ru> and is available for registered users.

On journal's website <http://www.rensit.ru> posted metadata publications and **RENSIT - English version** (cover-to-cover translation) of journal, which is a party to **CrossRef**.

The founder - the **Russian Academy of Natural Sciences**
Publisher - Publishing Center of the Russian Academy of Natural Sciences
Publisher Address: 119002 Moscow, per. Sivtsev Vrazhek 29/16

CONTENTS

RADIOELECTRONICS

PHYSICAL BASES AND PRINCIPLES OF CONSTRUCTION OF FRACTAL RADARS AND FRACTAL SENSORS: A NEW DIRECTION – FRACTAL ANALYSIS AND ITS APPLICATION IN THE THEORY OF STATISTICAL SOLUTIONS AND IN STATISTICAL RADIO ENGINEERING

Alexander A. Potapov 129

CREATION AND TESTING OF A FOUR-CHANNEL INSTALLATION FOR TESTING AT A MODERN EXPERIMENTAL LEVEL OF DISCUSSION KOZYREV ASTRONOMICAL OBSERVATIONS

Stepan N. Andreev, Alexander V. Voropinov, Dmitrii Yu. Tsipenyuk ... 139

ATOMIC PHYSICS

ATOM IN A STRONG MAGNETIC FIELD. TRANSFORMATION OF ATOMS TO TRANSATOMS

Gennady V. Mishinsky 147

CONTINUUM PHYSICS

RELATIVISTIC CONTINUUM IN SPECIFIED FORCE FIELD

Stanislav A. Podosenov, Alexander A. Potapov, Jaykov Foukzon, Elena R. Men'kova 161

NANOSYSTEMS

PRINTER TECHNOLOGIES IN ELECTRONICS. MATERIALS AND DEVICES FOR PRINTING – FIRST RUSSIAN SEMINAR (Moscow, December 15, 2017)

Denis Yu. Kornilov, Sergey V. Tkachev, Evgeny V. Zaitsev, Vitaly P. Kim, Alexey E. Kushnir 181

INFORMATION TECHNOLOGIES

OBJECT-ORIENTED LOGIC PROGRAMMING OF 3D INTELLIGENT VIDEO SURVEILLANCE SYSTEMS: THE PROBLEM STATEMENT

Alexei A. Morozov, Olga S. Sushkova, Alexander F. Polupanov 205

NUMERICAL MODELING OF THE PROCESS OF DETECTION OF KARST CAVITIES IN RAILWAY EMBANKMENTS BY A GRID-CHARACTERISTIC METHOD

Vladimir S. Egiyan, Alina V. Favorskaya, Aram A. Mkrtchyan, Igor B. Petrov, Nikolay I. Khokhlov, Vasilii I. Golubev 215

FRACTALS IN PHYSICS

LIGHT DIFFRACTION BY FRACTALS: COMPARISON OF EXPERIMENTAL DATA WITH THE OBTAINED BY NUMERICAL METHODS FOURIER IMAGES OF THE OBJECT PICTURES

Galina V. Arzamastseva, Mikhail G. Evtikhov, Feodor V. Lisovsky, Ekaterina G. Mansvetova 221

CHRONICLE

GRAFENIKA. RUSSIAN GUBIN'S SEMINAR (MOSCOW)

Vladimir I. Grachev 230



RUSSIAN ACADEMY
OF NATURAL SCIENCES

DEPARTMENT OF
RADIOELECTRONICS,
NANOPHYSICS AND
INFORMATION TECHNOLOGIES
PROBLEMS

RENSIT:

**RADIOELECTRONICS.
NANOSYSTEMS.
INFORMATION
TECHNOLOGIES.**
2017, VOL. 9, № 2

FOUNDED IN 2009
2 ISSUES PER YEAR
MOSCOW

Editor-in-Chief

VLADIMIR I. GRACHEV
grachev@cplire.ru

Deputy Chief

ALEXANDER S. ILUSHIN

Deputy Chief

SERGEY P. GUBIN

Executive Secretary

ROSTISLAV V. BELYAEV
belyaev@cplire.ru

EDITORIAL BOARD

Anatoly V. Andreev
Oleg V. Betzkiy
Vladimir A. Bushuev
Vladimir A. Cherepenin
Alexander S. Dmitriev
Yuri K. Fetisov
Yaroslav A. Ilushin
Anatoly V. Kozar
Vladimir V. Kolesov
Albina A. Kornilova
Vladimir A. Makarov
Andrey I. Panas
Igor B. Petrov
Alexander A. Potapov
Vyacheslav S. Rusakov
Alexander S. Sigov
Valentine M. Silonov
Eugeny S. Soldatov
Lkhamsuren Enkhtur (Mongolia)
Yoshiyuki Kawazoe (Japan)
Kairat K. Kadyrzhanov (Kazakhstan)
Peter Paul Mac Ken (USA)
Andre Skirtach (Belgium)
Eugeny V. Ushpuras (Republic
of Lithuania)
Enrico Verona (Italy)

ISSN 2414-1267 online

The journal is registered by the Ministry of Telecom
and Mass Communications of the Russian Federation.
Certificate El. no. FS77-60275 on 19.12.2014

All rights reserved. No part of this publication
may be reproduced in any form or by any means
without permission in writing from the publisher.

©RANS 2017

EDITORIAL BOARD ADDRESS
218-219 of, 7 b., 11, Mokhovaya str.,
125009 MOSCOW, RUSSIAN FEDERATION
TEL. +7 495 629 3368
FAX +7 495 629 3678 FOR VLADIMIR I. GRACHEV

PHYSICAL BASES AND PRINCIPLES OF CONSTRUCTION OF FRACTAL RADARS AND FRACTAL SENSORS: A NEW DIRECTION - FRACTAL ANALYSIS AND ITS APPLICATION IN THE THEORY OF STATISTICAL SOLUTIONS AND IN STATISTICAL RADIO ENGINEERING

Alexander A. Potapov

Kotel'nikov Institute of Radioengineering and Electronics, Russian Academy of Science, <http://cplire.ru>
11-7, Mokhovaya str., Moscow 125009, Russian Federation

Joint-Laboratory of JNU-IRE RAS

601, Huangpu Avenue, JiNan University, Guangzhou, 510632, China

potapov@cplire.ru

Abstract: Fast development of the fractal theory in radar and radio physics led to establishing of the new theoretical direction in modern radar. It can be described as «Statistical theory of fractal radar». The new kind and approach of up-to-date radiolocation: fractal-scaling or scale-invariant radiolocation has been proposed. The main ideas and strategic directions in synthesis of fundamentally new topological radar detectors of low-contrast objects have been considered. The new topologic signs and methods of detection of low-contrast objects against the background of high-intensity noise are presented. The methods are based on the textural and fractal analysis and also on the theory of deterministic chaos. The main purpose of the work is to interpret the main directions of radio physics, radio engineering and radio location in “fractal” language that makes new ways and generalizations promising radio systems in future. The author raised the foregoing problems as early as in 1980 and for more than 35 years he has been successfully working on their solution and development.

Keywords: texture, fractal, lacunarity, signals detector, low-contrast target, radar, fractal-frequency MIMO-systems, statistical radio engineering

UDC 537.86:519.22

Bibliography – 34 references

RENSIT, 2017, 9(2):129-138

Received 25.10.2017

DOI: 10.17725/rensit.2017.09.129

CONTENTS

1. INTRODUCTION (129)
 2. FRACTAL-SCALING OR SCALE-INVARIANT RADIOLOCATION AND FRACTAL MIMO-RADARS (130)
 3. INNOVATIVE FRACTAL-SCALING TECHNOLOGIES: CREATION, DEVELOPMENT AND APPLICATION OF FRACTAL METHODS FOR RADIOLOCATION TASKS (131)
 4. NEW FEATURES AND TOPOLOGICAL METHODS FOR THE DETECTION OF LOW-CONTRAST TARGETS AGAINST THE BACKGROUND OF HIGH-INTENSITY NOISE (131)
 5. FRACTAL TOPOLOGICAL DETECTORS OF LOW-CONTRAST TARGETS IN HIGH-INTENSITY NOISE (133)
 6. A NEW DIRECTION IN THE THEORY OF STATISTICAL SOLUTIONS AND IN STATISTICAL RADIO ENGINEERING (134)
 7. CONCLUSION (135)
- REFERENCES (136)

1. INTRODUCTION

Radar detection of low observable and small objects near the surface of the earth and the sea, as well as at meteorological precipitation is an extremely difficult problem [1, 2]. In addition, sea and vegetation clutters are of non-stationary and multiscale character, especially at θ shallow angles. A variety of underlying coverings, radar observation conditions and following the above mentioned objects very often lead to the fact that the signal-to-noise ratio q_0^2 for such problems almost always fills the area of negative values (in decibels), i.e., $q_0^2 < 1$ dB [1, 2].

This makes classical radar detection methods and detection algorithms inapplicable in most cases, that is, use of energy detectors (when the likelihood ratio is determined solely and only by

the received signal energy) becomes essentially impossible.

What is to be done? There is a way! Detection of low-contrast targets against the background of mentioned above high-intense natural noise inevitably requires to offer, and then calculate some fundamentally new characteristic that is different from the functional related to noise and signal energy, and is determined by the topology and the dimension of the received signal.

Introduction of the concepts "texture", "deterministic or dynamic chaos", "fractal" and "fractal dimension" to the scientific use in radio physics and radiolocation, enabled the author to be the first to offer and then apply new dimension and topological (not energy!) characteristics (invariants), which the author combined under the general concept "sampling topology" [1-12].

The work objective is to give a brief analytical review of the development and improvement of the author's methods and algorithms for new topological, including fractal textural detectors of low-contrast radar targets against the background of high-intense ground and sea clutters, as well as meteorological precipitation ones.

2. FRACTAL-SCALING OR SCALE-INVARIANT RADIOLOCATION AND FRACTAL MIMO-RADARS

For further instantiation of the problems of detection of weak radar signals, we believe initial information to come from a variety of radio systems in the form of a one-dimensional signal and/or a radar image (RI) – Fig. 1.

The simplified scheme of primary radiosystems and investigation of radar image and one-dimensional signal in millimeter wave band (MWB) were represented by the author much earlier. Currently, fractal radar, a MIMO-radar and a fractal MIMO radar as well as unmanned aerial vehicles (UAVs) are added to the scheme in Fig. 1. The concept of fractal radar is presented in [1-5, 8, 11, 12], the concept

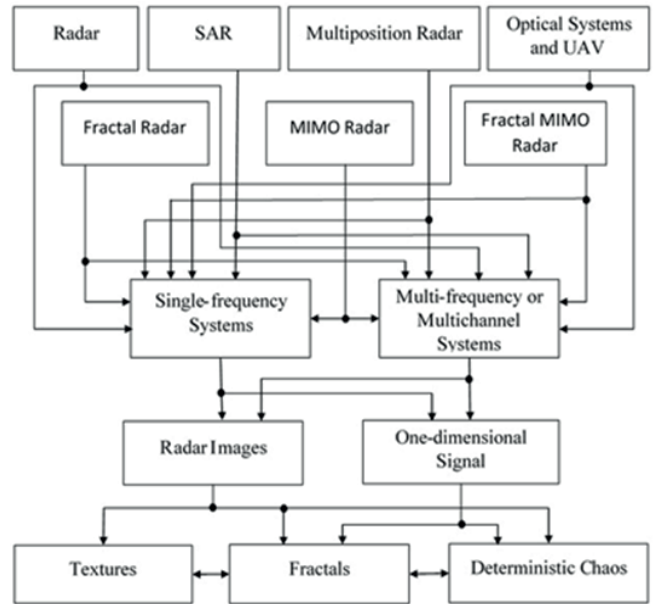


Fig. 1. Radio systems of initial information.

of fractal MIMO-radar is considered in [1-3, 5, 11, 12].

In general, the technology of MIMO systems implies that each wireless device involved in data exchange, has several spatially distributed receiving and transmitting antennas. The basic idea of fractal MIMO-radars is using fractal antennas and fractal detectors [1-12]. The capability of fractal antennas to work on several frequencies simultaneously or to radiate broadband sounding signal provides a sharp increase in the number of degrees of freedom that defines many of the important advantages of

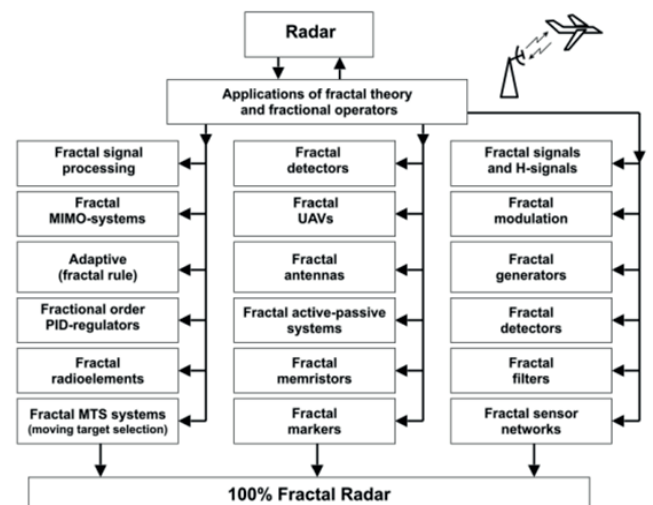


Fig. 2. A fractal radar.

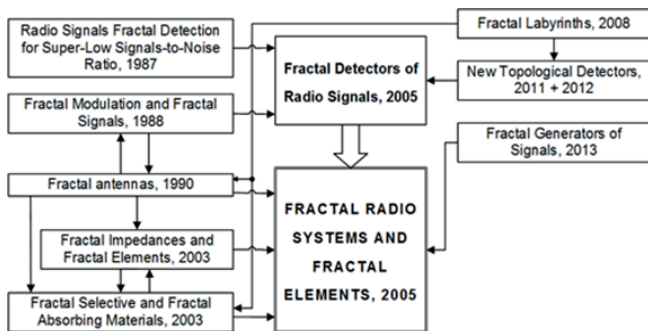


Fig. 3. Fractal radio systems.

this type of radiolocation and significantly expands adaptation possibilities.

To represent these specifics, in [1-3, 5, 11, 12] a new term "fractal-frequency MIMO systems (FF MIMO)" was introduced, which reflects their physical properties much better. MIMO technologies related to the spatial multi-channel systems provide great opportunities for the application of the author's global fractal-scaling method for signal processing, various algorithms and technologies of fractal detectors [1-12] at all stages of the synthesis of information MIMO systems. The idea of a fractal radar station (Fig. 1 and 2) is based on the concept of fractal radio systems developed by the author - Fig. 3 [4, 8, 9].

3. INNOVATIVE FRACTAL-SCALING TECHNOLOGIES: CREATION, DEVELOPMENT AND APPLICATION OF FRACTAL METHODS FOR RADIOLOCATION TASKS

During 35 years of research, the developed global fractal-scaling method completely lived up to expectations having found numerous applications (Fig. 4). This is a challenge of time.

4. NEW FEATURES AND TOPOLOGICAL METHODS FOR THE DETECTION OF LOW-CONTRAST TARGETS AGAINST THE BACKGROUND OF HIGH-INTENSITY NOISE

All currently existing and used by the author methods and topological features of low observable objects detection against the

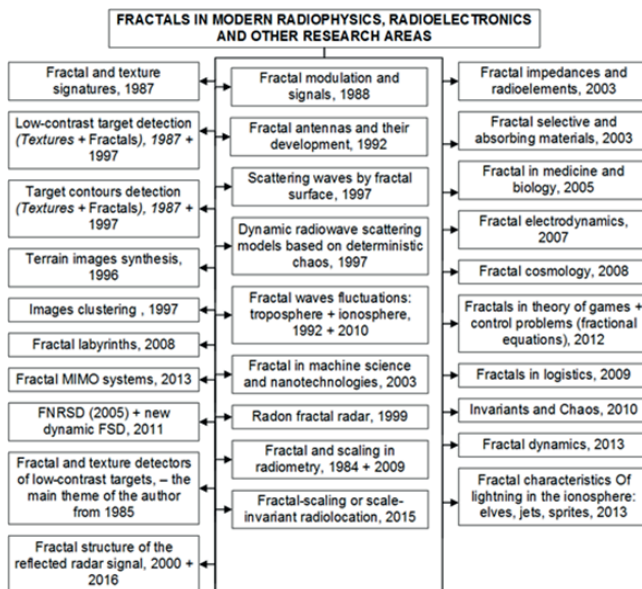


Fig. 4. The layout of the author's development of new information technologies based on fractals, fractional operators and scaling effects for nonlinear physics and electronics.

background of the high-intensity sea, ground and meteorological phenomena clutters are compactly represented in Fig. 5. The relationship

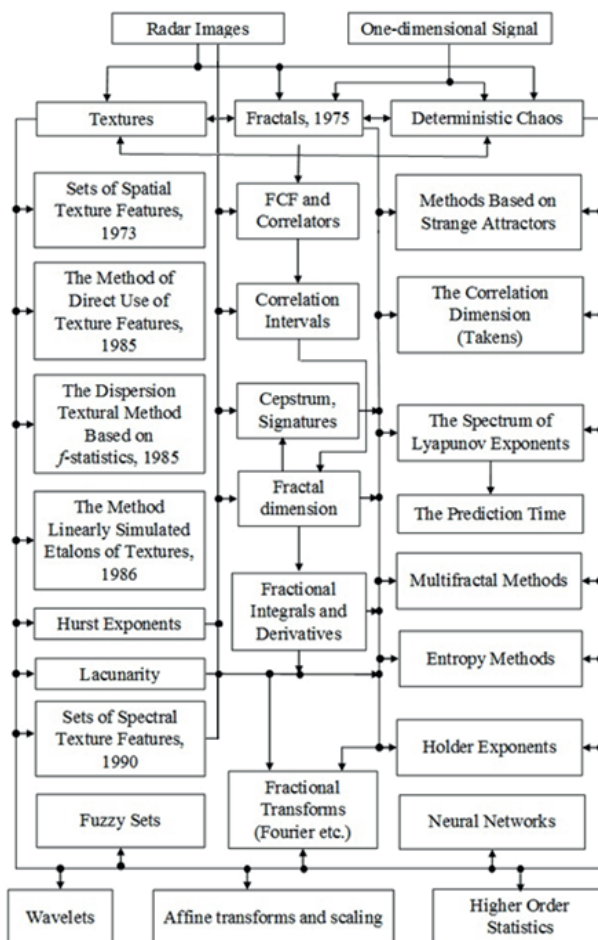


Fig. 5. Topological features and methods for detection of low-contrast targets against the background of high-intense noise.

between a variety of features and methods are also marked there. The work on the classification of such methods, algorithms and features started in May 2015 in China during the defense of the project "Leading Talents of Guangdong Province" and finished at the beginning of 2016 in China.

Introduction of the concept of textural features ensemble to the US in 1973 [13], in the 1980-ies made it possible for the author to be the first to calculate complete ensembles of 28 textural features and to conduct their detailed synchronic analysis for real objects (optical aerial photography (OAP) and radar images within MMW range at a wavelength of 8.6 mm), as well as for synthesized textures based on autoregressive models, depending on the season [1, 2, 4].

Long-term field experiments were carried out by the author in cooperation with "Almaz" CCB and other leading industrial organizations of the USSR. All investigations were performed at wavelengths $\lambda = 2.2$ and 8.6 mm (active radiation) and $\lambda = 3.5$ mm (passive radiation). When extracting a MMW signal scattered by a variety of land covers, back in 1985 the author conducted first experiments on sorting areas of frequency and time scaling, the presence of which imply certain fractal properties of the accepted sampling. At the same time, the problem of calculating textural features with account for the drift of their signatures under alternation of seasons was posed and solved. The assessments of the impact of window sizes on the accuracy of determining textural features for images of different land cover types were optimized.

For a long time the works on the study of radar images of the land cover at MMW using textural information have actually been carried out only in Russia and are of interest so far (especially now) [1, 2, 4]. After calculating ensembles of textural features based on optical and radar images, in 1985-1986 the author proposed methods and algorithms for

the detection of low-contrast targets against the background of high-intense noise. Those included the method of direct use of textural features (1985), the dispersion method based on f-statistics (1985) and a detection method using linearly simulated patterns, i.e. textures (1986) [1-4, 8, 11]. The created methods of detection are quite valid at low signal to noise ratio of the order of or less than one (times). To the author's knowledge, no textural method for detecting low-contrast target has been proposed abroad. Moreover, an important advantage of the textural methods of processing is the possibility to neutralize speckles at coherent images of the Earth's surface, obtained by SAR.

The methods of deterministic chaos are widespread; they are shown in the right column of Fig. 5. It should be only noted that the algorithms of radar detection of low-contrast targets against the background of woodlands for the radar at a wavelength of 2.2 mm were tested by the experimenters in 2001. It was the first time when a strange attractor was reconstructed. It controlled the radar scattering of millimeter radio waves. Its dynamic and geometric characteristics were measured; D fractal dimensions, depending on the value of m embedding dimension were calculated as well. The most accurate estimate of D can be obtained at the breakpoint of $D(m)$ convex curve, at that paying no attention to reduction in scale ratio above and below.

Based on the found maximum Lyapunov exponent $\lambda_1 > 0.6$ bit/s it has been shown that, when measuring the current conditions with an accuracy of up to 1 bit, we lose all predictive power over time during 1.7 seconds. Therefore, the prediction interval of echoed signal intensity is by about 8 times greater than classical correlation time τ ($\tau \approx 210$ ms at a wind speed of 3 m/sec). The prediction interval provides an opportunity to estimate roughly the amplitude of further samples in the sample collection and, as noted by the author, it can be

used in radar practice. Calculations of Hurst exponent H showed that in two out of three cases, the scattering process of millimeter waves by woodlands corresponds to the persistent process with $H > 0.5$, i.e. to the process with maximal rank.

5. FRACTAL TOPOLOGICAL DETECTORS OF LOW-CONTRAST TARGETS IN HIGH-INTENSITY NOISE

Currently, great interest is evinced in various fractal and scaling methods (Fig. 5). Those fractal investigations started almost simultaneously in Russia, the USA and China in the 1980s. [1-12]. And the global problem to detect a fractal object against the intensive fractal background with additive Gaussian and nongaussian noise and interference was once posed [1-12]. Distinguishing features and methodology of the author's approach differed so greatly and were unusual for that time, that it was followed by a number of foreign articles with references to his early works on fractal processing of signals and radar images (see, e.g., [14-16]), in which it was taken further.

At the same time, the fractal dimension D or its signature $D(t, f, r)$ in different parts of the surface image is also a corresponding texture measure, i.e. the spatial correlation properties of scattering of radio waves from the respective surface areas. Moreover, the texture also determines lacunarity Λ (Fig. 5), which uses second-order statistics for fractal images [1-12, 17-28]. Lacunarity is small for large dense texture and it is great when the texture is coarse-grained.

Lacunarity (Mandelbrot) is defined by the formula

$$\Lambda = \langle ((M / \langle M \rangle) - 1)^2 \rangle. \tag{1}$$

Here, M is a "mass" of a fractal formation, $\langle M \rangle$ is an anticipated "mass", and the brackets $\langle \dots \rangle$ stand for data ensemble averaging.

Lacunarity as a feature of objects detection was considered by the author in 1997. The

introduction of fractional measures and scaling invariant makes it necessary to work with power-series probability distributions. The basic principles of a fractal detector were discovered and offered as early as in the 1980s; and for the first time ever (Fig. 2 and 3) the operation of the working model of fractal nonparametric detector of radar signals (FNDRS) was performed in 2003-2005. [1-12, 17-28]. In 2005 in the US it was exhibited as part of ISTC project with CCB "Almaz" and IRE RAS and earned a very high opinion of experts [1, 2]. The authors proposed unconventional algorithms of fractal-scaling detection, which offered high resistance. Some original versions of generalized structures of radar fractal detectors are presented in Fig. 6. The schematic view of the conjectured detector is shown in Fig. 6a. Based on a received radio signal or an image, a set of textural and fractal features ξ is determined. Then, in the threshold device at the threshold value of T and a certain level of false alarm probability F , a decision on obtained signal H_1 or its lack H_0 is issued. As ξ features, the value of the fractal dimension

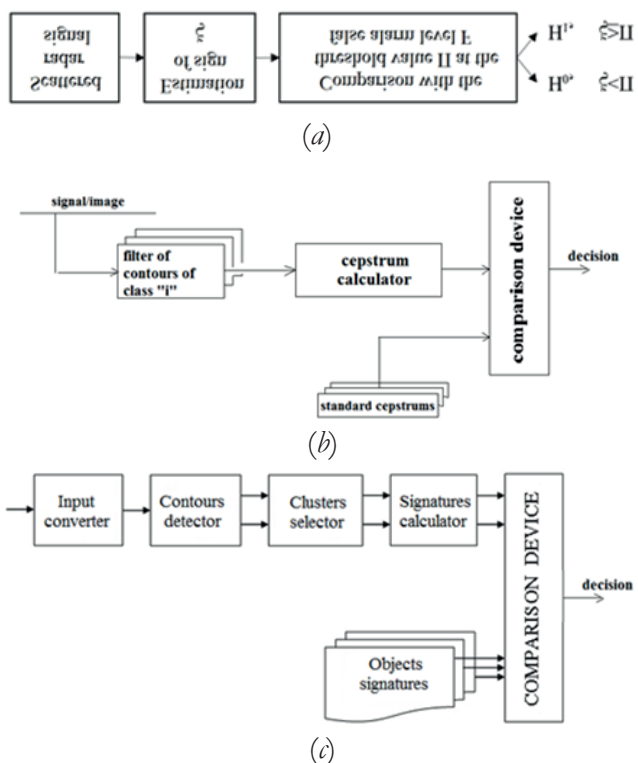


Fig. 6. The initial (a) and detailed (b, c) structures of the first fractal detectors.

D , Hurst exponents $0 \leq H \leq 1$ for multiscale surfaces, p -exponents, lacunarity values, etc. can be used. Hurst exponent is

$$H = 3 - D \tag{2}$$

for RI and

$$H = 2 - D \tag{3}$$

for a one-dimensional signal.

The integrated structural scheme of the fractal detector of radar signals is shown in Fig. 6b. It consists of a circuit filter and a *fractal cepstrum* computer. Further specification of the structural scheme of FNDRS is shown in Fig. 6c. An incoming signal (RI, a one-dimensional sample collection) arrives at the input converter.

Crucially, using the schemes in Fig. 6 it is definitely possible to synthesize absolutely all kinds of other fractal detectors in the future. For a long time (over 35 years) the priority in this area in Russia and over the world strictly belongs to V.A. Kotelnikov IRE of RAS and to the author in particular. The author's concept (Fig. 3) of fractal radio systems and fractal devices makes the synthesis of other types of fractal detectors possible (Fig. 7 and Fig. 8). The detector based on the Hurst exponent works by using one or more search frequencies of radar (Fig. 7).

Hurst exponent H reflects the irregularity of a fractal object. The smaller H exponent, the more irregular the fractal object is. So when an object occurs, the Hurst exponent grows. Fig. 8 is a scheme of a fractional detector with an autoregressive estimate of a power spectrum of the ground clutter. The autoregressive model is a linear prediction model that estimates the power spectrum of the clutter and forms its autocorrelation matrix.

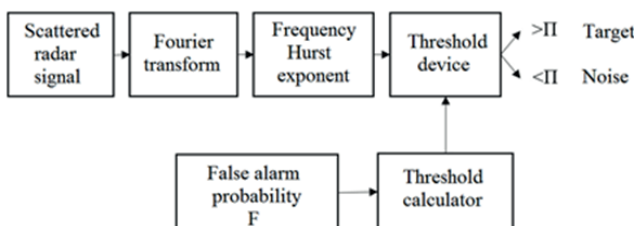


Fig. 7. A fractal detector on the basis of the Hurst exponent.

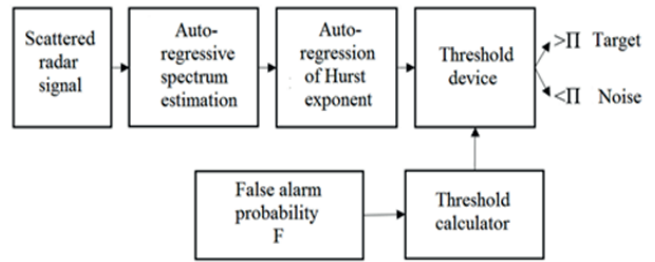


Fig. 8. A fractal detector with an autoregression estimation of interference spectrum and the Hurst exponent.

An autoregression equation governs the relationship between the current and previous samples of a sampled stochastic process. Earlier in the 1980-ies the problem of autoregression on the basis of canonical system of Yule-Walker equations with transformation of luminance histogram was solved by the investigators.

Thus, the detector in Fig. 8 uses real fractal properties of the power spectrum based on the autoregressive spectral estimation, used for the detection of low-contrast targets. Note that schemes like in Fig. 7 and Fig. 8 are often studied in China at present [2]. Similar detectors were used by the author in the texture processing of APS and radar images as early as in the 80-ies of the XX century. The author emphasizes that the correlation dimension (Fig. 5) that requires a large sample collection size, which is unrealistic in radiolocation and cannot be considered as detection statistics.

6. A NEW DIRECTION IN THE THEORY OF STATISTICAL SOLUTIONS AND IN STATISTICAL RADIO ENGINEERING

Fast development of the fractal theory in radar and radio physics led to establishing of the new theoretical direction in modern radar. It can be described as "Statistical theory of fractal radar".

This direction includes (at least at the initial stage) the following fundamental questions:

- 1). - The theory of the integer and fractional measure.
- 2). - Caratheodory construction in the measure theory.

- 3). - Hausdorff measure and Hausdorff-Besicovitch dimension.
- 4). - The theory of topological spaces.
- 5). - The dimension theory.
- 6). - The line from the point of view of mathematician.
- 7). - Non-differentiable functions and sets.
- 8). - Fundamentals of the theory of probability.
- 9). - Stable probability distributions.
- 10). - The theory of fractional calculus.
- 11). - The classical Brownian motion.
- 12). - Generalized Brownian motion.
- 13). - Fractal sets.
- 14). - Anomalous diffusion.
- 15). - The main criteria for statistical decision theory in radar.
- 16). - Wave propagation in fractal random media.
- 17). - Wave scattering generalized Brownian surface.
- 18). - Wave scattering surface on the basis of non-differentiable functions.
- 19). - Diffractals.
- 20). - Cluster analysis.
- 21). - Theory and circuitry of fractal detectors.
- 22). - Fractal-scaling or scale-invariant radar.
- 23). - The multi-radar.
- 24). - MIMO radar.
- 25). - Cognitive radar.

This list of studied questions, of course, is supposed to be expanded and refined in the future. The author has been dealing with it for nearly 40 years of his scientific career.

7. CONCLUSION

The author created, developed and applied fractal-scaling methods for radiolocation problems and forming the foundations of fractal element base [1 - 12, 17- 28]. For the first time ever approaches to development of a fractal radar and a fractal MIMO-radar were considered. The author emphasizes that the synthesis of topological (fractal, textural, chaotic, etc.) detectors makes for a fresh look at the problem of detecting super weak actual signals. As a result of that, the author's discovery in the away-back 1980-ies takes the meaning of generalized detection.

Thus, pure energy and pure topological detectors are not contrary to each other and they do not duplicate, but complement one another.

Due to topological detectors it is possible to see the process of energy detection in a new light and to find some essential faults in it. Consequently, topological detection becomes not less, if not more, valuable for theory and practice than energy detection. The theory of topological detection is formulated in [1-12, 17-28]. It is especially necessary for the purpose of reexamining the former theory and in that way producing new results that are not available to traditional concepts of radiolocation.

Thus, topological detection opens the door to a radically new field of statistical decision theory and provides an opportunity to correct ideas in this field, and even to create new ones, which is of great theoretical and practical importance. The sufficiently detailed reasoning reported here should contribute to a better understanding of proposed by the author fundamentally new interpretation of the problem of radar (and other kinds of) detection. The proposed theory has much in common with cognitive radar.

Thus, during more than 35 years, almost from scratch, fundamental bases of the theory that will be applied in the following decades were formed. Not results, not specific solutions are the most valuable, but namely the solution method, the approach to it. The created method is presented in [1-12, 17-34].

The author raised the foregoing problems as early as in 1980 and for more than 35 years he has been successfully working on their solution and development. Careful bibliographic studies show complete and absolute world priority of the author in all "fractal" fields of radiolocation and radiophysics (the list of the author's works in cooperation with students has about 900 publications, including 32 monographs).

ACKNOWLEDGMENTS

This work was supported in part by the project of International Science and Technology Center No. 0847.2 (2000-2005, USA), Russian Foundation

for Basic Research (projects №№ 05-07-90349, 07-07-07005, 07-07-12054, 07-08-00637, 11-07-00203), and also was supported in part by the project "Leading Talents of Guangdong Province", № 00201502 (2016-2020) in the JiNan University (China, Guangzhou).

REFERENCES

- Potapov AA. Chaos Theory, Fractals and Scaling in the Radar: A Look from 2015. In: *The Foundations of Chaos Revisited: From Poincaré to Recent Advancements*, ed. C. Skiadas. Springer, Switzerland, Basel, 2016, pp. 195-218.
- Potapov AA, Wu Hao, Foukzon J, Podosenov SA, Men'kova ER. *Fields, Fractals, Control and Low – Contrast Target Detection*. China, 2017, in print.
- Potapov AA. The Fractal-Scaling Radiolocation: Formation History 1980-2015. *Chaotic Modeling and Simulation (CMSIM)*, 2016, 3:317-331.
- Potapov AA. The Textures, Fractal, Scaling Effects and Fractional Operators as a Basis of New Methods of Information Processing and Fractal Radio Systems Designing. *Proc. SPIE*, 2009, 7374:73740E-1-73740E-14.
- Potapov AA. New Conception of Fractal Radio Device with Fractal Antennas and Fractal Detectors in the MIMO Systems. *Abstracts of the 9th Int. Conf. on Chaotic Modeling, Simulation and Applications (CHAOS'2016)*, University of London, London, U.K., 2016, pp. 85.
- Potapov AA, German VA. Detection of Artificial Objects with Fractal Signatures. *Pattern Recognition and Image Analysis*, 1998, 8(2):226-229.
- Potapov AA, German VA. Fractals, Fractal Target Selection and Fractal Antennas. *Proc. of the 1st Int. Workshop on Mathematical Modeling of Physical Processes in Inhomogeneous Media*, Mexico, Guanajuato, 2001, pp. 44-46.
- Potapov AA. New Information Radiophysical Technologies Fractal in Radiolocation: Fractal and Synergetic. *Proc. of 28th ESA Antenna Workshop on pace Antenna Systems and Technologies* (Noordwijk, The Netherlands, 31 May–03 June 2005), ESTEC, Noordwijk, 2005, pt. 2, pp. 1047-1050.
- Potapov AA. Can We Build an Adaptive Fractal Radio System? *Proc. of the PIERS 2009 in Moscow «Progress in Electromagnetics Research Symp.»*, Electromagnetics Academy, Cambridge, MA, 2009, pp. 1798–1802.
- Potapov AA. The Global Fractal Method, Fractal Paradigm and the Fractional Derivatives Method in Fundamental Radar Problems and Designing of Revolutionary Radio Signals Detectors. *Zbornik radova Konferencije MIT - Matematicke i informacione tehnologije* (Vrnjackoj Banji od 5. do 9. septembra i u Beticima od 10. do 14. septembra 2013. godine), Kosovska Mitrovica: Prirodno-matematički fakultet Ulverziteta u Pristini (Serbia), 2014, pp. 539-552.
- Potapov AA. Fractals, Scaling and Fractional Operators in Modern Physics and Radio Engineering. *Abstracts of the Int. Conf. XIV Khariton's Topical Scientific Reading "High-Power Pulsed Electrophysics"*, RFNC-VNIIEF, Sarov, 2014, pp. 81-82.
- Potapov AA. Fractal Radar: Towards 1980-2015. *Proc. of the Int. Conf. "CHAOS 2015"*, Henri Poincaré Institute, France, Paris, 2015, pp. 559-573.
- Haralick RM, Shanmugan K, Dinstein I. Textural Features for Image Classification. *IEEE Trans.*, 1973, SMC-3(6):610-621.
- Du G. Detection of sea-surface radar targets based on fractal model. *Electronics Letters*, 2004, 40(14):906-907.
- Soumeiya, Cherouat, Faouzi, Soltani, Françoise, Schmitt & Franck. Daout. Using fractal dimension to target detection in bistatic SAR data. *Signal, Image and Video Processing*, 2015, 9(2):365-371.
- Coopmans C, Malek H, Spencer E. Radiation and Impedance Characteristics of a Circular Loop Antenna Driven by Fractional Order Electronics. *Proc. of the Int. Design Engineering Technical Conf. ASME 2013 & Computers and Information in Engineering Conf. IDETC/CIE*, American Society of Mechanical Engineers, Portland, 2013, pp. V004T08A028-V004T08A028.
- Potapov AA. U istokov fraktalno-skeylingovoy ili masshtabno-invariantnoy radiolokatsii (1980-2015) [At the origins on fractal scaling or scale-invariant radiolocation (1980-2015)]. *Radiotekhnika*, 2015, 8:95-106 [in Russian].
- Potapov AA. Fractal-scaling or scale-invariant radiolocation principles and their application in synthetic aperture radars. *Coll. of scientific papers of*

- III All-Russian STC "Prospects of development of early warning RS, integrated systems and information support complexes of ASD and information management and processing systems: "RTI Systems of ASD-2015", N.E. Bauman MSTU Publishing House, Moscow, 2015, pp. 573-590 [in Russian].
19. Potapov AA. Synthesis of new kinds of dynamic textural-fractal detectors of low-contrast targets with contour extraction and the coordinate location against the background of high-intense ground, sea and rainfall clutters. *Proc. of the 26th Intern. Crimean Conf. "Microwave engineering and telecommunication technologies", KryMiKo'2016*, Sevastopol, 2016, 12:2625-2636 [in Russian].
 20. Potapov AA. On the strategic directions in the synthesis of new kinds of textural fractal radar detectors of low-contrast targets with contour extraction and the coordinate location against the background of high-intense ground, sea and rainfall clutters. *Proc. of the IV All-Russian STC "Prospects of development of early warning radar systems, integrated systems and information support complexes of aerospace defense and information management and processing systems "RTI Systems of ASD-2016 "*, OJSC "Academician A.L. Mintz RTI", Moscow, 2016, pp.12 [in Russian].
 21. Potapov AA. Strategic Directions in the synthesis of new topological radar detectors of low contrast targets against the background of intense ground, sea and rainfall clutters. *Nelineyny mir*, 2016, 14(3):6-22 [in Russian].
 22. Potapov AA. Processing of blurred images obtained by UAVs flying over nonuniform terrain using fractal-scaling and integrated methods. *Radiotekhnika*, 2016, 7:119-124 [in Russian].
 23. Potapov AA. *Fraktaly v radiofizike i radiolokatsii: topologiya vyborke* [Fractals in Radio Physics and Radar: Topology of Sample], 2-th issue ed. and correct, University Library, Moscow, 2005.
 24. Potapov AA, German VA. A Local-Dispersion Method of Measuring a Fractal Dimension and Fractal Signatures. *Proc. 2016 CIE Int. Conf. on Radar «Radar 2016»*, ed. Wu Shunjun (China, Guangzhou, Oct. 10-12, 2016), Chinese Institute of Electronics (CIE), Beijing, 2016, pp. 799-803.
 25. Potapov AA, German VA, Pahomov AA. Processing of Images Obtained from Unmanned Aerial Vehicles in the Regime of Flight over Inhomogeneous Terrain with Fractal-Scaling and Integral Method. *Proc. 2016 CIE Int. Conf. on Radar «Radar 2016»*, ed. Wu Shunjun (China, Guangzhou, Oct. 10-12, 2016), Chinese Institute of Electronics (CIE), Beijing, 2016, pp. 585-587.
 26. Potapov AA. Strategic Directions in Synthesis of New Topological Radar Detectors of Low-Contrast Targets against the Background of High-Intensity Noise from the Ground, Sea and Precipitations. *Proc. 2016 CIE Int. Conf. on Radar «Radar 2016»*, ed. Wu Shunjun (China, Guangzhou, Oct. 10-12, 2016), Chinese Institute of Electronics (CIE), Beijing, 2016, pp. 692-696.
 27. Potapov AA, Rassadin AE. The latest achievements in the development of the concept of radio- and optical systems quasiparticle based on Feynman integrals. *Proc. SPIE*, 2017, 10342, in print (doi: 10.1117/12.2270592).
 28. Potapov AA. Fractal Scaling or Scale-invariant Radar: A Breakthrough into the Future. *Universal Journal of Physics and Application (USA)*, 2017, 11(1):13-32.
 29. Potapov Alexander, Potapov Victor. Fractal Radioelement's, Devices and Systems for Radar and Future Telecommunications: Antennas, Capacitor, Memristor, Smart 2D Frequency-Selective Surfaces, Labyrinths and Other Fractal Metamaterials. *Materials, Methods & Technologies*, 2017, 11:492-512.
 30. Potapov AA. Diffractals at frequency 36 GHz which are observed at radar scattering of an electromagnetic wave by a fractal surface and wave catastrophes in fractal randomly inhomogeneous media. *Proc. XIII Int. Conf. "Zababakhin Scientific Talks" Dedicated to 100th anniversary of academician E.I. Zababakhin* (Snezhinsk, March 20-24, 2017). Snezhinsk, RFNC-VNIITF, 2017, pp. 137-138.
 31. Potapov Alexander A. Diffractals at Millimeter Waves and Waves Catastrophes in Fractal Randomly Inhomogeneous Media: Theory and Experiments. *Book of Abstracts of the 10th Chaotic Modeling and Simulation International Conference (Barcelona, Spain: 30 May-2 June, 2017)*, ed. Christos H Skiadas. Barcelona, International Society for the Advancement of Science and Technology Publ., 2017, pp. 100-101.
 32. Potapov Alexander A. Postulates of Fractal Radar. *Book of Abstracts of the 10th Chaotic Modeling and Simulation International Conference (Barcelona, Spain: 30 May-2 June, 2017)*, ed. Christos H

- Skiadas. Barcelona, International Society for the Advancement of Science and Technology Publ., 2017, p. 101.
33. Potapov Alexander. On the Indicatrixes of Waves Scattering from the Random Fractal Anisotropic Surface. In: *Fractal Analysis – Applications in Physics, Engineering and Technology*. Ed. Fernando Brambila. Rijeka: InTech. P. 187-248 (eBook ISBN 978-953-51-3192-2, Print ISBN 978-953-51-3191-5), 2017.
34. Potapov Alexander. Postulate "The Topology Maximum at the Energy Minimum" for Textural and Fractal-and-Scaling Processing of Multidimensional Super Weak Signals against a Background of Noises. In: *Nonlinearity: Problems, Solutions and Applications*, 2017, vol. 2, pp. 35-94. Ed. Ludmila A. Uvarova, Alexey B. Nadykto, Anatoly V. Latyshev. New York: Nova Science Publ. (eBook ISBN: 978-1-53612-184-1, Print ISBN 978-1-53612-163-6).

CREATION AND TESTING OF A FOUR-CHANNEL INSTALLATION FOR TESTING AT A MODERN EXPERIMENTAL LEVEL OF DISCUSSION KOZYREV ASTRONOMICAL OBSERVATIONS

¹Stepan N. Andreev, ²Andrey V. Voropinov, ¹Dmitriy Yu. Tsipenyuk

¹Prokhorov General Physics Institute, Russian Academy of Sciences, <http://www.gpi.ru>
119991 Moscow, Russian Federation

²LaserGraphicArt Ltd., <http://www.lasergraphicart.com>
119991 Moscow, Russian Federation

nauka@gpi.ru, avv@lasergraphicart.com, tsip@kapella.gpi.ru

Abstract. The work is devoted to the design, the development of a measurement technique and testing of a four-channel experimental setup for verifying the results of N.A. Kozyrev's controversial astronomical observations. It was shown that the parameters of the installation make it possible to exceed the accuracy of measurements carried out earlier by N.A. Kozyrev, and get reliable data on the existence or absence of "Kozyrev radiation".

Keywords: "Kozyrev radiation", non-electromagnetic properties of optical radiation, thermal conductivity, relic radiation, Wheatstone bridge

PACS: 06.30.-k, 07.07.Df

Bibliography – 13 references

RENSIT, 2017, 9(2):139-146

Received 06.07.2017

DOI: 10.17725/rensit.2017.09.139

CONTENTS

1. INTRODUCTION (139)
 2. DESCRIPTION OF THE DESIGN AND MEASUREMENT TECHNIQUES IN THE ORIGINAL AND SUBSEQUENT EXPERIMENTS TO OBSERVE "KOZYREV RADIATION" (141)
 3. DESCRIPTION OF INSTALLATION DESIGN AND MEASUREMENT TECHNIQUES (142)
 4. TESTING INSTALLATION PARAMETERS (143)
 5. CONCLUSIONS (145)
- REFEREBCES (145)

1. INTRODUCTION

In 1976, at the symposium in Byurakan (Armenia), Nikolay A. Kozyrev reported on the opening a new type of penetrating radiation, which he detected when scanning a celestial sphere with a telescope-reflector, closed with an impenetrable cover – the so-called "Kozyrev's radiation." The "Kozyrev radiation" sensor was a thin-film resistor located in the focal plane of the telescope and included in the shoulder of a balanced Wheatstone bridge connected to a galvanometer [1, 2]. N.A. Kozyrev found

that when the telescope was pointing at certain astronomical objects (stars, star clusters, galaxies) or on their surroundings, the resistance of the resistor changed and the Wheatstone bridge became unbalanced. He was investigated more than 30 astronomical objects, which were causing the appearance of signals on the galvanometer. At the time of recording signals, the orientation of the telescope sometimes strictly coincide, but more often did not coincide with the direction on the astronomical objects visible in the telescope. The results Kozyrev's astronomical observations caused an ambiguous and rather skeptical reaction of the scientific community, although as time went on, publications appeared that confirmed experimentally the stated effect [3-5, 9-11].

N.A. Kozyrev believed that the results of his astronomical observations confirm the "causal or asymmetric mechanics" he created in 1958. The theoretical model proposed by N.A. Kozyrev, did not receive the recognition of the scientific community. In 1960, under

the Bureau of the Department of Physical and Mathematical Sciences of the USSR Academy of Sciences, a commission was set up under the chairmanship of Corresponding Member USSR Academy of Sciences AA Mikhailov on the verification of "causal mechanics" NA Kozyrev. It consisted of nine people, divided into subgroups, engaged in verification in three areas: theory, experiment, the problem of asymmetry of the planets. In the studies that lasted about six months, NA Kozyrev himself participated, as well as a number of other specialists. The results were announced on June 15, 1960. The general conclusions were as follows [12]:

- a) the theory is not based on a clearly formulated axiomatics, its conclusions are not developed quite strictly by a logical or mathematical method;
- b) the quality and accuracy of the laboratory experiments do not make it possible to draw definite conclusions about the nature of the observed effects; in the experiments, various side effects have not been sufficiently eliminated.

In the opinion of Academician A.M. Cherepashchuk, director of the State Astronomical Institute named after PK Shternberg, at the present time NA Kozyrev's theory is rejected by the overwhelming majority of physicists and astronomers in view of the complete unreasonableness [13]. Thus, the verification of the results of his experiments, carried out at his own request by two commissions of the Academic Council of the Pulkovo Observatory in 1960 and 1967, showed that the effects observed by him are at the limit of measurement accuracy and are not convincing. Nevertheless, the question of the existence of a "Kozyrev radiation" is still open, as and the problem of creating a theory explaining this effect.

The original explanation of the observed effect was suggested by AG. Parkhomov in his work in [5]. He put forward the hypothesis

that the effects found in NA Kozyrev's experiments are related to gravitational focusing by astronomical objects of some cosmic radiation or a stream of particles. It allows us to explain the phenomenon "Kozyrev radiation" without the assumption of instantaneous or superluminal information transfer speed in space.

We note that the assumption of the existence of particles moving at a speed of several hundred kilometers per second and relatively weakly interacting with thin layers of metal and dielectrics (the telescope cover) [5] correlates well with the conclusions of the five-dimensional theoretical model of the expanded space (ESM) that developing since 1999 by D.Yu. Tsipenyuk and V.A. Andreev [6-8]. In accordance with this model in the five-dimensional space $(1 + 4)D$, in which the interval S is considered as the fifth coordinate (the physical meaning of the fifth coordinate is the action), massless photons can acquire mass in an external field and become carriers of new fields - one vector and one scalar in addition to the electromagnetic field. According to the ESM, photons can acquire non-electromagnetic properties reversibly upon entering in external field [7].

As for the possibility of organizing an experiment to test the Kozyrev effect, it is described in sufficient detail, for example, in [2, 3, 5] and can be repeated at the modern level with the aid of a telescope-reflector.

Having carried out a series of verification experiments on registration the unusual Kozyrev effect, it is possible, in case of confirmation of this phenomenon, to obtain a new object for a large-scale space exploration, comparable in importance to the relic radiation. In this case, the agenda will be the question of mapping the distribution of a new type of cosmic radiation in the entire space sphere with the help of ground-based instruments and, subsequently, space observatories.

2. DESCRIPTION OF THE DESIGN AND TECHNIQUE OF MEASUREMENTS IN ORIGINAL AND FOLLOWING EXPERIMENTS ON OBSERVATION OF "KOZYREV RADIATION"

In the original experiments conducted by NA. Kozyrev [1], a 50-dm telescope-reflector of the Crimean Astrophysical Observatory was used for observation. In subsequent works conducted under the guidance of Academician Lavrent'ev [9], a telescope with a significantly smaller diameter was used: "For the observation ... the telescope" MITTAR "TAL-1 (the diameter of the main mirror 110 mm) was sufficient." A.G. Parkhomov in his experiments used a telescope with a mirror diameter of about 22 cm [4, 5].

Kozyrev requirements to the simplest and most reliable sensor are formulated by him as follows: "The sensor itself should register only differential changes in its working element as compared to elements protected from the process being studied. Under this condition, the effect of the background, that is, the action of the set of surrounding processes, is largely excluded. In this sense, a sensor that is based on a change in the electrical conductivity of a resistor inserted into the Wheatstone bridge is particularly convenient and sensitive enough. The Wheatstone bridge was built on the basis of metal-film resistors of the OMLT-0.125 type with resistances of 5.6 k Ω having a positive temperature coefficient of 0.0015 (1/K). The value of the resistance of the resistors was chosen close to the internal resistance of the galvanometer (device type M-95, accuracy class 1.5), equal to 5 k Ω . The value of the galvanometer division was $2 \cdot 10^{-9}$ A. A stabilized voltage of 30 V was supplied from the constant-current source to the Wheatstone bridge. To balance the bridge's shoulders at the input, a resistors store was connected from the power source side. Due to this, it was possible to estimate the galvanometer dial in the values

of the resistance changes: to one division of the galvanometer corresponded a change of $1.1 \cdot 10^{-2}$ Ohm, which is $2.7 \cdot 10^{-6}$ relative change" [1].

Kozyrev observations were carried out in the focus Nesmit-Cassegrain of reflector, where the spectrograph slit with sight device was located. "... The scale on the gap was 8" in mm. From the spectrograph has been left only a bronze casing, closed on butt end by thick cardboard. The bridge resistors were mounted on a cardboard base fixed in a closed aluminum cylinder inserted inside the casing behind the slot device. The measurement procedure consisted in directing the telescope to the star under study, after which a multiple scanning of the sky around the star was carried out. After visual guidance on a star, the inlet was closed by light-tight aluminum cover thickness of about 1.5 mm. The magnitude of the measured effect was registered by the operator visually by the deflection of the galvanometer arrow with simultaneous registration of the coordinates of the section of the sky on which the telescope is aimed" [1].

A similar scheme and measurement technique was used by the authors, who later verified Kozyrev's experiments [3-5, 9-12]. We should especially note a large series of papers published in the journal DAN by a group led by Academician M.M. Lavrent'ev [3, 9, 10, 11].

In addition to the Wheatstone bridge, the authors of [3-5, 9-12] investigated the possibility of using for registration of "Kozyrev radiation" and other sensors based on a wide variety of physical and even biological processes for recording. However, this part of the researches, in our opinion, can be considered only after the "Kozyrev radiation" will be authentically and reliably fixed using the simplest, and therefore the most reliably studied and easily controlled sensor applied by NA. Kozyrev – by Wheatstone bridge.

3. DESCRIPTION OF INSTALLATION DESIGN AND MEASUREMENT TECHNIQUES

To carry out experiments on the detection of "Kozyrev radiation," we designed and manufactured a set of equipment containing two identical sensor heads fixed on a telescope (Fig. 1), as well as a board with the necessary measuring instruments connected by cables with earthed screens. The only difference between the sensor heads is that the measuring head is installed in the focus of the telescope's output eyepiece, and the control head can be fixed at a distance of 10 to 50 cm from the measuring head.

Analysis of the description of Kozyrev and his followers experiments makes it possible to assume that the imbalance of the Wheatstone bridge when the telescope was aimed at the

astronomical object occurred due to a decrease in the thermal conductivity coefficient, both the material of the sensor resistor itself and of the ambient air. As a result, the temperature of the resistor increased, which was recorded during the measurements. To test this hypothesis, we added a temperature sensor, based on a platinum resistance thermometer, to each sensor head in addition to the Wheatstone bridge resistor.

This four-channel experiment schema allows us to monitor the noises of various nature present in the area of the installation and to select only those signals that are associated with the expected impact of "Kozyrev radiation" to the sensors.

The body of the sensor head (Fig. 2) was made of sheet polymethylmethacrylate. Inside, a Wheatstone bridge sensor resistor and a resistance thermometer were placed. The remaining resistors of the Wheatstone bridge were placed inside their own casing, spaced from the sensor head by a distance of about 40 cm.

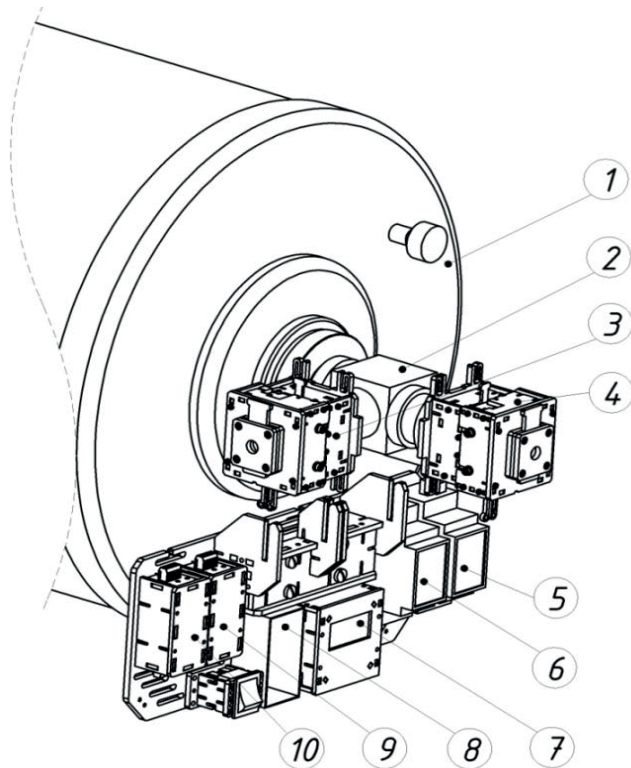


Fig. 1. Appearance of the device mounted on the Meade telescope: 1 – telescope; 2 – node of the elevating diagonal mirror; 3 – control sensor head; 4 – working sensor head; 5 – working channel voltmeter; 6 – the voltmeter of the control channel; 7 – two-channel temperature control device; 8 – power element; 9 – working bridge casing; 10 – the casing of the control bridge.

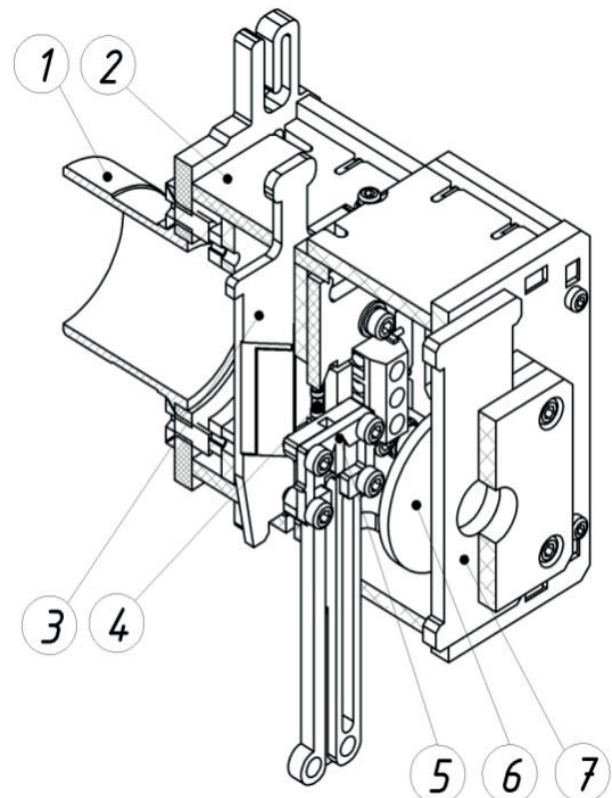


Fig. 2. Sensor head device (cut): 1 – landing bush 1.25", 2 – sensor head corpus, 3 – replaceable slit, 4 – sensor resistor, 5 – platinum thermometer mounting, 6 – eyepiece, 7 – eyepiece blind.

The unbalance of the bridge was registered using the digital millivoltmeter AME-1102 manufactured by Aktakom, which was connected to the laptop via a USB interface. The resistance thermometer Pt1000 was connected to the two-channel temperature controller DX5100 manufactured by RMT company, connected to the laptop via the RS-485 interface. The temperature controller DX5100 is an industrial sample used, for example, to maintain the temperature in a nonlinear crystal with an accuracy of at least 0.01°C. The DX5100 system with a Pt1000 resistance thermometer is calibrated during manufacture and has a built-in mechanism of calibration, that allows measuring the temperature with an accuracy of 0.005°C. The values of the unbalance voltage of the Wheatstone bridge and the temperature value obtained from the operating and control sensor heads, were recorded synchronously into one data array using specially designed software.

From the point of view of the maximum use of the measurement range of the digital millivoltmeter AME-1102, the most convenient resistance nominals for resistors used in the bridges of our installation are about 1 kΩ. Wheatstone bridges were made of metal oxide film resistors of type C2.23 with a rated power of 0.25 W with a temperature coefficient of resistance of $0.1 \cdot 10^{-3}$ (1/K). The spread of resistance values of resistors from 985 to 1007 Ohm made it possible to obtain voltage on the measuring diagonal of the Wheatstone bridge from 20 to 180 mV when applying voltage from 8 to 20V on the diagonal of supply from the DC power supply unit B5-30.

Following the description of the experiment given by NA Kozyrev [1], the sensor resistor was fixed so that its cylindrical surface touched the meridian plane of the telescope's optical system. The slit in front of the resistor was made up of two steel plates 0.5 mm thick and was replaceable from 0.3 to 2.0 mm. The coincidence of the focal plane of the main mirror of the telescope with the plane of the resistor was controlled

visually by means of the eyepiece built into the body of the head. To screen the resistor from the focused parasitic light during the measurement, the eyepiece was closed by a movable blind. The platinum resistance thermometer Pt1000 was mounted on a copper foil plate with an area of 1 cm² and was shifted from the optical axis by 1 cm. The placement of the control head on the second exit of nodule of the telescope lifting mirror assembly made it possible to equalize the air temperature in the volumes of the sensor heads.

The general scheme of the experimental setup is shown in Fig. 3.

4. TESTING OF INSTALLATION PARAMETERS

Within the experimental study of the response time, sensitivity and intrinsic noises of the installation, we conducted more than 30 measurement series, as in laboratory conditions, so and in the case of installation of equipment on two telescopes-reflectors Meade LX-200-ACF with the diameters of the main mirror 14"

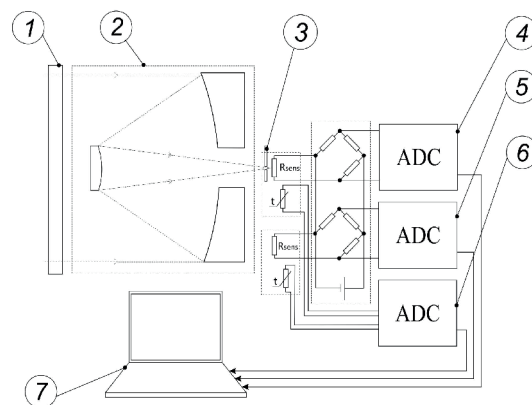


Fig. 3. Basic diagram of the experiment: 1 – opaque screen; 2 – telescope; 3 – slit; 4 – measuring channel; 5 – control channel; 6 – temperature channel; 7 – computer. Scheme of measuring four-channel installation consisting of identical measuring and control channels mounted in two identical sensor heads. Each channel consists of two sensors - a Wheatstone bridge based on metal oxide film resistors such as C2.23 and resistance thermometers based on the Pt1000 platinum resistor. The digital millivoltmeters AME-1102 measured the mismatch voltage by R_{sensor} ; Two-channel temperature controller DX5100 measured data from Pt1000.

and 16". The total data accumulation time in the various series of measurements was usually from 40 to 480 minutes. The operating frequency of the measuring channels was about 3 Hz.

Experiments to measure the response time of the installation to an external action (blowing the head with a hot or cold gas flow for 1 s) showed that the reaction time is of the order of 0.2-0.3 s in all four channels. The relaxation time after the impact on the sensors based on the Wheatstone bridge was 25-30 seconds. For sensors based on the Pt1000 platinum resistance thermometer, the relaxation time is much longer – about 230-250 s. The difference in the relaxation time of the sensors based on the Wheatstone bridge and the Pt1000 resistance thermometer is caused, apparently, by the difference in thermal energy, which is scattered by the sensors per unit time.

An experimental determination of the sensitivity of sensors based on Wheatstone bridges was carried out with a slow heating of a closed volume into which both measuring heads were placed. The obtained graphs of depending of the bridge imbalance voltage and the current temperature inside the head from time allowed

estimating the accuracy of the temperature measurement with the help of Wheatstone bridges in 0.01 C, while the error of measuring the imbalance voltage of the Wheatstone bridges was less than 1 mV.

As an example of test measurements of astronomical objects in **Fig. 4** the data received on February 9, 2016 when the Wheatstone bridge was installed on a telescope-reflector Meade LX-200-ACF with a mirror diameter of 14" are given.

The measurement frequency was about 1 Hz, each counting is the arithmetic mean of 100 measurements of the misalignment signal. Fig. 4 shows both the data of the Wheatstone bridge misalignment signal (left scale) and the measured rms deviation of each counting for 100 measurements (right scale). The amplitude of the change in the misalignment signal during the test tests was from 0.023 to 0.025 V, and the measured rms deviation of each measurement was about 0.001 V.

The telescope is located in the Moscow region in a rotating automated dome with heating and

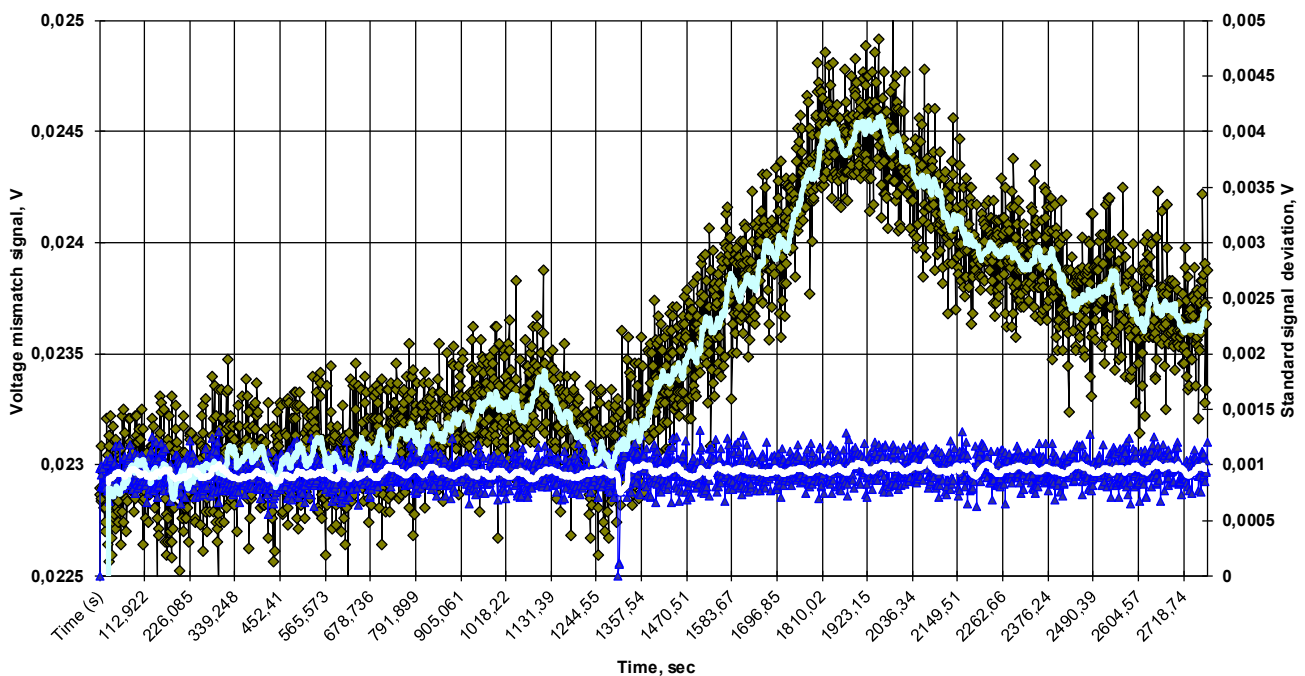


Fig. 4. Test measurements on a telescope reflector Meade LX-200-ACF 14". 02/09/2016 - Set of backgrounds up to 1300 sec. -The telescope is closed by cover and directed along the horizon. From 1300 to 2700 seconds the measurement of the Wheatstone bridge mismatch signal. Telescope cover removed and telescope directed per star.

power supply built especially for astronomical observations.

The time of the experiments from 11.00 to 12.00 Moscow time. The weather conditions at the site of the experiments on 09.11.2016 were as follows: air temperature -3°C , wind 2 m/s, cloudy, humidity 81%, pressure 748 mm Hg.

After installing the equipment on the telescope at 11.15 the installation was switched on and warmed up. The measurements were started in 11.32. The total time of the test measurements was 2700 s.

At first the telescope for 1300 s was oriented along the horizon line and directed to the dome wall, with a standard aluminum cover 1.5 mm thick on the telescope. From 1300 to 2700 s the telescope was aimed at the star Alpha Ursa Major Dubhe (Dubhe α UMa) with the dome open and the lid removed. For observation, a region was chosen in the vicinity of this star, since it was indicated in the works of NA Kozyrev, as one of the objects of observation, in the study of which a positive result was obtained.

By directing the telescope to the star region, we performed various manipulations with the focusing of telescope on the star, and also scanned 2 minutes of the region 5 degrees "to" the star and 5 degrees "after" the star.

As can be seen from Fig. 4, a statistically significant increase in the misalignment of the Wheatstone bridge signal was recorded when the telescope was pointed at the Dubhe star from 1300 to 2700 seconds, compared to the control set of background from 0 to 1300 seconds of measurement.

5. CONCLUSIONS

A compact four-channel installation has been created and tested in laboratory and field conditions, allowing at the present level to carry out research to verify the discussion NA Kozyrev experiments. The results of the test tests of the installation allow improving the accuracy of measurements and planning the experimental procedure for obtaining reliable

results. The design of the device allows us to verify the authors' assumption that the effect of "Kozyrev radiation" leads to a decrease in the thermal conductivity coefficient of the material, from which comprises the resistor, and of its surrounding air, as a result the temperature in the measuring channel of the Wheatstone bridge increases as compared to the control channel.

In the case of obtaining positive experimental results of registration of "Kozyrev radiation" on the agenda will be the task of continuous scanning the firmament for create a star map of "Kozyrev's radiation" similarly to how the discovery of relic radiation led to large-scale experiments on mapping the cosmic relic radiation of the universe.

After working out the experimental technique at the modern level and creating of basic experimental set including special software, it is possible to set the task of realizing the massive project "Creation by the joint forces of amateur astronomers and professional laboratories of Kozyrev's radiation star.

REFERENCES

1. Kozyrev NA, Nasonov VV. In: *Manifestation of cosmic factors on Earth and stars*. M.-L., 1980, p. 76-93.
2. Kozyrev NA. Selected Works, Izd. Len. University, Leningrad, 1991.
3. Lavrentyev MM, Eganova IL, Lutset MK, Fominykh SF. About distance action of stars on the resistor. *DAN*, 1990, 314(2).
4. Parkhomov AG. Observation of cosmic flows of slow weakly interacting particles. *Preprint No. 41 ISTC WENT*, M., 1993.
5. Parkhomov AG. Astronomical observations by Kozyrev's method and the problem of instantaneous signal transmission. *Physical Thought of Russia*, 2000, 1:18-25; http://www.chronos.msu.ru/RREPORTS/parkhomov_astronomicheskiye/parkhomov_astronomicheskiye.htm
6. Tsipenyuk DYu, Andreev VA. 5-Dimensional Extended Space Model. *Proc.*

- ESA-ESO-CERN Conference (EPS13)*, Bern, Switzerland, 11-15 July 2005 (ESA SP-605, November 2005), arXiv: physics/0601151.
7. Andreev VA, Tsipenyuk DYu. Mechanism of the Dark Matter and Condensed Bubble Objects Formation in the Model of Extended Space. *Bulletin of the Lebedev Physics Institute*, 2004, 9:13-25; arXiv: physics/0506002.
 8. Andreev VA, Tsipenyuk DYu. The Mass and Size of Photons in the 5-Dimensional Extended Space Model. *Journal of Modern Physics*, 2016, 7:1308-1315. <http://dx.doi.org/10.4236/jmp.2016.711116>.
 9. Lavrent'ev MM, Gusev VA, Eganova IA, et al. On registration of the true position of the Sun. *Dokl. AN SSSR*, 1990, 315(2).
 10. Lavrent'ev, MM, Eganova IA, Lutset MK et al. On Recording the Reaction of a Substance to an External Irreversible Process. *Dokl. AN SSSR*, 1991, 317(3).
 11. Lavrent'ev MM, Eganova IA, Medvedev VG et al. On the scanning of the stellar sky by the Kozyrev probe. *Dokl. AN*, 1992, 323(4).
 12. Materials of the commission for the study and verification of NA Kozyrev's works. *Archives of the Main Astronomical Observatory of the USSR Academy of Sciences in Pulkovo (GAO)*, 1960; https://ru.wikipedia.org/wiki/causal_mechanics.
 13. Kruglyakov E. Common sense, 1998/99, №10; <http://www.atheism.ru/old/KruAth1.html>.

ATOM IN A STRONG MAGNETIC FIELD. TRANSFORMATION OF ATOMS INTO TRANSATOMS

Gennady V. Mishinsky

Joint Institute for Nuclear Research, <http://www.jinr.ru>

Dubna, Moscow Region 141980, Russian Federation

mysh@jinr.ru

Abstract. All ℓ -s and j-j bonds in a strong magnetic field B are broken in all atomic electrons and their orbital moments are "frozen-in" in the field. Electronic states with identical orbital ℓ and magnetic moments m_ℓ are split into two levels with antiparallel electron spins $s = \pm 1/2$. The frequency of transitions between these levels $m_s = \pm 1/2$ is the same for all electron pairs $\omega = 2\mu_e B/\hbar$. Electromagnetic interaction of electrons causes them to oscillate near their orbitals. These oscillations are quantized by introducing a new quantum number. The exchange interaction between two electrons, an additional asymmetry in their oscillations enable the electrons to create an ortho-boson with $S = 1$. The orbital magnetic moment m_ℓ of each electron precesses around the magnetic field B with a frequency $\omega = \ell \cdot \mu_e B/\hbar$ and creates its own internal magnetic field B_μ rotating with the same frequency. The internal magnetic field B_μ stimulates transitions between the levels $m_s = 1/2 \rightarrow m_s = -1/2$. Thus, ortho-bosons are formed in the entire atom and electron Bose–Einstein condensate is produced. Consequently, atoms, in a strong magnetic field, inevitably turn into transatoms.

Keywords: atomic physics, quantum physics, electron Bose–Einstein condensate, the Pauli principle, electron magnetic resonance, coherent radiation, condensed matter nuclear science

PACS: 36.10.-k; 32.10.-f; 76.30.-v; 03.75.Mn; 03.75.Nt; 42.55.Vc

Bibliography – 27 references

Received 14.11.2017

RENSIT, 2017, 9(2):147-160

DOI: 10.17725/rensit.2017.09.147

CONTENTS

1. INTRODUCTION (147)
 2. ATOM IN WEAK, MEDIUM AND ULTRA STRONG MAGNETIC FIELDS (148)
 3. ATOM IN STRONG MAGNETIC FIELDS. ELECTRON OSCILLATIONS (149)
 4. ELECTRON PAIRING INTO ORTHO-BOSON (152)
 5. INTRA-ATOMIC ELECTRON MAGNETIC RESONANCE (154)
 6. ATOM AS $Z/2$ ACTIVE MEDIUM (156)
 7. FORMATION OF TRANSATOMS AND TRANSMOLECULES (157)
 8. CONCLUSION (158)
- REFERENCES (159)

1. INTRODUCTION

"The electron is as inexhaustible as the atom, nature is infinite, but it exists infinitely..." [1]. This statement is associated with the development, in the early 20th century, of the theory of

knowledge. The author of this statement did not, at the time of writing that article, yet know that electrons are part of atoms, and he considered them to be independent substances. For physicists, this phrase should sound the opposite: the atom is inexhaustible like the electron. Such a turn is caused, in the theory of systems, by the dependence of properties of the system on the state of its constituent elements, and on the changing behavior of their existence in changing external conditions. In our case, the atom is a system, and the electrons, along with atomic nucleus, are its constituent elements. Changes in properties and behavior, both of electrons and nuclei, cause appropriate transformations in the properties of the atom. In this paper, we consider a change in atomic structure when an atom is placed in a strong magnetic field. In science and technology, magnetic fields are subdivided into weak – up to 0.05 T, medium – 0.05÷4T; strong

– 4÷100T and ultrastrong fields – more than 100T. Furthermore, the presentation will adhere to that classification.

2. ATOM IN WEAK, MEDIUM AND ULTRA STRONG MAGNETIC FIELDS

The fine structure of optical spectra of atoms is explained by spin-orbit interaction, i.e. by the interaction of spin magnetic moments of all external electrons with magnetic field B_L produced by orbital motion of electrons in the atom. Calculations show that magnetic induction vector of the field created by orbital motion of electrons at the location of nucleus is 10÷200 T (for Li ~13 T, for Cs ~210 T). States with different orientations of the total electron spin S and the associated magnetic moment μ_s relative to B_L differ in energy by $\Delta E = -\mu_s B_L$, which causes a thin splitting of levels. The number of orientations $2S+1$ is determined by total spin of electrons S . The simplest picture of interaction is obtained for atoms with one external electron. In this case, there are only two orientations of the magnetic moment of the electron μ_e relative to B_L either along the field or against the field. Accordingly, two close lines are observed in the spectrum ($\mu_e = \hbar/2me = 9.29 \cdot 10^{-24} J/T = 5.79 \cdot 10^{-5} eV/T$, where \hbar is the Planck constant, e and m_e are electron charge and mass).

Atoms with several electrons in the outer shell have a more complicated fine structure. Thus helium with two electrons has single lines in case of antiparallel orientation of electron spins with total zero spin $S = 0$ – parahelium and triple lines in case of parallel orientation of electron spins with total spin $S = 1$ – orthohelium. The spin $S = 1$ corresponds to three possible projections on magnetic field direction: +1, 0, -1.

The hyperfine structure of spectral lines is explained by magnetic field interaction B_L with magnetic moment of the nucleus μ_I associated with its spin I . The extraordinary smallness of the hyperfine splitting is due to the smallness of nuclear magneton $\mu_N = \hbar/2mP = 3.15 \cdot 10^{-8} eV/T$,

where m_p is proton mass. When an atom is placed in an external magnetic field \mathbf{B} , the magnetic moments of electrons μ_s and the magnetic moment of the nucleus μ_I interact with both \mathbf{B} and the magnetic field produced by the orbital motion of electrons in the \mathbf{B}_L atom. The energy of such interaction is $\Delta E_e = -\mu_s(B_L + B)$, $\Delta E_I = -\mu_I(B_L + B)$.

Depending on influence on the structure of atomic levels, several cases of different values of \mathbf{B} are distinguished. A weak external field \mathbf{B} is a field that does not break the bonds between the nucleus (I) and the electrons ($F = J + I$) and between the orbital (L) and the spin (S) moments of the atom ($J = L+S$) (Zeeman effect).

In the external field \mathbf{B} of a medium value, first, the I - J bond is broken and, secondly, the bond between the orbital and spin moments of the atom is broken: the L - S bond (the Paschen-Buck effect). Historically, in physical literature, such a field is called a "strong" field. The Paschen-Buck effect is manifested in magnetic fields up to 4 T, i.e. in medium fields, according to classification. Fig. 1 shows, as an example, the splitting in the weak (Fig. 1a) and medium magnetic fields of the 2S and 2P levels of the sodium atom. In case of the medium field (Fig. 1b), due to discontinuity of the L - S bond, one can no longer refer to the total atomic moment of the J atom. The $^2P_{1/2}$ and $^2P_{3/2}$ levels do not differ and are characterized as levels with $L = 1$. The orbital moment of an atom in this case can

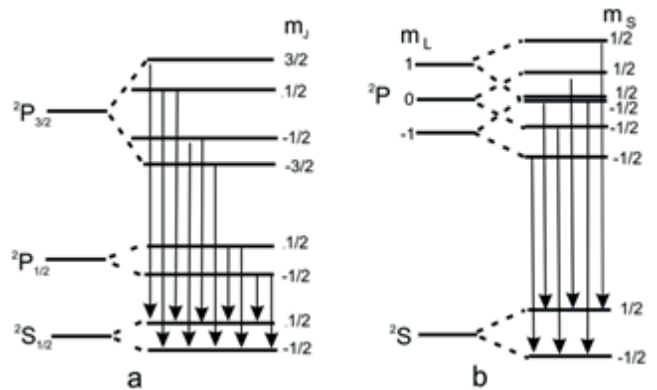


Fig. 1. Splitting of ground and excited energy levels of sodium atom: a – in a weak external magnetic field and b – in a medium magnetic field.

be oriented relative to field \mathbf{B} in three ways: $m_L = -1, 0, 1$. For each orientation of the orbital moment, the spin magnetic moment of an electron can be oriented in two ways, $m_S = \pm 1/2$, for both $L = 1$ and $L = 0$. Electron levels with higher energy correspond to magnetic moments directed against the vector of magnetic induction. The projections of magnetic moments on the direction of magnetic field do not change at that. The condition for breaking the L - S bond occurs when the interaction energy of magnetic moment of an atom with an external magnetic field becomes greater than the energy of the spin-orbit interaction. In this case, the spin magnetic moment of the nucleus, the spin and orbital magnetic moments of the atom begin to interact independently with external magnetic field, increasing or decreasing the energy of an atom, depending on the orientation of magnetic moments with respect to the direction of magnetic induction vector \mathbf{B} : $\Delta E = -\mu_L B - \mu_S B - 2\mu_e S \cdot B$, where $\mu_L = L \cdot \mu_B$, $\mu_B = \mu_e = \hbar/2m_e$. Each magnetic moment μ precesses independently the direction of magnetic induction vector of the external field with its frequency $\omega = \mu_B/\hbar$.

B.B. Kadomtsev showed in his papers [2-3] that in a heavy atom with a nuclear charge $Z \gg 1$ located in a ultrastrong magnetic field \mathbf{B} , with which the magnetic interaction of atomic electrons becomes larger than their Coulomb interaction and whose value exceeds significantly $10^6 T$ ($B \gg 10^5 \cdot Z^{4/3} T$), a complete rearrangement of electron configurations of all atomic electrons occurs. In this case, the electrons move in thin cylindrical shells, oscillating parallel to the axis of the magnetic field, and simultaneously rotate around the nucleus. At $B \ll 10^5 \cdot Z^3 T$, several electrons are located on each shell. In this case, the atom retains spherical symmetry, and its radius changes as $(Z/B^2)^{1/5}$, i.e. the atom contracts with increasing \mathbf{B} . For $B \gg 10^5 \cdot Z^4 T$, each individual electron precesses around the nucleus and makes motion in a thin cylindrical shell with a radius R , oscillating along the magnetic field axis. The

wave functions of individual electrons do not overlap, i.e. the exchange interaction is absent.

Thus, the structure of atomic levels varies both in the medium and ultrastrong magnetic fields. The question arises: How will change the structure of an atom in a strong magnetic field exceeding $20 T$?

3. ATOM IN STRONG MAGNETIC FIELD. ELECTRON OSCILLATIONS

It has been known that the state of an electron in an atom can be characterized by four quantum numbers: ground quantum number $n = 1, 2, 3, \dots$; orbital quantum number $\ell = 0, 1, 2, \dots, n-1$; magnetic quantum number $m_\ell = -\ell, -\ell+1, \dots, 0, \dots, \ell+1, \ell$; spin magnetic moment of an electron $m_s = +1/2$ or $m_s = -1/2$. According to Pauli principle, an atom cannot contain electrons with the same set of quantum numbers. Electrons with the same ground quantum number n form the shell of an atom. Fig. 2a shows the filling of shells by electrons in a sodium atom.

For clearness, the Bohr concept of elliptic motion of electrons in a plane will be used in reasoning and drawings.

The internal electron orbitals of the atom, in the absence of a strong magnetic field, do not have a constant orientation in outer space, since they precess under the action of other charges

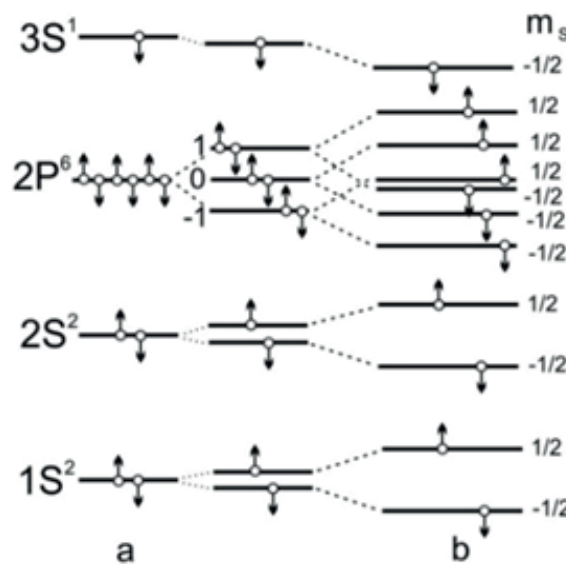


Fig. 2. a – filling with electrons of sodium atom shell; b – splitting of sodium atom energy levels in a strong magnetic field.

and cease to lie in one plane. The electron moves around the nucleus not in a plane, but along a trajectory similar to "thread in the clew" [4]. Therefore, in spite of the fact that the orbital moments for p , d ... of electronic states differ from zero ($\ell \neq 0$), the medium values of orbital moments for x -, y - and z -components are equal to zero: $(0|\ell_x|0) = (0|\ell_y|0) = (0|\ell_z|0) = 0$. This phenomenon has received the name – quenching orbital motion. Because of this, first, the magnetic field created by orbital motion of an electron is zeroed, $B = \mu_0 \frac{e}{m_e c r^3} l$, and, secondly, the forces of Coulomb repulsion between atomic electrons do not have a preferred direction.

In a strong external magnetic field, apparently, more than 20 T, ℓ - s and j - j bonds of each electron in the whole atom are torn apart, not only on external but also on internal orbitals. All electronic states are relieved from degeneration. The spin and orbital moments of each individual electron interact independently with an external magnetic field \mathbf{B} . The external magnetic field \mathbf{B} , which has a constant orientation, rigidly aligns electron orbitals with respect to its direction in accordance with their orbital magnetic moments. The average values of the orbital moments for x -, y - and z -components cease to be zero. Orbital moments of electrons are "frozen-in" in a magnetic field. The atom in "amorphous state" is transformed into an ordered, magnetic "crystal". (The situation, in which magnetic moments of nanoclusters, which interact with a constant external magnetic field, are oriented along the field, is called magnetism of "frozen-in" moments.)

In accordance with the orientation, the orbital moment ℓ of each electron and its associated orbital magnetic moment μ_ℓ precess independently around the vector direction of external magnetic field with a frequency $\omega_\ell = \mu_\ell \cdot B / \hbar$, $\mu_\ell = \mu_B \cdot \ell$. Electron orbitals with equal orbital moment ℓ precess around \mathbf{B} synchronously, with the same frequency ω_ℓ (Fig. 3a). The spin magnetic moments of electrons do not precess around \mathbf{B} , since they are

oriented only in two ways: $m_s = -1/2$ over the field and $m_s = +1/2$ against the field. The interaction energy of the orbital and spin magnetic moments of an electron is $\Delta E = -\mu_\ell \cdot \mathbf{B} - 2\mu_s \cdot \mathbf{B}$. Fig. 2b shows the splitting of energy, electronic levels in the sodium atom.

Electron orbitals align relative each other so that Coulomb repulsion forces between electrons are minimal. Fig. 3a shows schematically two orbitals with equal orbital moments ℓ and their projections m_ℓ on the Z axis parallel to \mathbf{B} , but with different directions of electron spins $s = \pm 1/2$.

The Coulomb repulsive forces, which forced, in the absence of field \mathbf{B} , the electron orbitals to freely precess, now cause the electrons to oscillate near the orbitals. If atomic electrons oscillate, in case of an ultrastrong magnetic field [2], parallel to magnetic field axis at the expense of its interaction with magnetic moments of electrons, then in case of a strong magnetic field, the atomic electrons oscillate due to Coulomb repulsive forces between electrons and compensating Coulomb attraction forces of electrons to a positively charged nucleus.

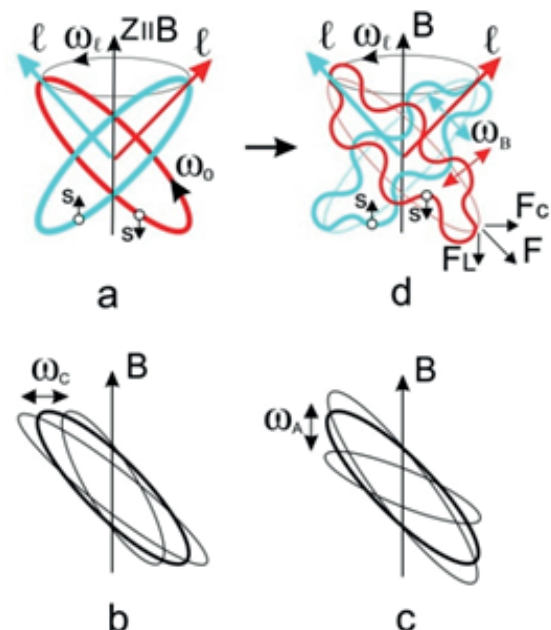


Fig. 3. *a* – precession of two orbitals in magnetic field \mathbf{B} with equal ℓ and m_ℓ , but with different $s = \pm 1/2$; *b* and *c* – electron oscillations transversely and along magnetic field direction; *d* – electron oscillations close to orbitals in a strong magnetic field.

The Coulomb repulsion force F between electrons, which are located in adjacent orbitals with the same orbital magnetic moment, has a preferential direction and it can be decomposed into force components: one force F_c acts transversely to the direction of magnetic induction vector and the second force F_L acts along the direction of magnetic induction vector (Fig. 3d). Transverse oscillations of ω_c can be represented as oscillations of entire electron orbital across the magnetic field near the equilibrium state (Fig. 3b). Longitudinal oscillations of ω_A can be represented as oscillations that stretch and compress the orbital along magnetic field direction, near the same equilibrium state (Fig. 3c). Since transverse and longitudinal forces are components of one, total force, oscillation frequencies in transverse and longitudinal directions will be the same $\omega_c = \omega_A \equiv \omega_B$ (Fig. 3d). However, oscillation amplitudes can be different. The oscillation frequency ω_B is related to electron rotation frequency on the orbital $\omega_0 = E_0/\hbar$ by the following relation [5-6]

$$\omega_B = k\sqrt{\omega_0^2 + \omega_l^2}, \text{ where } k = 1, 2, 3... \quad (1)$$

Since the rotational frequencies on the orbitals for electrons with different spins are not equal to each other: $\omega_0(s = 1/2) \neq \omega_0(s = -1/2)$, then the oscillation frequencies for them will differ $\omega_B(s = 1/2) \neq \omega_B(s = -1/2)$ even for equal numbers k (1). However, since the energy of level E_0 is much greater than the energy of its splitting due to the interaction of field \mathbf{B} both with orbital $\Delta E_\ell = \mu_c \cdot \ell \cdot B$, and spin $\Delta E_s = 2\mu_c \cdot s \cdot B$ electron magnetic moments:

$$E_0 \gg \Delta E_\ell \text{ or } \omega_0 \gg \omega_l, \quad (2)$$

$$E_0 \gg \Delta E_s \text{ or } \omega_0 \gg \omega_s, \quad (3)$$

where $\omega_s = \Delta E_s/\hbar$, then at equal numbers k , it follows from expression (2) that $\omega_B(s = 1/2) \approx \omega_0(s = 1/2)$ and $\omega_B(s = -1/2) \approx \omega_0(s = -1/2)$, and it follows from expression (3) that

$$\omega_B(s = 1/2) \approx \omega_B(s = -1/2). \quad (4)$$

For orbitals with equal ground quantum number, orbital and magnetic quantum numbers, but with different electron spins, the number k

will be equal. This is due to the fact that electron energies on the orbitals are close to each other, the electrons are in one magnetic field and, in addition, synchronized electron oscillations minimize Coulomb repulsion between them.

Thus, atomic electrons in a strong magnetic field \mathbf{B} not only rotate in orbitals that are strictly oriented and precess around the direction of the magnetic field \mathbf{B} , but the electrons additionally perform oscillations near their orbitals. Consequently, an additional degree of electron freedom appears in an atom in a strong magnetic field. A new degree of electron movement freedom generates a new quantum number for them.

It is known that a system with j degrees of freedom is described by means of generalized coordinates q_i and generalized pulses p_i ($i = 1, 2, 3, \dots, j$). Each generalized moment p_i depends on the corresponding generalized coordinate q_i only. The j quantum conditions are superimposed on the motion of a system with j degrees of freedom with j quantum numbers n_i ($i = 1, 2, 3, \dots, j$):

$$\oint p_i dq_i = 2\pi\hbar n_i \quad (n_i = 1, 2, 3, \dots; i = 1, 2, 3, \dots, j)$$

Thus, an intrinsic quantum condition is superimposed on the electron motion oscillating close to orbital, which can be correlated with the number k from equation (1). Recall that in case of plane motion of an electron along an elliptical orbit around the nucleus, the system has two degrees of freedom [7]. Therefore, two quantum conditions are superimposed on this system expressed in two quantum numbers: azimuthal n_φ and radial n_r . The energies of electron stationary states in case of elliptical orbitals are characterized by the sum of the azimuthal and radial quantum numbers $n_\varphi + n_r = n$ and they are equal to the energies of electron states in case of its motion along circular orbitals with the same values of ground quantum number n .

An atomic electron that moves in a strong magnetic field has three degrees of freedom. Consequently, it has an additional quantum number n_b . The quantum number n_b allows that

two or more electrons with different n_b have identically directed spins.

4. ELECTRON PAIRING INTO ORTHO-BOSON

If we transfer the conditions for electron pairing at superconductivity in metals to an atom, then we must observe three basic requirements:

1. The Pauli principle must be fulfilled, according to which fermions cannot be in exactly equal states;
2. Electrons should be attracted by each other (Cooper condition [8]). This attraction between electrons can be arbitrarily small;
3. The sum of pulses of two electrons in a pair must be equal to zero $P_{ec} = 0$, i.e. electrons in the pair must have equal in magnitude and opposite in the direction pulses: $\mathbf{P}_{e1} = -\mathbf{P}_{e2}$.

Atomic electrons with equal quantum numbers n , ℓ and m_ℓ , but and with antiparallel spins $s = \pm 1/2$, occupy different energy states in a strong magnetic field (Fig. 2b). For them, $\mathbf{P}_{e1} \neq -\mathbf{P}_{e2}$, so electrons cannot form a boson with $S = 0$. Consequently, paired atomic electrons should be in equal energy states, which requires equal direction of their spins $\uparrow\uparrow$, $S = 1$. Schematically, for a pair of atomic electrons the condition $\mathbf{P}_{e1} = -\mathbf{P}_{e2}$ can be realized if they are placed on the same line with atomic nucleus, opposite to each other (Fig. 4, $\mathbf{P}_{10} = -\mathbf{P}_{20}$). In addition, such a location of electron pair allows them to compensate their mutual repulsion due to attraction to a positively charged nucleus.

The second condition – presence of attraction between paired electrons, is provided by the exchange interaction [9]. It is remarkable that the exchange interaction has the character of attraction in an atom for electrons with parallel-directed spins $\uparrow\uparrow$ only.

As it is known, the exchange interaction is associated with the indistinguishability of electrons (the principle of identity). It is characterized by the magnitude of exchange energy "A". The exchange energy represents

an additional contribution to the total system energy.

It differs from zero only in case if wave functions of electrons overlap. The more the wave functions of electrons overlap, the greater is the exchange energy. In the atom, the energy of the Coulomb repulsion of electrons "C" and the exchange energy "A" are positive. (The exchange energy is negative for a hydrogen molecule). In contrast to the Coulomb electrostatic energy "C", the contribution of the exchange energy "A" to the total system energy can have different signs depending on whether the spin part of wave function is symmetric or antisymmetric. The correction ΔE to the total system energy (5) connected with the interaction of electrons, is calculated in perturbation theory and is equal to:

$$\Delta E = C \pm A, \quad (5)$$

where '+' refers to the antisymmetric $\uparrow\downarrow$ spin state $S = 0$, and '-' refers to the symmetric $\uparrow\uparrow$ spin state $S = 1$. Thus, thanks to the exchange interaction, two electrons with identically directed spins $\uparrow\uparrow$ are attracted together in an atom.

Since the exchange energy of electrons is comparable to the energy of their Coulomb repulsion, which is also compensated by the attraction to a positively charged atomic nucleus for paired electrons, it cannot be neglected in calculations. I.e., one can not consider the motion of one of the paired electrons in the field of the nucleus independent of the motion of the other electron. The motion of an electron is rigidly correlated with the motion of the second electron, as well as the probability of its finding at one or another point of space causes a point in space, at which the second electron is located with equal probability.

Electrons with identically directed spins $\uparrow\uparrow$, but with different quantum numbers n_b will be in different energy states. And the condition



Fig. 4. Antiphase rotation of two electrons around a nucleus.

$\mathbf{P}_{e1} = -\mathbf{P}_{e2}$ is not fulfilled for them. Therefore, the possibility for two electrons to have unidirectional spins at identical quantum numbers is associated with the need for additional antisymmetry in electron wave functions. Such an antisymmetry in the wave functions of the spatial motion of electrons can be ensured if, while on the same orbital, the paired electrons rotate around the nucleus ($\mathbf{P}_{10} = -\mathbf{P}_{20}$, Fig. 4) and oscillate near the orbital (${}^1\mathbf{P}_{1B} = -{}^1\mathbf{P}_{2B}$, Fig. 5a,b) in antiphase. In this case, the wave function of the spatial motion of the first electron will be an antisymmetric function relative to spatial motion of the second electron. The electron oscillations must occur both in the longitudinal and transverse magnetic field \mathbf{B} directions ($\mathbf{P}_{1B} = -\mathbf{P}_{2B}$, Fig. 5c,d). Such a motion allows two electrons in equal energy states to be in nonintersecting spatial regions. Fig. 5b-d shows one and the same electron drawn on the orbital in the form of filled and empty circles is depicted conditionally. The Fig. 5b-d shows the case $n_b = 2$.

The projections of the oscillation pulse moments for each electron in a pair by the selected direction (Z axis) are not defined. However, these moments, just like the pulses themselves, are equal and opposite to each other in the direction:

$$n_{1b} \cdot \hbar = r_1 \cdot \mathbf{P}_{1B} = r_2 \cdot (-\mathbf{P}_{2B}) = -n_{2b} \cdot \hbar.$$

With an average $\langle r_1 \rangle$ equal to the mean $\langle r_2 \rangle$, this is equivalent to the equality of the modules, but with opposite signs, the quantum numbers of electron oscillations $n_{1b} = -n_{2b}$. Thus, the Pauli principle is true for two rigidly correlated electrons, which move in a fixed way with respect to each other in three-dimensional space around the nucleus.

It should be noted that, when a strong magnetic field orders the orbital moments of electrons, it "squeezes out" their orbital spatial uncertainty to other newly formed degrees of freedom, i.e. the oscillation moments of electrons. One may say that the amount of "chaos" is preserved in a closed system, if one applies efforts to its ordering.

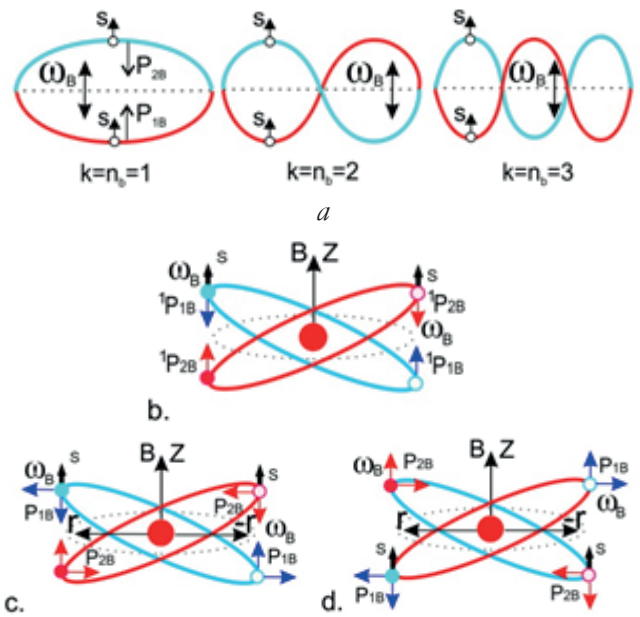


Fig. 5. a, b – antiphase oscillations of paired electrons; c, d – antiphase oscillations of two paired electrons around nucleus close to orbital.

The total wave function of two electrons is equal to the product of symmetric spin wave function of two electrons $\Psi(S)$ by the wave function of their spatial motion $\Psi[1, 2]$. It must be an antisymmetric function at rearrangement of electrons. If electrons change their places, Fig. 5c is converted to Fig. 5d. Respectively, $\Psi[r_1, r_2]$ becomes $\Psi[r_2, r_1]$. The electron oscillation direction will change to opposite direction. Both wave functions $\Psi[r_1, r_2]$ and $\Psi[r_2, r_1]$ belong to the same energy eigenvalue. Therefore, the function: $\Psi(S) \cdot \Psi[1, 2] = \Psi(S) \cdot \{\Psi[r_1, r_2] - \Psi[r_2, r_1]\}$ will become antisymmetric at electron rearrangement, but it will be symmetric with respect to the spatial reflection, if r is replaced by $(-r)$: $\Psi[-r_1, -r_2] = \Psi[r_1, r_2]$ and $\Psi[-r_2, -r_1] = \Psi[r_2, r_1]$ (Fig. 5c,d).

Thus, the pairing condition and the requirement of attraction between two electrons are automatically satisfied in a strong magnetic field due to the symmetric spin part of their wave functions $S = 1$, and the requirement of antisymmetry of wave functions of the spatial motion of electrons with respect to each other automatically leads to zero sum of their moments $P_{ee} = 0$. The fulfillment of these conditions and requirements is ensured by a rigid correlation of three-dimensional motion of two paired

electrons in the central field of the nucleus in a strong magnetic field.

5. INTRA-ATOMIC ELECTRON MAGNETIC RESONANCE

The projections of magnetic moments on magnetic field direction do not change in a constant magnetic field. The direction of magnetic moments and spins can be changed by magnetic resonance methods. Known are methods of nuclear magnetic resonance (NMR) and electron paramagnetic resonance (EPMR). The essence of these methods consists in forced reorientation of magnetic moment of the nucleus (NMR) or of electron magnetic moment (EPMR) under the action of resonant electromagnetic high-frequency or microwave fields. The scheme of methods consists in placing the atoms of substance in a homogeneous magnetic field, where electron levels of an atom are split, and a resonant HF (microwave) magnetic field is applied perpendicular to the uniform magnetic field, which causes transitions between the split electron levels. In the NMR method, electron transitions occur between the levels of hyperfine atomic structure, and in the EPMR method, they occur between the levels of fine structure of an unpaired atomic electron.

The orbital magnetic moments μ_ℓ with equal orbital moment ℓ precess around magnetic field \mathbf{B} synchronously, with equal frequency $\omega_\ell = \mu_\ell \cdot B / \hbar$, $\mu_\ell = \ell \cdot \mu_e$ (Fig. 6a). The orbital magnetic moment μ_ℓ creates an intrinsic magnetic field with a magnetic induction vector \mathbf{B}_μ , which is calculated by the formula [10]:

$$\mathbf{B}_\mu = \mu_0 \frac{3\mathbf{n}(\boldsymbol{\mu}_\ell \cdot \mathbf{n}) - \boldsymbol{\mu}_\ell}{r^3}, \quad (6)$$

where $\mu_0 = 1.26 \cdot 10^{-6}$ H/m is magnetic constant, r is the distance from electron to the point at which the field is calculated, and \mathbf{n} is a unit vector in the r direction. The magnetic induction vector \mathbf{B}_μ can be decomposed into two components: a magnetic field $\mathbf{B}_\mu^{\parallel}$ directed parallel to the homogeneous field \mathbf{B} and a magnetic field \mathbf{B}_μ^{\perp} directed perpendicular to the field \mathbf{B}

(Fig. 6a). The vector by the magnetic induction \mathbf{B}_μ and its component \mathbf{B}_μ^{\perp} precess around \mathbf{B} with a frequency $\omega_\ell = \mu_\ell \cdot B / \hbar$, $\mu_\ell = \mu_e \cdot \ell$. Once again, \mathbf{B}_μ^{\perp} precess perpendicular to \mathbf{B} . Fig. 6a shows two orbitals with equal orbital magnetic moments μ_ℓ emanating from one point and lying in the same plane with Z axis. If the last two states are permanently conserved, then perpendicular magnetic fields \mathbf{B}_μ^{\perp} , created by two magnetic moments μ_ℓ , compensate each other. However, as rotational frequencies on the orbitals for electrons with different spins are not equal to each other: $\omega_0(s = 1/2) \neq \omega_0(s = -1/2)$, there are reasons to believe that orbital magnetic moments μ_ℓ create magnetic fields, which perpendicular components \mathbf{B}_μ^{\perp} are not compensated. In addition, magnetic fields \mathbf{B}_μ^{\perp} are not compensated for the odd elements. The magnetic fields $\mathbf{B}_\mu^{\parallel}$ remain uncompensated until the whole subshell ℓ is filled.

The interaction energy of magnetic field \mathbf{B} with orbital magnetic moment of the electron is $\Delta E_\ell = -\ell \cdot \mu_e B$, with the spin magnetic moment of the electron $\Delta E_s = -2\mu_e \cdot s \cdot B$. The energy between levels for a pair of electrons $m_s = \pm 1/2$ is equal to $\Delta E m_s = 2\mu_e \cdot B$. For the p -subshell ($\ell = 1$), the energy $\Delta E m_\ell$ between neighboring levels m_ℓ is half the energy $\Delta E m_s$ (Fig. 6b). For the d -subshell ($\ell = 2$), the energy $\Delta E m_\ell$ is equal to the energy $\Delta E m_s$ (Fig. 6c). Therefore, for the d -subshell, the rotation frequency $\omega_\ell = 2 \cdot \mu_e B / \hbar$ of magnetic fields \mathbf{B}_μ coincides with transition frequency $\omega_s = \Delta E m_s / \hbar = 2 \cdot \mu_e B / \hbar$ between the spin levels $m_s = 1/2$ and $m_s = -1/2$. This enables to appear transitions between spin levels $m_s = 1/2$ and $m_s = -1/2$ stimulated by rotating magnetic fields \mathbf{B}_μ^{\perp} . In case of a p -subshell, the rotation of two oppositely directed magnetic fields \mathbf{B}_μ^{\perp} with a frequency ω_ℓ can be represented as a sum of fields rotating with multiple ω_ℓ , including frequency $2\omega_\ell$. Therefore, transitions between levels $m_s = 1/2$ and $m_s = -1/2$ stimulated by fields \mathbf{B}_μ are also possible for the p -subshell.

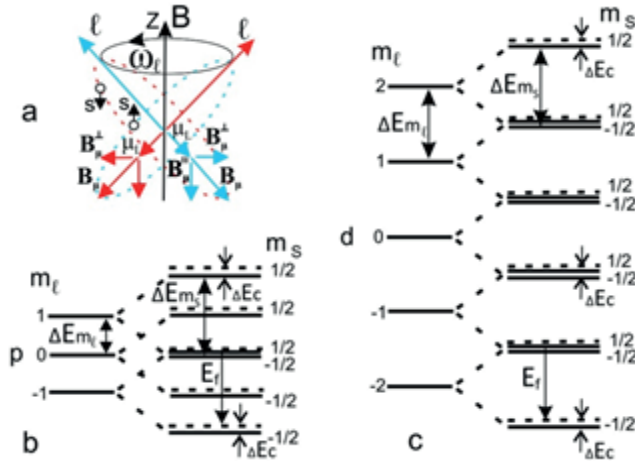


Fig. 6. a – ω_ℓ frequency precession of electron orbital magnetic moments μ_ℓ and magnetic fields \mathbf{B}_μ and \mathbf{B}_μ^\perp generated by them ; b, c – splitting of p- and d-subshells in a strong magnetic field.

Rotating magnetic fields \mathbf{B}_μ^\perp will stimulate transitions with energy release E_f (Fig. 6b,c), i.e. transitions from levels $m_s = 1/2$ to levels $m_s = -1/2$. Inverse transitions are forbidden, because they proceed with energy absorption that must be taken from somewhere, and an external generator of rotating magnetic fields \mathbf{B}_μ is absent. The transition from level $m_s = 1/2$ will occur to intermediate transport level, from which the electron pair will move to ortho-boson state. Because of increased Coulomb repulsion between electrons, transport levels will be above spin levels both for $m_s = 1/2$ and $m_s = -1/2$ by the value ΔE_c (Fig. 6). The energy ΔE_{m_s} between levels $m_s = \pm 1/2$ should be much higher than ΔE_c : $\Delta E_{m_s} \gg \Delta E_c$ (Fig. 6b,c). The transport levels in Fig. 6b,c are shown as dashed line. The energy released during the transition is $E_f = \Delta E_{m_s} - \Delta E_c$.

Consequently, in a strong magnetic field \mathbf{B} , precessing orbital magnetic moments μ_ℓ create internal, rotating magnetic fields \mathbf{B}_μ^\perp that stimulate forced transitions between atomic levels $m_s = 1/2 \rightarrow m_s = -1/2$. Thus, in a strong magnetic field, the spin-orbit interaction of internal electrons, leads, due to intra-atomic electron magnetic resonance (IAEMR), to pairing of two atomic electrons into an ortho-boson.

6. ATOM AS Z/2 ACTIVE MEDIUM

The energy between the spin levels $m_s = 1/2$ и $m_s = -1/2$ will be, in a strong magnetic field, approximately the same for all atoms, regardless of their electron shell and charge of the Z nucleus, and will be equal to $\Delta E_{m_s} = 2\mu_c \cdot B$ (with exactness up to newly arising internal magnetic fields \mathbf{B}_μ). Moreover, the atom has Z/2 such two-level systems. I.e., each atom in a strong magnetic field represents a Z/2 two level active medium.

As already mentioned, thanks to the IAEMR, an interlevel transition is performed with the emission of a photon with energy $E_f \approx 2\mu_c \cdot B$. The proton energy amounts, with an external magnetic field in the range of 10÷100 T, to $10^{-3} \div 10^{-2}$ eV, which corresponds to a frequency of 0.3-3 THz or a wavelength of 1-0.1 mm. The emitted photon E_f propagating in the active medium, stimulates the forced transitions with the same energy both inside the atom in which it was generated (Fig. 7a) and in other surrounding atoms. Thus, the Z/2 active medium will produce coherent radiation in the terahertz range. Transitions from the lower $m_s = -1/2$ level to the upper $m_s = 1/2$ under the action of the photon E_f will not occur, since the transition energy E_i is greater than E_f (Fig. 7a). Inverse transitions are unlikely, because more rapid transitions to ortho-boson states and transitions of ortho-bosons from high-lying levels to low-lying levels will occur at once (Fig. 7b). In the end, ortho-bosons will occupy the lowest-lying level. Transitions to low-lying levels will be carried out by electron ortho-bosons, probably, with the emission of two photons. Since transitions occur between internal electron levels of the atom, the energies of these photons depend on the charge of nucleus Z and lie in the range from hard ultraviolet to hard X-rays of 10^2 - 10^5 eV [11]. The energies of these transitions are characteristic for each Z. Thus, coherent radiation will be produced at other wavelengths (Fig. 7b), along with terahertz radiation. Apparently, exactly that radiation in the X-ray range was discovered by

A.V. Karabut [12-13] in experiments with a high-current glow discharge and by S.V. Adamenko in experiments with the irradiation of metals by a powerful electron beam [14]. Moreover, Karabut A.V. observed intensive generation of X-ray radiation in the form of narrowly directed beams in his experiments [13]. The diameter of the microbeam at a distance of 200 mm from the cathode was estimated to be 10-20 μm , and the angular divergence to be $\sim 10^{-4}$.

Electrons in ortho-bosons rotate around the nucleus and oscillate near the lowest-lying orbital in antiphase with frequency ω_0 ($\ell = 0$, $n_b = 1$). The phases of neighboring electrons are shifted by $360^\circ/P_c$, where P_c is the number of paired electrons in the shell. The trajectories of two moving paired electrons represent closed spirals, which are enclosed into each other and similar to the spiral of DNA molecules. The trajectories of several ortho-bosons are located on the surface of toroid and form several spirals resembling the DNA code of the main character of the film "The Fifth Element" – Lila [15]. Such a comparison is connected with the phenomenon of transmutation (transformation) of certain chemical elements into other chemical elements in microbiological systems [16-18]. Apparently, depending on the values of the magnetic field \mathbf{B} , the charge of nucleus Z and the number of

paired electrons P_c , the toroid may have a circle, an elongated or flattened ellipse in its section.

As experiments [18-20] have shown, chemical d -elements can act as catalysts to increase the efficiency of formation of ortho-bosons in a $Z/2$ active medium. This is due to the fact that rotation frequency ω_ℓ of magnetic fields \mathbf{B}_μ almost coincides, for the d -subshell, with the frequency ω_s of transition between spin levels $m_s = 1/2$ and $m_s = -1/2$. The d -elements include: $^{21}_{\text{Sc}}$ - $^{30}_{\text{Zn}}$, $^{39}_{\text{Y}}$ - $^{48}_{\text{Cd}}$, $^{57}_{\text{La}}$, $^{72}_{\text{Hf}}$ - $^{80}_{\text{Hg}}$, $^{89}_{\text{Ac}}$, $^{104}_{\text{Rf}}$ - $^{112}_{\text{Cn}}$. By chance or not, scientists engaged in the research of cold nuclear synthesis will extract Ti, Ni, Zr, Pd, and Au out of these elements.

Thus, it is possible to create sources of coherent radiation in the terahertz range and radiation ranges: from hard ultraviolet to hard X-ray $\sim 10^2$ - 10^5 eV.

7. FORMATION OF TRANSATOMS AND TRANSMOLECULES

A spin electron Bose condensate will form in the atom at lowest-lying levels. An atom possessing such Bose condensate is called the Transatom. Fig. 7c shows schematically a sodium transatom. Magnetic induction vector of sodium transatom created by electron spin magnetic moments at nucleus location has a value of $\sim 10^6$ T. The transatom due to interaction of its summarized magnetic moment $\mu_c \cdot P_c$ with external magnetic field \mathbf{B} , will precess $\Omega = \mu_c P_c B / \hbar$ (Fig. 7c) around direction \mathbf{B} .

All electron spin magnetic moments in Bose condensate are directed in one direction. These moments create a giant inhomogeneous and anisotropic magnetic field $\sim 10^6$ - 10^9 T in the entire region of atom, including in the region of nucleus location (6) [11]. This field forms an electromagnetic trap in the first electron boson orbital with a radius R_Z with magnetic field irregularity of 10^2 - 10^6 T on the nucleus diameter. Fig. 8 demonstrates, in relative units, the dependence of magnetic induction vector \mathbf{B}_s from the distance to nucleus $C(R_Z)$ along the C axis (Fig. 7c). The distance $C(R_Z)$ is normalized

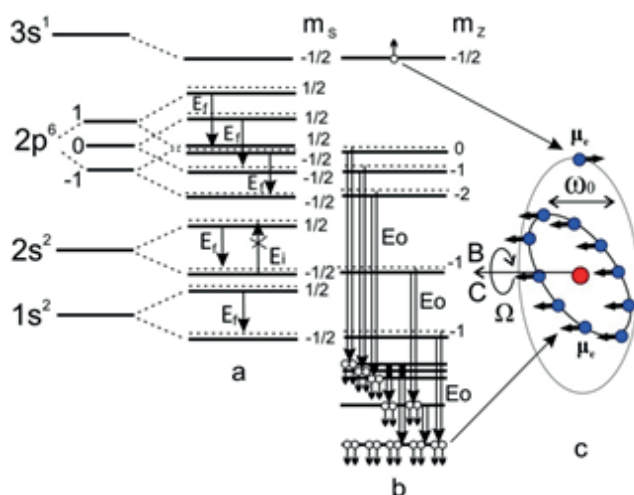


Fig. 7. Atom as $Z/2$ active medium. a – sodium atom radiation of forced photons E_p in terahertz range; b – sodium radiation realized by electron ortho-bosons; c – sodium transatom.

for $R_z = 1$. Negative values of magnetic induction vector \mathbf{B}_s mean that magnetic field in the central region of transatom is directed in the direction opposite to electron magnetic moment direction. When one or several nuclei move within a magnetic trap, an inhomogeneous and anisotropic magnetic field causes changes in the energy levels of protons and neutrons. As a result, nuclear structure and their properties change. The nuclei are transformed into Transnuclei. Transatoms with transnuclei represent a new state of matter: spin-nuclide-electron condensate [11].

The transatom has a magnetic feature. Transatoms are attracted to each other. When two transatoms converge, their electronic shells are combined into one shell, common for both nuclei. This results in the creation of a binuclear system. Other transatoms can join that system subsequently. Thus, a multinuclear system – nuclear molecule – transmolecule is formed. The transmolecule is located in the region of inhomogeneous and anisotropic magnetic field. Consequently, the space, in which transnuclei move in the transmolecule, is inhomogeneous and anisotropic. Thus, motion integrals are not conserved in transnuclear interaction: momentum conservation law, angular momentum (spin) conservation law, and, apparently, energy conservation law are violated. As a result, nonradiative, low-energy multinuclear reactions automatically take place in nuclear transmolecule [11-14, 16-27].

Not all atomic electrons, but only a part of them can, in the process of forced transitions, be transformed into ortho-bosons. Thus, each atomic nucleus Z can have $Z/2$ "chemical" transelements or "transatomic chimeras". A part of "transatomic chimera" will be represented by electrons in a paired boson state, the other part will be represented by electrons, which fill the "chimera" orbitals. Here, "chimera" orbitals should be understood as "traditional" orbitals with corrections due to magnetic and electric field influence created by transatomic paired

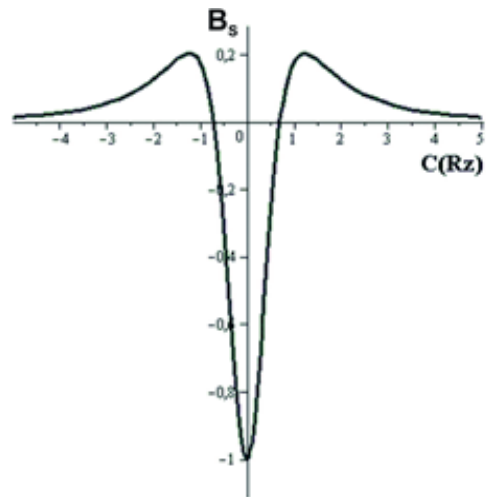


Fig. 8. Dependence of magnetic induction vector value \mathbf{B}_s in relative units along axis C .

electrons of the transatom on its unpaired electrons. Thus, many other transelements are added to the existing chemical elements in D.I. Mendeleev Table. So, if one confines himself to nuclei with Z charge from 2 to 100, then the number of transelements will be ~ 2500 .

Thus, the transatoms generated by strong magnetic fields of 20-100 T have ultrastrong magnetic fields of 10^6 - 10^9 T in their volume and at nucleus location [11]. In a strong magnetic field, atoms inevitably turn into transatoms, which inevitably enter into low-energy nuclear reactions. The proposed hypothetical mechanism for the conversion of atoms into transatoms requires experimental verification.

8. CONCLUSION

In a strong magnetic field \mathbf{B} , the uncertainty of the x -, y - and z -components of the orbital moments of internal electrons is removed. Orbital moments of all electrons are "frozen-in" in a magnetic field. For this purpose, the value of field \mathbf{B} should be comparable with magnetic fields generated by electron orbital moments \mathbf{B}_μ , i.e. more than 20 T.

Thanks to Coulomb forces, the motion of electrons in atom acquires a new degree of freedom, i.e. oscillations. Oscillations can be quantized by introducing a new quantum number.

The orbital moments of electrons precessing around the field \mathbf{B} generate their own, intra-atomic magnetic fields \mathbf{B}_μ , which also precess around the field \mathbf{B} . The components \mathbf{B}_μ (\mathbf{B}_μ^\perp) orthogonal to the field \mathbf{B} stimulate forced transitions between electronic levels differing only in the direction of electron spins $m_s = 1/2 \rightarrow m_s = -1/2$. Such transitions result into formation of ortho-bosons with $S = 1$. The possibility of existence of ortho-bosons is provided by exchange interaction between electrons and a rigid correlation in the quantum, three-dimensional motion of paired electrons around the nucleus. Ortho-bosons on the orbitals closest to nucleus create a spin electron condensate. The atomic structure changes. There is a complete reorganization of electron configurations of all atomic electrons. Atoms in a strong magnetic field inevitably turn into transatoms.

A strong magnetic field \mathbf{B} that identically interacts with all electrons of all atoms generates a $Z/2$ active medium. The $Z/2$ deexcitation of active medium is accompanied by intense coherent radiation lying in terahertz range and ultraviolet to X-ray ranges.

Spin electron condensate creates a giant inhomogeneous anisotropic magnetic field \mathbf{B}_s in the transatom volume. This field changes the structure of a nucleus, turning it into a transnucleus. In addition, the \mathbf{B}_s field changes interaction way of transnuclei, both with each other and with surrounding Bose electrons. A transnuclear transatom is a new state of matter: spin-nuclide-electronic condensate (SNEC).

The SNEC is a changed state of atomic and nuclear structure of chemical elements. The physical and chemical properties of elements change in this state. Transatoms are attracted to each other and form transmolecules with new properties that differ from those of ordinary molecules.

The SNEC transnuclei can enter into nuclear reactions. A peculiarity of these nuclear reactions is the absence of irradiation during their implementation and the absence of radioactive

isotopes in their products. Nuclear reactions occur after the formation of transmolecules automatically. Consequently, cross section values of nuclear reactions are comparable with cross sections values of atomic processes.

Spin-nuclide-electronic condensate possesses physical properties unknown up to present time. It is easy and, at the same time, difficult to predict what opportunities can be realized using these properties in science and technology. – The transatom is inexhaustible...

REFERENCES

1. Ul'yanov VI (Lenin). *Materializm i empiriokrititsizm*. Polnoe sobr. soch., 18(5):231. Moscow, Politicheskaya literatura Publ., 1968.
2. Kadomtsev BB. Tyazhely atom v sverkhsil'nom magnitnom pole [Heavy atom in an ultrastrong magnetic field]. *ZhETF*, 1970, 58(5):1765-1769 (in Russ.).
3. Kadomtsev BB, Kudryavtsev VS. Veshchestvo v sverkhsil'nom magnitnom pole [Matter in an ultrastrong magnetic field]. *ZhETF*, 1972, 62(1):144-152 (in Russ.).
4. Slichter ChP. *Principles of magnetic resonance*. New York, Harper & Row Publishers, 1963, 246 p.
5. Fock VA. Bemerkung zur Quantelung des harmonischen Oszillators im Magnetfeld. *Z.Phys.*, 1928, 47:446-448.
6. Heiss WD, Nazmitdinov RG. Orbital magnetism in small quantum dots with closed shells. *Pis'ma v ZhETF*, 1998, 68(12):870-875.
7. Matveev AN. *Atomic physics*. Moscow, Vysshaya shkola Publ., 1989, 439 p.
8. Cooper LN. Bound electron pairs in a degenerate Fermi gas. *Phys.Rev*, 1956, 104:1189.
9. Heisenberg W. Über die Spektren von Atomsystemen mit zwei Elektronen. *Z. Phys.*, 1926, 39(7):499-518.
10. Landau LD, Lifshits YeM. *Teoriya polya* [Field theory]. Moscow, Nauka Publ., 1973, 512 p.
11. Mishinsky GV. Magnitnye polya transatomov. Spinovy-nuklidny-elektronny kondensat

- [Magnetic fields of transatoms. Spin-nuclide-electronic condensate]. *International Journal of Unconventional Science*, 2017, 15-16(5):6-25 (in Russ.).
12. Karabut AB. Analiz rezultatov registratsii izbytochnoy teplovoy moshchnosti, primesnykh nuklidov s izmenennym sootnosheniem izotopov i pronikayushchego izlucheniya v eksperimentakh s silnotochnym tleyushchim razryadom [Analysis of the results of recording excess heat power, impurity nuclides with a modified natural ratio of isotopes and penetrating radiation in experiments with a high-current glow discharge]. *Proc. of 7th Russian Conference on Cold Transmutation of Nuclei of Chemical Elements* (RCCTNCE), Moscow, 2000, p. 27-35 (in Russ.).
 13. Karabut AB. Zavisimost' proizvodstva izbytochnoy teplovoy moshchnosti, produktov yadernykh reaktsiy i emissii rentgenovskogo izlucheniya ot eksperimentalnykh parametrov silnotochnogo tleyushchego razryada [Dependence of the production of excessive thermal power, products of nuclear reactions and emission of X-ray radiation on the experimental parameters of a high-current glow discharge]. *Proc. of 9th Russian Conference on Cold Transmutation of Nuclei of Chemical Elements*, Moscow, 2002, p. 86-98 (in Russ.).
 14. Adamenko SV, Selleri F, A. van der Merwe. *Controlled Nucleosynthesis. Breakthroughs in Experiment and Theory. Series: Fundamental theories in Physics*, Springer, 2007, 156, 780 p., http://www.proton21.com.ua/articles/Booklet_ru.pdf.
 15. Besson L, Kamen RM. *The Fifth Element*, film, 1997.
 16. Vysotskii VI, Kornilova AA. Nuclear transmutation of stable and radioactive isotopes in biological systems. India, Delhi, Pentagon Press, 2010.
 17. Kornilova AA. Vysotskii VI. Sintez i transmutatsiya stabil'nykh i radioaktivnykh izotopov v biologicheskikh sistemakh [Synthesis and transmutation of stable and radioactive isotopes in biological systems]. *Radioelektronika. Nanosistemy. Informatsionnye Tekhnologii* (RENSIT), 2017, 9(1):52-64 (in Russ.).
 18. Kurashov VM, Sakhno TV. Mikrobiologicheskiy sposob transmutatsii khimicheskikh elementov i prevrashcheniya izotopov khimicheskikh elementov [Microbiological method of transmutation of chemical elements and conversion of isotopes of chemical elements]. *Patent RU 2 563 511 C2* May 15, 2014.
 19. Simakin AV, Shafeev GA. Vliyaniye lazernogo oblucheniya nanochastits v vodnykh rastvorakh soli urana na aktivnost' nuklidov [The influence of laser irradiation of nanoparticles in aqueous solutions of uranium salts on the activity of the nuclides]. *Kvantovaya elektronika*, 2011, 41(7):614-618 (in Russ.).
 20. Andreev SN, Shafeev GA. Nelineynoe tusheniye radioaktivnosti vodnykh rastvorov soley nuklidov pri lazernoy ablyatsii nanochastits metallov [Nonlinear quenching of the radioactivity of aqueous solutions of salts of nuclides by laser ablation of nanoparticles of metals]. *RENSIT*, 2017, 9(1):65-73 (in Russ.).
 21. Mishinsky GV. Transatomy-transyadra i ikh svoystva [Transatoms – Transnuclei, and their properties]. *Proceedings of 18th Russian conference on cold transmutation of nuclei of chemical elements*, 2012, Moscow, pp. 94-106 (in Russ.).
 22. Mishinsky GV. Mnogoyadernye reaktzii v kondensirovannom gelii [Multinuclear reactions in condensed helium]. *RENSIT*, 2017, 9(1):94-105 (in Russ.).
 23. *Proceedings of 1-23th Russian Conference on Cold Transmutation of Nuclei of Chemical Elements* (in Russ.).
 24. *Proceedings of the 1-19th International Conferences on Cold Fusion (Condensed Matter Nuclear Science)*.

25. Balakirev VF, Krymskiy VV, Bolotov BV. et al. *Vzaimoprevrashcheniye khimicheskikh elementov* [Interconversion of chemical elements]. Ed. Balakirev VF. Ekaterinburg, UrO RAN Publ., 2003, 64 p.
26. Kuznetsov VD, Mishinsky GV, Penkov FM, Arbuzov VI, Zhemenik VI. Low energy transmutation of atomic nuclei of chemical elements. *Annales de la Fondation Louis de Broglie*, 2003, 28(2):173-214.
27. Mishinsky GV, Kuznetsov VD. Element distribution in the products of low energy transmutation. Nucleosynthesis. *Annales de la Fondation Louis de Broglie*, 2008, 33(3-4):331-356; *Proceedings of 14-th Russian Conf. on cold transmutation of nuclei of chemical elements*, 2008, Moscow, pp. 79-97 (in Russ.).

RELATIVISTIC CONTINUUM IN SPECIFIED FORCE FIELD

Stanislav A. Podosenov, Elena R. Men'kova

All-Russian Research Institute for Optical and Physical Measurements, <http://www.vniiofi.ru>
Moscow 119361, Russian Federation

Alexander A. Potapov

Kotel'nikov Institute of Radioengineering and Electronics, Russian Academy of Sciences, <http://www.cplire.ru>
Moscow 125009, Russian Federation

Jinan University, College of Information Science and Technology/College of Cyber Security, <http://www.jnu.edu.cn>
Guangzhou 510632, China

Cooperative Chinese-Russian Laboratory of Informational Technologies and Signals Fractal Processing,
Guangzhou 510632, China

Jaykov Foukzon

Center for Mathematical Sciences, Israel Institute of Technology, <http://www.technion.ac.il>
Haifa 3200003, Israel

podosenov@mail.ru, potapov@cplire.ru, jaykovfoukzon@list.ru, e_menkova@mail.ru

Abstract. A continuum motion in the flat Minkowski space in the specified force field is considered. When movement the relative space-time curvature stipulated by the noncoincidence of the hypersurface orthogonal to world lines of basis particles with the simultaneity hypersurface arises. The anholonomic mathematical apparatus and its continua application is developed. Metrics for relative 4-interval element squares for the arbitrary continuum motion and special cases are found. The acceleration addition law is obtained. It turns out that exact solutions of the Einstein's equations for the isotropic cosmological model for the strongly evacuated gas and for the critical density follow from solutions of the Newtonian gas dynamics Euler's equations.

Keywords: space-time, curvature tensor, reference frame, Born's rigidity, Minkowski, Riemann, Einstein, coordinates, Christoffel, hypersurfaces.

UDC 530.12, 531.134, 537.9

Bibliography - 25 references

Received 10.11.2017

RENSIT, 2017, 9(2):161-180

DOI: 10.17725/rensit.2017.09.161

CONTENTS

1. INTRODUCTION (161)
 2. RELATIVE NRF CURVATURE TENSOR IN SPECIAL RELATIVITY (SR) (162)
 3. ELEMENT SQUARE OF RELATIVE CONTINUUM INTERVAL IN LAGRANGIAN COORDINATES (170)
 - 3.1. Uniformly rotating RF (170)
 - 3.2. Relativistic (nonrigid) uniformly accelerated NRF (171)
 4. ACCELERATION ADDITION LAW, RELATIVE NRF CURVATURE TENSOR IN MINKOWSKI SPACE (172)
 5. RELATIVE CONTINUUM CURVATURE TENSOR IN NEWTON MECHANICS (175)
 6. CONCLUSION (178)
- REFERENCES (178)

1. INTRODUCTION

Generally a continuum motion description in an inertial reference frame (IRF) and a transition to a noninertial reference frame (NRF) demands a going out of the flat space-time [1]. That is connected with both a specifying of a force field affecting on the medium particles and a condition superposition on motion continuum characteristic by means of the structure equations [1-5]. These equations connect the Riemannian-Christoffel tensor and the strain velocity tensors, the rotational velocity tensors and the first curvature vectors of medium particle world lines. As a result the set of equations is an overdetermined system and it is not realized in Minkowski space.

This system is solved when considering of a medium motion in the Riemannian space or in a general case in the metric connectivity space. However if one does not impose characteristic continuum additional conditions and restrict just an integration of motion equations, for example, in a flat space-time, then no going out of the flat space-time is occur. When using nonholonomic transformations the curvature tensor obtained from Minkowski space in the nonholonomic coordinates is identically zero. However this zero tensor can be divided into two nonzero parts. One of them is expressed in an ordinary way with the Christoffel symbols and the other one depends on the moving medium characteristics [2-5].

2. RELATIVE NRF CURVATURE TENSOR IN SPECIAL RELATIVITY (SR)

The essence of our NRF mapping method from IRF is in finding of transformation rules of geometric objects prescribed in Galilean coordinates of Minkowski space (Euler variables) by means of affine frames of Lagrangian comoving NRF. First this method was developed in [6]. “Space” reference marks of the NRF are located in hypersurfaces orthogonal to world lines of medium particles (anholonomic in the presence of rotations) and time vectors coincide with the field of 4-velocities V^μ tangent to world lines.

The continuum motion law in an arbitrary force field in Minkowski space is described by equations

$$x^\mu = \Psi^\mu(y^{\hat{k}}, \xi^{\hat{0}}), \tag{1}$$

where x^μ are the Eulerian coordinates and $y^{\hat{k}}$ are the Lagrangian coordinates which are constant along each fixed world line, $(1/c)\xi^{\hat{0}}$ is the time parameter, for example, proper time. Let μ indices belong to Eulerian coordinates and $\hat{\mu}$ indices belong to Lagrangian ones. Differentiating (1) with respect to $y^{\hat{k}}$ and

$\xi^{\hat{0}}$ in each space-time point, we obtain the affine frame. We note that in the general case time $\partial x^\mu / \partial \xi^{\hat{0}}$ and space $\partial x^\mu / \partial y^{\hat{k}}$ vectors are not orthogonal to each other. However, the reference marks with orthogonal “time” and “space” vectors can be constructed from relation (1), but these reference marks are not a result of 4-radius vector differentiation with respect to $y^{\hat{k}}$ and $\xi^{\hat{0}}$ Lagrangian coordinates. These reference marks are anholonomic and corresponding Lamé coefficients have the form

$$h_k^\mu = (\delta_\varepsilon^\mu - V^\mu V_\varepsilon) \frac{\partial \Psi^\varepsilon}{\partial y^{\hat{k}}}, \quad h_0^\mu = \frac{\partial \Psi^\mu}{\partial \xi^{\hat{0}}} = V^\mu, \tag{2}$$

$$h_\mu^{\hat{k}} = \frac{\partial y^{\hat{k}}}{\partial x^\mu}, \quad h_\mu^{\hat{0}} = V_\mu.$$

For anholonomic coordinates connectivity coefficients $\Gamma_{\hat{a}\hat{b}}^{\hat{\sigma}}$ in Minkowski space can be presented in the form [7]

$$\Gamma_{\hat{a}\hat{b}}^{\hat{\sigma}} = h_\varepsilon^{\hat{\sigma}} \frac{\hat{\partial} h_b^\varepsilon}{\hat{\partial} y^{\hat{a}}} = -h_b^\varepsilon \frac{\hat{\partial} h_\varepsilon^{\hat{\sigma}}}{\hat{\partial} y^{\hat{a}}}, \tag{3}$$

where hereinafter $\hat{\partial} / \hat{\partial} y^{\hat{a}}$ will be directional derivatives determined as

$$\frac{\hat{\partial}}{\hat{\partial} y^{\hat{0}}} = \frac{\hat{\partial}}{\hat{\partial} \xi^{\hat{0}}} = V^\mu \frac{\partial}{\partial x^\mu}, \quad \frac{\hat{\partial}}{\hat{\partial} y^{\hat{k}}} = h_k^\mu \frac{\partial}{\partial x^\mu}. \tag{4}$$

It is proposed in formula (3) that Galilean coordinates have been selected in Minkowski space. For arbitrary curvilinear coordinates the connectivity formula has the form

$$\Gamma_{\hat{a}\hat{b}}^{\hat{\sigma}} = -h_b^\varepsilon \frac{\hat{\partial} h_\varepsilon^{\hat{\sigma}}}{\hat{\partial} y^{\hat{a}}} + \Gamma_{\nu\lambda}^\mu h_\mu^{\hat{\sigma}} h_b^\nu h_a^\lambda, \tag{3a}$$

where $\Gamma_{\nu\lambda}^\mu$ is the connectivity in Minkowski space. We form the nonholonomy object $C_{\hat{a}\hat{b}}^{\hat{\sigma}}$ from Lamé coefficients

$$C_{\hat{a}\hat{b}}^{\hat{\sigma}} = -\Gamma_{[\hat{a}\hat{b}]}^{\hat{\sigma}} = \frac{1}{2} \left(h_b^\varepsilon \frac{\hat{\partial} h_\varepsilon^{\hat{\sigma}}}{\hat{\partial} y^{\hat{a}}} - h_a^\varepsilon \frac{\hat{\partial} h_\varepsilon^{\hat{\sigma}}}{\hat{\partial} y^{\hat{b}}} \right) = \frac{1}{2} h_a^\nu h_b^\varepsilon \left(\frac{\partial h_\varepsilon^{\hat{\sigma}}}{\partial x^\nu} - \frac{\partial h_\nu^{\hat{\sigma}}}{\partial x^\varepsilon} \right). \tag{5}$$

Following to Schouten [7] for anholonomic transformations the $\Gamma_{\hat{a}\hat{b}}^{\hat{\sigma}}$ connectivity has the form

$$\Gamma_{\hat{a}\hat{b}}^{\hat{\sigma}} = \left\{ \begin{matrix} \hat{\sigma} \\ \hat{a}\hat{b} \end{matrix} \right\} + T_{\hat{a}\hat{b}}^{\hat{\sigma}}, \quad T_{\hat{a}\hat{b}}^{\hat{\sigma}} = -C_{\hat{a}\hat{b}}^{\hat{\sigma}} + g_{\hat{\alpha}\hat{\epsilon}} g^{\hat{\sigma}\hat{\nu}} C_{\hat{b}\hat{\nu}}^{\hat{\epsilon}} + g_{\hat{b}\hat{\epsilon}} g^{\hat{\sigma}\hat{\nu}} C_{\hat{\alpha}\hat{\nu}}^{\hat{\epsilon}}. \quad (6)$$

If one calculates the Riemannian-Christoffel's tensor in Minkowski space, it is identically zero. It is clear that the transition into the Lagrangian comoving NRF by means of Lamé coefficients (2) does not make the curvature tensor differed from zero and it results in identity [7]

$$R_{\hat{a}\hat{b}\hat{\gamma}}^{\dots\hat{\mu}} = 2\hat{\partial}_{[\hat{\alpha}} \Gamma_{\hat{b}}^{\hat{\mu}}]_{\hat{\gamma}} + 2\Gamma_{[\hat{\alpha}|\hat{\epsilon}|}^{\hat{\mu}} \Gamma_{\hat{b}}^{\hat{\epsilon}}]_{\hat{\gamma}} + 2C_{\hat{a}\hat{b}}^{\hat{\epsilon}} \Gamma_{\hat{\epsilon}\hat{\gamma}}^{\hat{\mu}} \equiv 0. \quad (7)$$

It follows from (6) and (7) that

$$\hat{R}_{\hat{a}\hat{b}\hat{\gamma}}^{\dots\hat{\mu}} = -2\hat{\nabla}_{[\hat{\alpha}} T_{\hat{b}}^{\hat{\mu}}]_{\hat{\gamma}} - 2T_{[\hat{\alpha}|\hat{\epsilon}|}^{\hat{\mu}} T_{\hat{b}}^{\hat{\epsilon}}]_{\hat{\gamma}} - 2C_{\hat{a}\hat{b}}^{\hat{\epsilon}} T_{\hat{\epsilon}\hat{\gamma}}^{\hat{\mu}}. \quad (8)$$

In relation (8) the curvature tensor is calculated by means of Christoffel's symbols $\left\{ \begin{matrix} \hat{\sigma} \\ \hat{a}\hat{b} \end{matrix} \right\}$, obtained from metric coefficients

$$\hat{g}_{\hat{a}\hat{b}} = g_{\mu\nu} h_{\hat{a}}^{\mu} h_{\hat{b}}^{\nu}, \quad \hat{g}_{\hat{0}\hat{0}} = 1, \quad \hat{g}_{\hat{0}\hat{k}} = 0, \quad (9)$$

where $g_{\mu\nu}$ is the metric tensor in Eulerian coordinates of Minkowski space. Christoffel's symbols are calculated in the usual way with the substitution of partial derivatives by directional derivatives, and $\hat{\nabla}_{\hat{\alpha}}$ operator is calculated by means of the Christoffel's connectivity.

Thus, anholonomic transformations resulted in the curvature tensor differed from zero and calculated by means of the Christoffel's connectivity (6).

As it would be followed further from the analysis of motion equations, $\hat{R}_{\hat{a}\hat{b}\hat{\gamma}}^{\dots\hat{\mu}}$ curvature tensor may be called as *relative NRF curvature tensor*.

For anholonomic coordinates following commutation relations exist [7]

$$\frac{\hat{\partial}^2}{\hat{\partial}y^{\hat{b}}\hat{\partial}y^{\hat{\alpha}}} - \frac{\hat{\partial}^2}{\hat{\partial}y^{\hat{\alpha}}\hat{\partial}y^{\hat{b}}} = 2C_{\hat{a}\hat{b}}^{\hat{\gamma}} \frac{\hat{\partial}}{\hat{\partial}y^{\hat{\gamma}}}. \quad (10)$$

The concrete form of a nonholonomy object depends on selected Lamé coefficients which are determined against the time parameter

choice along world lines of basis particles. For example, if one selects a proper time as a time parameter (2) then the calculation of the nonholonomy object results in relations

$$C_{\hat{k}\hat{l}}^{\hat{0}} = \Omega_{\hat{k}\hat{l}}, \quad 2C_{\hat{0}\hat{k}}^{\hat{0}} = F_{\hat{k}}, \quad C_{\hat{a}\hat{b}}^{\hat{k}} = 0, \quad (11)$$

where

$$\Omega_{\hat{k}\hat{l}} = \Omega_{\mu\nu} h_{\hat{k}}^{\mu} h_{\hat{l}}^{\nu}, \quad F_{\hat{k}} = F_{\mu} h_{\hat{k}}^{\mu}. \quad (12)$$

In receiving (12) one can use relations, where the rotational velocity tensor and the vector of 4-acceleration are considered in Eulerian coordinates of Minkowski space and they are projected with Lamé parameters into the comoving Lagrangian NRF. For the nonholonomy object (11) commutation relations (10) reduce to the form

$$\frac{\hat{\partial}^2}{\hat{\partial}y^{\hat{k}}\hat{\partial}y^{\hat{j}}} - \frac{\hat{\partial}^2}{\hat{\partial}y^{\hat{j}}\hat{\partial}y^{\hat{k}}} = 2\Omega_{\hat{l}\hat{k}} \frac{\hat{\partial}}{\hat{\partial}y^{\hat{0}}}, \quad (13)$$

$$\frac{\hat{\partial}^2}{\hat{\partial}y^{\hat{k}}\hat{\partial}y^{\hat{0}}} - \frac{\hat{\partial}^2}{\hat{\partial}y^{\hat{0}}\hat{\partial}y^{\hat{k}}} = F_{\hat{k}} \frac{\hat{\partial}}{\hat{\partial}y^{\hat{0}}}.$$

Commutation relations (13) are equivalent to Zel'manov commutation relations [8]. From metric (9), expansion (6) and Lamé coefficients (2) we obtain

$$\left\{ \begin{matrix} \hat{0} \\ \hat{0}\hat{0} \end{matrix} \right\} = \left\{ \begin{matrix} \hat{k} \\ \hat{0}\hat{0} \end{matrix} \right\} = \left\{ \begin{matrix} \hat{0} \\ \hat{0}\hat{k} \end{matrix} \right\} = 0, \quad \left\{ \begin{matrix} \hat{0} \\ \hat{k}\hat{l} \end{matrix} \right\} = -\Sigma_{\hat{k}\hat{l}},$$

$$\left\{ \begin{matrix} \hat{k} \\ \hat{n}\hat{l} \end{matrix} \right\} = \lambda_{\hat{n}\hat{l}}^{\hat{k}}, \quad \left\{ \begin{matrix} \hat{k} \\ \hat{0}\hat{n} \end{matrix} \right\} = \Sigma_{\hat{n}}^{\hat{k}}, \quad T_{\hat{0}\hat{k}}^{\hat{0}} = -F_{\hat{k}}, \quad T_{\hat{0}\hat{0}}^{\hat{k}} = F^{\hat{k}}, \quad (14)$$

$$T_{\hat{m}\hat{l}}^{\hat{k}} = T_{\hat{m}\hat{l},\hat{k}} = T_{\hat{k}\hat{0}}^{\hat{0}} = 0, \quad T_{\hat{0}\hat{l}}^{\hat{k}} = T_{\hat{l}\hat{0}}^{\hat{k}} = \Omega_{\hat{l}}^{\hat{k}}, \quad T_{\hat{k}\hat{l}}^{\hat{0}} = -\Omega_{\hat{k}\hat{l}}.$$

As

$$\Sigma_{\hat{k}\hat{l}} + \Omega_{\hat{k}\hat{l}} = h_{\hat{k}}^{\nu} h_{\hat{l}}^{\mu} \nabla_{\nu} V_{\mu}, \quad (15)$$

one could show differentiating with respect to $y^{\hat{0}}$ that the following kinematic identity exists

$$\frac{\hat{\partial}}{\hat{\partial}y^{\hat{0}}} (\Sigma_{\hat{k}\hat{l}} + \Omega_{\hat{k}\hat{l}}) \equiv$$

$$\equiv \hat{g}^{\hat{m}\hat{n}} (\Sigma_{\hat{i}\hat{n}} + \Omega_{\hat{i}\hat{n}}) (\Sigma_{\hat{k}\hat{m}} + \Omega_{\hat{k}\hat{m}}) + \hat{\nabla}_{\hat{k}} F_{\hat{l}} - F_{\hat{k}} F_{\hat{l}},$$

whence alternating we obtain

$$\frac{\hat{\partial}}{\hat{\partial}y^{\hat{0}}} \Omega_{\hat{k}\hat{l}} \equiv \hat{\nabla}_{[\hat{k}} F_{\hat{l}]}. \quad (17)$$

Balancing of expression (16) gives

$$\begin{aligned} \frac{\hat{\partial}}{\hat{\partial}y^{\hat{0}}} \Sigma_{\hat{k}\hat{i}} &\equiv \\ &\equiv \hat{g}^{\hat{m}\hat{n}} (\Sigma_{\hat{i}\hat{n}} + \Omega_{\hat{i}\hat{n}}) (\Sigma_{\hat{k}\hat{m}} + \Omega_{\hat{k}\hat{m}}) + \hat{\nabla}_{\hat{k}} F_{\hat{l}} - F_{\hat{k}} F_{\hat{l}}. \end{aligned} \quad (18)$$

Although the relative NRF curvature tensor is calculated by means of Christoffel's symbols in the same way as an usual curvature tensor in the Riemannian space, however in expressing of a connectivity by a metric tensor, directional derivatives are used instead of usual partial derivatives. Therefore, the relative curvature tensor has features, which arise because of noncommutativity of directional derivatives. For example, the known Richi identity will have the form

$$\begin{aligned} \hat{R}_{\hat{a}\hat{b},\hat{\gamma}}^{\hat{\mu}} + \hat{R}_{\hat{b}\hat{\gamma},\hat{a}}^{\hat{\mu}} + \hat{R}_{\hat{\gamma}\hat{a},\hat{b}}^{\hat{\mu}} &= \\ = 2 \left[C_{\hat{a}\hat{b}}^{\hat{\sigma}} \left\{ \begin{matrix} \hat{\mu} \\ \hat{\sigma}\hat{\gamma} \end{matrix} \right\} + C_{\hat{b}\hat{\gamma}}^{\hat{\sigma}} \left\{ \begin{matrix} \hat{\mu} \\ \hat{\sigma}\hat{a} \end{matrix} \right\} + C_{\hat{\gamma}\hat{a}}^{\hat{\sigma}} \left\{ \begin{matrix} \hat{\mu} \\ \hat{\sigma}\hat{b} \end{matrix} \right\} \right]. \end{aligned} \quad (18a)$$

For Bianchi identity we have the expression

$$\begin{aligned} \hat{\nabla}_{\hat{\varepsilon}} \hat{R}_{\hat{a}\hat{b},\hat{\gamma}}^{\hat{\mu}} + \hat{\nabla}_{\hat{a}} \hat{R}_{\hat{b}\hat{\varepsilon},\hat{\gamma}}^{\hat{\mu}} + \hat{\nabla}_{\hat{b}} \hat{R}_{\hat{\varepsilon}\hat{a},\hat{\gamma}}^{\hat{\mu}} &= \\ = 2C_{\hat{\varepsilon}\hat{a}}^{\hat{\sigma}} \hat{R}_{\hat{b}\hat{\sigma},\hat{\gamma}}^{\hat{\mu}} + 2C_{\hat{a}\hat{b}}^{\hat{\sigma}} \hat{R}_{\hat{\varepsilon}\hat{\sigma},\hat{\gamma}}^{\hat{\mu}} + 2C_{\hat{b}\hat{\varepsilon}}^{\hat{\sigma}} \hat{R}_{\hat{a}\hat{\sigma},\hat{\gamma}}^{\hat{\mu}}, \end{aligned} \quad (19)$$

to prove that it is convenient to pass into the local geodesic coordinate system.

One can represent the curvature tensor (8) in other equivalent form

$$\begin{aligned} \hat{R}_{\hat{a}\hat{b},\hat{\gamma}}^{\hat{\mu}} &= 2\hat{\partial}_{[\hat{a}} \left\{ \begin{matrix} \hat{\mu} \\ \hat{b}]\hat{\gamma}} \right\} + 2 \left\{ \begin{matrix} \hat{\mu} \\ [\hat{a}|\hat{\varepsilon}] \end{matrix} \right\} \left\{ \begin{matrix} \hat{\varepsilon} \\ \hat{b}]\hat{\gamma}} \right\} + 2C_{\hat{a}\hat{b}}^{\hat{\varepsilon}} \left\{ \begin{matrix} \hat{\mu} \\ \hat{\varepsilon}\hat{\gamma}} \right\} \equiv \\ \equiv K_{\hat{a}\hat{b},\hat{\gamma}}^{\hat{\mu}} + 2C_{\hat{a}\hat{b}}^{\hat{\varepsilon}} \left\{ \begin{matrix} \hat{\mu} \\ \hat{\varepsilon}\hat{\gamma}} \right\}. \end{aligned} \quad (20)$$

$K_{\hat{a}\hat{b},\hat{\gamma}}^{\hat{\mu}}$ is not a tensor relatively holonomic transformations of Lagrangian variables, although its form is not differed from an usual curvature tensor. However substitution of partial derivatives by directional derivatives results in the modification of transformation properties.

As we consider two kinds of covariant derivatives $\hat{\nabla}_{\hat{a}}$ and $\tilde{\nabla}_{\hat{a}}$ calculated by means of Christoffel's part of connectivity (6) and the complete anholonomic connectivity (3)

correspondingly then matched conditions have to be satisfied. One can prove that the directly under test relation is such a matching condition

$$\tilde{\nabla}_{\hat{a}} \hat{g}_{\hat{b}\hat{\gamma}} = \hat{\nabla}_{\hat{a}} \hat{g}_{\hat{b}\hat{\gamma}} = 0. \quad (21)$$

Let's carry out a further analysis of the relative curvature tensor. Let's consider the expression

$$0 = \hat{\nabla}_{[\hat{a}} \hat{\nabla}_{\hat{\mu}]} \hat{g}_{\hat{\lambda}\hat{\nu}} = C_{\hat{\mu}\hat{a}}^{\hat{\gamma}} \frac{\hat{\partial} \hat{g}_{\hat{\lambda}\hat{\nu}}}{\hat{\partial} y^{\hat{\gamma}}} - K_{\hat{a}\hat{\mu},(\hat{\lambda}\hat{\nu})}. \quad (22)$$

Using (20) we find

$$\hat{R}_{\hat{a}\hat{b},(\hat{\gamma}\hat{\mu})} = 0. \quad (23)$$

Convoluting (18) on $\hat{\mu}$ and $\hat{\gamma}$ we obtain

$$\hat{R}_{[\hat{a}\hat{b}]} = C_{\hat{a}\hat{b}}^{\hat{\sigma}} \left\{ \begin{matrix} \hat{\mu} \\ \hat{\sigma}\hat{\mu} \end{matrix} \right\} + C_{\hat{b}\hat{\gamma}}^{\hat{\sigma}} \left\{ \begin{matrix} \hat{\gamma} \\ \hat{\sigma}\hat{a} \end{matrix} \right\} + C_{\hat{\gamma}\hat{a}}^{\hat{\sigma}} \left\{ \begin{matrix} \hat{\gamma} \\ \hat{\sigma}\hat{b} \end{matrix} \right\}. \quad (24)$$

It follows from (24) that the relative Ricci tensor is not symmetrical. Symmetry absence of Ricci tensor is indirectly connected with the expression

$$\hat{R}_{\hat{a}\hat{b},\hat{\gamma}\hat{\mu}} \neq \hat{R}_{\hat{\gamma}\hat{\mu},\hat{a}\hat{b}}. \quad (25)$$

Let's form a tensor having the same symmetry properties as the usual Riemann-Christoffel tensor. We construct the tensor

$$\tilde{R}_{\hat{a}\hat{b},\hat{\gamma}\hat{\mu}} = \frac{1}{2} (\hat{R}_{\hat{a}\hat{b},\hat{\gamma}\hat{\mu}} + \hat{R}_{\hat{\gamma}\hat{\mu},\hat{a}\hat{b}}), \quad (26)$$

Using previous formulae one can show that the constructed tensor satisfies the usual Ricci identity

$$\tilde{R}_{\hat{a}\hat{b},\hat{\gamma}\hat{\mu}} + \tilde{R}_{\hat{b}\hat{\gamma},\hat{a}\hat{\mu}} + \tilde{R}_{\hat{\gamma}\hat{a},\hat{b}\hat{\mu}} = 0, \quad (27)$$

which results in Ricci tensor symmetry $\tilde{R}_{\hat{a}\hat{b}} = \tilde{R}_{\hat{b}\hat{a}}$. We shall point out the equality

$$\begin{aligned} \hat{R}_{\hat{b}\hat{\mu},\hat{\gamma}\hat{a}} - \hat{R}_{\hat{\gamma}\hat{a},\hat{b}\hat{\mu}} &= C_{\hat{\gamma}\hat{b}}^{\hat{\sigma}} \frac{\hat{\partial} \hat{g}_{\hat{\mu}\hat{a}}}{\hat{\partial} y^{\hat{\sigma}}} + \\ + C_{\hat{b}\hat{a}}^{\hat{\sigma}} \frac{\hat{\partial} \hat{g}_{\hat{\gamma}\hat{\mu}}}{\hat{\partial} y^{\hat{\sigma}}} + C_{\hat{\mu}\hat{\gamma}}^{\hat{\sigma}} \frac{\hat{\partial} \hat{g}_{\hat{b}\hat{a}}}{\hat{\partial} y^{\hat{\sigma}}} + C_{\hat{a}\hat{\mu}}^{\hat{\sigma}} \frac{\hat{\partial} \hat{g}_{\hat{b}\hat{\gamma}}}{\hat{\partial} y^{\hat{\sigma}}}. \end{aligned} \quad (28)$$

Calculation of curvature tensor components $\tilde{R}_{\hat{a}\hat{b},\hat{\gamma}\hat{\mu}}$ gives

$$\begin{aligned}\tilde{R}_{\hat{a}\hat{b},\hat{c}\hat{q}} &= \Omega_{\hat{q}\hat{b}}\Omega_{\hat{a}\hat{c}} - \Omega_{\hat{q}\hat{a}}\Omega_{\hat{b}\hat{c}} - 2\Omega_{\hat{a}\hat{b}}\Omega_{\hat{c}\hat{q}}, \\ \tilde{R}_{\hat{a}\hat{b},\hat{c}\hat{0}} &= 2\hat{\nabla}_{[\hat{a}}\Omega_{\hat{b}]\hat{c}} + 2\Omega_{\hat{a}\hat{b}}F_{\hat{c}} - \frac{1}{2}F_{\hat{b}}\Sigma_{\hat{a}\hat{c}} + \frac{1}{2}F_{\hat{a}}\Sigma_{\hat{c}\hat{b}}, \quad (29) \\ \tilde{R}_{\hat{0}\hat{b},\hat{c}\hat{0}} &= F_{\hat{b}}F_{\hat{c}} - \hat{\nabla}_{(\hat{b}}F_{\hat{c})} - 2\Sigma_{(\hat{b}}^{\hat{n}}\Omega_{\hat{c})\hat{n}} + \Omega_{\hat{n}\hat{c}}\Omega_{\hat{b}}^{\hat{n}}.\end{aligned}$$

Space components of the relative curvature tensor can be represented in the form

$$\tilde{R}_{\hat{a}\hat{b},\hat{c}\hat{q}} = \tilde{R}_{\hat{a}\hat{b},\hat{c}\hat{q}} - 2\Sigma_{\hat{q}[\hat{a}}\Sigma_{\hat{b}]\hat{c}}, \quad (30)$$

where $\tilde{R}_{\hat{a}\hat{b},\hat{c}\hat{q}}$ is the three-dimensional curvature tensor on the hypersurface orthogonal to world lines of medium particles. This hypersurface is anholonomic when rotations are present. From (29) and (30) we find

$$\tilde{R}_{\hat{a}\hat{b},\hat{c}\hat{q}} = 2\Sigma_{\hat{q}[\hat{a}}\Sigma_{\hat{b}]\hat{c}} + \Omega_{\hat{q}\hat{b}}\Omega_{\hat{a}\hat{c}} - \Omega_{\hat{q}\hat{a}}\Omega_{\hat{b}\hat{c}} - 2\Omega_{\hat{a}\hat{b}}\Omega_{\hat{c}\hat{q}}. \quad (31)$$

If there are no rotations the expression (31) passes into one obtained earlier by the author from other considerations [9].

Let's introduce a number of useful identities

$$\begin{aligned}\hat{V}_{\hat{\alpha}} &= h_{\hat{\alpha}}^{\mu}V_{\mu} = \delta_{\hat{\alpha}}^{\hat{0}}, \quad \tilde{\nabla}_{[\hat{\alpha}}\tilde{\nabla}_{\hat{\beta}]\hat{\gamma}}\hat{V}_{\hat{\gamma}} = 0 = \\ &= \hat{\nabla}_{[\hat{\alpha}}\tilde{\nabla}_{\hat{\beta}]\hat{\gamma}}\hat{V}_{\hat{\gamma}} - \mathbb{T}_{[\hat{\alpha}\hat{\beta}]}^{\hat{\epsilon}}\tilde{\nabla}_{\hat{\epsilon}}\hat{V}_{\hat{\gamma}} - \mathbb{T}_{[\hat{\alpha}|\hat{\gamma}]}^{\hat{\epsilon}}\tilde{\nabla}_{\hat{\beta}]\hat{\epsilon}}\hat{V}_{\hat{\gamma}}, \quad (32) \\ \tilde{\nabla}_{\hat{k}}\hat{V}_{\hat{l}} &= \Sigma_{\hat{k}\hat{l}} + \Omega_{\hat{k}\hat{l}}, \quad \tilde{\nabla}_{\hat{0}}\hat{V}_{\hat{l}} = F_{\hat{l}}, \\ \tilde{\nabla}_{\hat{k}}\hat{V}_{\hat{0}} &= \tilde{\nabla}_{\hat{0}}\hat{V}_{\hat{l}} = 0.\end{aligned}$$

It follows from (32) that

$$\hat{\nabla}_{[\hat{a}}\Sigma_{\hat{b}]\hat{c}} + \hat{\nabla}_{[\hat{a}}\Omega_{\hat{b}]\hat{c}} = -\Omega_{\hat{a}\hat{b}}F_{\hat{c}}. \quad (33)$$

Executing the circular permutation of \hat{a} , \hat{b} , \hat{c} indices in (33) we obtain two additional identities, summing up these ones with (33) we have the identity

$$\begin{aligned}\hat{\nabla}_{\hat{a}}\Omega_{\hat{b}\hat{c}} + \hat{\nabla}_{\hat{b}}\Omega_{\hat{c}\hat{a}} + \hat{\nabla}_{\hat{c}}\Omega_{\hat{a}\hat{b}} + \\ + F_{\hat{a}}\Omega_{\hat{b}\hat{c}} + F_{\hat{b}}\Omega_{\hat{c}\hat{a}} + F_{\hat{c}}\Omega_{\hat{a}\hat{b}} = 0.\end{aligned} \quad (34)$$

The similar identity is obtained in [8]. Using expressions (18) and (33) we write (29) in the form

$$\begin{aligned}\tilde{R}_{\hat{a}\hat{b},\hat{c}\hat{0}} &= -\hat{\nabla}_{[\hat{a}}\Sigma_{\hat{b}]\hat{c}} - \frac{1}{2}F_{\hat{b}}\Sigma_{\hat{a}\hat{c}} + \frac{1}{2}F_{\hat{a}}\Sigma_{\hat{c}\hat{b}}, \\ \tilde{R}_{\hat{0}\hat{b},\hat{c}\hat{0}} &= -\frac{\hat{\partial}\Sigma_{\hat{b}\hat{c}}}{\hat{\partial}y^{\hat{0}}} + \Sigma_{\hat{c}}^{\hat{n}}\Sigma_{\hat{b}\hat{n}}.\end{aligned} \quad (35)$$

It follows from (29) and (35) that for Born rigid irrotational NRF the relative curvature tensor is equal to zero.

For Ricci tensor components we have¹

$$\begin{aligned}\tilde{R}_{\hat{b}\hat{c}} &= -\frac{\hat{\partial}\Sigma_{\hat{b}\hat{c}}}{\hat{\partial}y^{\hat{0}}} + \Sigma_{\hat{n}}^{\hat{n}}\Sigma_{\hat{b}\hat{c}} + 2\Sigma_{\hat{c}}^{\hat{n}}\Sigma_{\hat{b}\hat{n}} + \tilde{R}_{\hat{b}\hat{c}} \equiv \\ &\equiv F_{\hat{b}}F_{\hat{c}} - \hat{\nabla}_{(\hat{b}}F_{\hat{c})} - 2\Sigma_{(\hat{b}}^{\hat{n}}\Omega_{\hat{c})\hat{n}} + \Omega_{\hat{n}\hat{b}}\Omega_{\hat{c}}^{\hat{n}}, \\ \tilde{R}_{\hat{b}\hat{0}} &= -\hat{\nabla}_{\hat{a}}\Omega_{\hat{b}}^{\hat{a}} - 2\Omega_{\hat{a}\hat{b}}F^{\hat{a}} - \frac{1}{2}F_{\hat{a}}\Sigma_{\hat{a}\hat{b}} + \frac{1}{2}F_{\hat{b}}\Sigma_{\hat{c}}^{\hat{c}} \equiv \\ &\equiv \hat{\nabla}_{\hat{a}}\Sigma_{\hat{b}}^{\hat{a}} - \hat{\nabla}_{\hat{b}}\Sigma_{\hat{a}}^{\hat{a}} + \frac{1}{2}F_{\hat{b}}\Sigma_{\hat{a}}^{\hat{a}} - \frac{1}{2}F^{\hat{a}}\Sigma_{\hat{a}\hat{b}}, \\ \tilde{R}_{\hat{0}\hat{0}} &= -\frac{\hat{\partial}\Sigma_{\hat{b}}^{\hat{b}}}{\hat{\partial}y^{\hat{0}}} - \Sigma_{\hat{n}\hat{c}}\Sigma^{\hat{n}\hat{c}} \equiv \\ &\equiv F_{\hat{n}}F^{\hat{n}} - \hat{\nabla}_{\hat{n}}F^{\hat{n}} + \Omega_{\hat{n}\hat{b}}\Omega^{\hat{b}\hat{n}}.\end{aligned} \quad (36)$$

For the scalar curvature we obtain

$$\tilde{R} = 2F_{\hat{n}}F^{\hat{n}} - 2\hat{\nabla}_{\hat{n}}F^{\hat{n}} + \Omega_{\hat{n}\hat{b}}\Omega^{\hat{b}\hat{n}}. \quad (37)$$

We find truncated Bianchi identity from identity (19)

$$\begin{aligned}\hat{\nabla}_{\hat{\alpha}}\left(\tilde{R}^{\hat{\epsilon}\hat{\alpha}} - \frac{1}{2}\hat{g}^{\hat{\epsilon}\hat{\alpha}}\tilde{R}\right) &= -\hat{\nabla}_{\hat{\alpha}}\hat{R}^{[\hat{\epsilon}\hat{\alpha}]} + \\ &+ 2C_{\hat{\alpha}\hat{\sigma}}^{\hat{\epsilon}}\left(\hat{R}^{\hat{\sigma}\hat{\alpha}} + \hat{R}^{[\hat{\sigma}\hat{\alpha}]}\right) + C_{\hat{b}\hat{\alpha},\hat{\sigma}}\hat{R}^{\hat{\epsilon}\hat{\sigma},\hat{b}\hat{\alpha}}.\end{aligned} \quad (38)$$

One can see from expression (38) that the NRF Einstein tensor being in parenthesis in the first member of the equality is essentially differed from the GR Einstein tensor. For that tensor the second member of the equality is identically zero.

¹We point out that curvature tensors are determined accurate within a mathematical character by different authors. For example, in [10] and [11] curvature tensors coincide and they are differed from the curvature tensor used in this part on the basis of [7] by the sign. The Ricci tensor in [7, 11] and in our case is obtained by means of the convolution on the first and fourth indices and in [10] the convolution is realized on the first and third indices. Therefore Ricci tensors and the scalar curvature in [7, 10] and in our case coincide and they are differed from [11] by the sign.

Let's compare obtained results with A.L. Zel'manov ones [8] introducing for convenience the designations used in [8].

$$\begin{aligned} \hat{g}_{\hat{a}\hat{b}} &= -h_{ab}, \quad \Sigma_{\hat{a}\hat{b}} = -\frac{1}{c}D_{ab}, \quad \Omega_{\hat{c}\hat{a}} = -\hat{A}_{ca}, \\ \Sigma_{\hat{a}}^{\hat{a}} &= \frac{1}{c}D, \quad \Sigma_{\hat{c}}^{\hat{c}} = \frac{1}{c}D_c^n, \quad \Omega_{\hat{c}}^\alpha = \frac{1}{c}A_c^a, \\ F_{\hat{b}} &= \frac{1}{c^2}F_b, \quad F^{\hat{a}} = -\frac{1}{c^2}F^a, \\ \frac{\hat{\partial}}{\hat{\partial}y^{\hat{k}}} &= \frac{* \partial}{\partial x^k}, \quad \frac{\hat{\partial}}{\hat{\partial}y^{\hat{0}}} = \frac{1}{c} \frac{* \partial}{\partial t}. \end{aligned} \tag{38a}$$

Using relations (36) we obtain following identities in Zel'manov designations

$$\begin{aligned} \frac{* \partial D_{ik}}{\partial t} - (D_{ij} + A_{ij})(D_k^j + A_k^j) + DD_{ik} - D_{ij}D_k^j + \\ + 3A_{ij}A_k^j + \hat{\nabla}_{(i}F_{k)} - \frac{1}{c^2}F_iF_k + c^2\tilde{R}_{ik} &\equiv 0, \\ \hat{\nabla}_j(h^{ij}D - D^{ij} - A^{ij}) + \frac{2}{c^2}F_iA^{ij} &\equiv 0, \\ \frac{* \partial D}{\partial t} + D_{jk}D^{kj} + A_{jk}A^{kj} + \hat{\nabla}_jF^j - \frac{1}{c^2}F_jF^j &\equiv 0. \end{aligned} \tag{39}$$

First members of identities in (39) are Ricci tensor components specifying the first member of Einstein equations in the chronometric invariant theory (CIT). In our case these components are equal to zero. Obtained result is not unexpected. An initial space in which a continuum motion is studied was the flat Minkowski space. The origin of the relative curvature tensor differed from zero is stipulated for the division of zero anholonomic curvature tensor of the flat space-time into two nonzero parts.

If the initial space was Riemannian (as in GR) then the curvature tensor of the initial space prescribed in the anholonomic comoving Lagrangian NRF would add to the first member of equality (8). It had to result in the change of some kinematic identities. In particular in the second member of identity (33) the term will be added

$$\tilde{\nabla}_{[\hat{a}}\tilde{\nabla}_{\hat{b}}]\hat{V}^{\hat{c}} = -\frac{1}{2}R_{\hat{a}\hat{b}\hat{c}}^{\hat{d}}.$$

Making a convolution on \hat{a} and \hat{c} , raising \hat{b} index in the new identity we obtain the expression $R^{\hat{b}\hat{0}}$ of Ricci tensor component in Zel'manov theory.

The purpose of the investigation proposed in this article is the separation of the space-time curvature contribution stipulated for the noninertiality of the observers moving together with the medium in an arbitrary force field. As the field of 4-velocities V_μ appears as the integration result of the relativistic continuum motion equation in a flat space-time then the expansion

$$\nabla_\mu V_\nu = \Sigma_{\mu\nu} + \Omega_{\mu\nu} + V_\mu F_\nu,$$

saves as mathematical identity.

Although the law of continuum motion in Lagrangian coordinates (1) is holonomic, "space" vectors of affine frames connecting adjacent Lagrangian particles can not appear as a result of differentiation of 4-radius vector x^μ on $y^{\hat{k}}$ Lagrangian coordinates, since the hypersurface of simultaneous events is not orthogonal to world lines of medium particles, when a proper time is used as a time parameter. Therefore the nonholonomy object differed from zero arises from the physical demand of an "allocation" of space reference marks on the hypersurface orthogonal to world lines.

Form of the nonholonomy object depends on the selection of a time parameter. For the interval element we find

$$dS^2 = dy^{\hat{0}2} + g_{\mu\theta}^* \frac{\partial \Psi^\mu}{\partial y^{\hat{n}}} \frac{\partial \Psi^\nu}{\partial y^{\hat{k}}} dy^{\hat{n}} dy^{\hat{k}}, \tag{40}$$

$$g_{\mu\nu}^* = g_{\mu\nu} - V_\mu V_\nu.$$

$g_{\mu\nu}^*$ is the projection operator in Minkowski space projecting tensors on the hypersurface orthogonal to world lines of basis particles

$$dy^{\hat{0}} = d\xi^{\hat{0}} + V_\mu \frac{\partial \Psi^\mu}{\partial y^{\hat{n}}} dy^{\hat{n}} = V_\mu dx^\mu. \tag{41}$$

One can see from (41) that $dy^{\hat{0}}$ is not a total differential, that is $y^{\hat{0}}$ is the anholonomic coordinate.

Interval element (40) is equivalent to a fragmentation of four-dimensional interval by two parts in the comoving NRF. One part $dy^{\hat{0}} = V_{\mu} dx^{\mu}$ is the time element of the observer moving together with the medium and other part is the element of three-dimensional interval on the hypersurface orthogonal to world lines of medium particles. Similar fragmentation is presented in [8] and [12]. As in the comoving NRF obvious relations are valid

$$V^{\hat{k}} = h^{\hat{k}\mu} V_{\mu} = \frac{dy^{\hat{k}}}{d\xi^{\hat{0}}} = 0, \quad (42)$$

$$V_{\hat{k}} = V_{\mu} \frac{\partial \Psi^{\mu}}{\partial y^{\hat{k}}} = g_{\hat{k}\hat{\alpha}} V^{\hat{\alpha}} = g_{\hat{k}\hat{0}} V^{\hat{0}} = \frac{g_{\hat{k}\hat{0}}}{\sqrt{g_{\hat{0}\hat{0}}}},$$

then the space interval element in Lagrangian comoving NRF has the form

$$dl^2 = \left(\begin{array}{c} g_{\hat{n}\hat{0}} g_{\hat{k}\hat{0}} \\ g_{\hat{0}\hat{0}} \end{array} - g_{\hat{n}\hat{k}} \right) dy^{\hat{n}} dy^{\hat{k}}. \quad (43)$$

The interval element (43) coincides with the well-known relation [10]. We point out that relations (42) and (43) are general and they do not depend on concrete form of Lamé parameters (2).

The constructed relative curvature tensor is the tensor relatively anholonomic transformations. It is interesting to construct the relative curvature tensor corresponding to the usual generally covariant Riemannian-Christoffel tensor relatively arbitrary holonomic transformations.

In accordance with (6) the nonholonomic connectivity is expanded into the Christoffel's connectivity part and the sum of anholonomy objects. Christoffel's connectivity part is calculated by the metric tensor (9)

$$\left\{ \begin{array}{c} \hat{\sigma} \\ \hat{\alpha}\hat{b} \end{array} \right\} = \frac{1}{2} \hat{g}^{\hat{\sigma}\hat{\gamma}} \left(\hat{\partial}_{\hat{\alpha}} \hat{g}_{\hat{b}\hat{\gamma}} + \hat{\partial}_{\hat{b}} \hat{g}_{\hat{\gamma}\hat{\alpha}} - \hat{\partial}_{\hat{\gamma}} \hat{g}_{\hat{\alpha}\hat{b}} \right), \quad (44)$$

$$\hat{\partial}_{\hat{\alpha}} \equiv \frac{\hat{\partial}}{\hat{\partial} y^{\hat{\alpha}}}.$$

Obviously connectivity (44) differs from usual holonomic one, as directional derivatives are

present in connectivity (44) instead of partial derivatives. On the basis of the directional derivative determination and using (2) we have

$$\hat{\partial}_{\hat{\alpha}} = h_{\hat{\alpha}}^{\mu} \frac{\partial}{\partial x^{\mu}} = \frac{\partial}{\partial y^{\hat{\alpha}}} + L_{\hat{\alpha}} \frac{\partial}{\partial s}, \quad L_{\hat{\alpha}} \equiv \hat{V}_{\hat{\alpha}} - V_{\hat{\alpha}}, \quad (45)$$

$$\hat{V}_{\hat{\alpha}} = h_{\hat{\alpha}}^{\mu} V_{\mu} = \delta_{\hat{\alpha}}^{\hat{0}}, \quad V_{\hat{\alpha}} = V_{\mu} \frac{\partial x^{\mu}}{\partial y^{\hat{\alpha}}},$$

where the differentiation on $y^{\hat{0}}$ is equivalent to the differentiation on $\xi^{\hat{0}}$ or on the length s along basis world lines.

It follows from (45) that $L_{\hat{0}} = 0$.

From (6) and (45) we find

$$\left\{ \hat{\alpha}\hat{b}, \hat{\gamma} \right\} = \tilde{\Gamma}_{\hat{a}\hat{b}, \hat{\gamma}} + \tilde{\tilde{\Gamma}}_{\hat{a}\hat{b}\hat{\gamma}},$$

$$\tilde{\tilde{\Gamma}}_{\hat{a}\hat{b}\hat{\gamma}} = L_{\hat{b}} \Sigma_{\hat{\gamma}\hat{a}} + L_{\hat{\alpha}} \Sigma_{\hat{\gamma}\hat{b}} - L_{\hat{\gamma}} \Sigma_{\hat{a}\hat{b}}, \quad (46)$$

$$\Sigma_{\hat{\gamma}\hat{a}} = \frac{1}{2} \frac{\partial \hat{g}_{\hat{a}\hat{b}}}{\partial s}, \quad \Sigma_{\hat{0}\hat{0}} = \Sigma_{\hat{0}\hat{k}} = 0,$$

where $\tilde{\Gamma}_{\hat{a}\hat{b}, \hat{\gamma}}$ is the holonomic Christoffel connectivity calculated in accordance with metric (9). On the basis of the analysis carried out the anholonomic connectivity determined by expansion (6) can be presented in the form

$$\Gamma_{\hat{a}\hat{b}}^{\hat{\sigma}} = \tilde{\Gamma}_{\hat{a}\hat{b}}^{\hat{\sigma}} + \Pi_{\hat{a}\hat{b}}^{\hat{\sigma}}, \quad \Pi_{\hat{a}\hat{b}}^{\hat{\sigma}} = \tilde{\Pi}_{\hat{a}\hat{b}}^{\hat{\sigma}} + \tilde{\tilde{\Pi}}_{\hat{a}\hat{b}}^{\hat{\sigma}}. \quad (47)$$

Substituting in (7) the anholonomic connectivity $\Gamma_{\hat{a}\hat{b}}^{\hat{\sigma}}$ by the connectivity sum from (47) and taking into account (45) and (6) we obtain the expansion

$$R_{\hat{a}\hat{b}\hat{\gamma}}^{\dots\hat{\mu}} = 2\partial_{[\hat{\alpha}} \tilde{\Gamma}_{\hat{b}}^{\hat{\mu}}]_{\hat{\gamma}} + 2\partial_{[\hat{\alpha}} \Pi_{\hat{b}}^{\hat{\mu}}]_{\hat{\gamma}} +$$

$$+ 2L_{[\hat{\alpha}} \frac{\partial \Gamma_{\hat{b}}^{\hat{\mu}}]_{\hat{\gamma}}}{\partial s} + 2\Gamma_{[\hat{\alpha}|\hat{\epsilon}]}^{\hat{\mu}} \Gamma_{\hat{b}]_{\hat{\gamma}}}^{\hat{\epsilon}} + 2C_{\hat{\alpha}\hat{\beta}}^{\hat{\epsilon}} \Gamma_{\hat{\epsilon}\hat{\gamma}}^{\hat{\mu}} \equiv 0. \quad (48)$$

From expansion (48) one can select the term in explicit form

$$\tilde{\tilde{K}}_{\hat{a}\hat{b}\hat{\gamma}}^{\dots\hat{\mu}} = 2\partial_{[\hat{\alpha}} \tilde{\Gamma}_{\hat{b}}^{\hat{\mu}}]_{\hat{\gamma}} + 2\tilde{\tilde{\Gamma}}_{[\hat{\alpha}|\hat{\epsilon}]}^{\hat{\mu}} \tilde{\tilde{\Gamma}}_{\hat{b}]_{\hat{\gamma}}}^{\hat{\epsilon}}, \quad (49)$$

which corresponds to usual generally covariant relatively holonomic transformations Riemannian-Christoffel tensor. From (48) and (49) we have

$$-\tilde{\tilde{K}}_{\hat{a}\hat{b}\hat{\gamma}}^{\dots\hat{\mu}} = 2\nabla_{[\hat{\alpha}} \Pi_{\hat{b}}^{\hat{\mu}}]_{\hat{\gamma}} + 2\Pi_{[\hat{\alpha}|\hat{\epsilon}]}^{\hat{\mu}} \Pi_{\hat{b}]_{\hat{\gamma}}}^{\hat{\epsilon}} + 2C_{\hat{\alpha}\hat{\beta}}^{\hat{\epsilon}} \Gamma_{\hat{\epsilon}\hat{\gamma}}^{\hat{\mu}} +$$

$$+ 2L_{[\hat{\alpha}} \frac{\partial \Gamma_{\hat{b}}^{\hat{\mu}}]_{\hat{\gamma}}}{\partial s}. \quad (50)$$

It is necessary to make following remarks concerning formula (50):

1. Covariant derivative in the second member of (50) is calculated in an ordinary way (as for a tensor) in accordance with the holonomic Christoffel connectivity from $\Pi_{\hat{a}\hat{b}}^{\hat{\sigma}}$ object. This object is not a tensor relatively holonomic transformations.
2. All values including into the second member of equality (identity) (50) also are not tensors relatively holonomic transformations. However their combination is a generally covariant tensor.

Thus, in the Lagrangian comoving reference frame one can introduce three connectivities in a general coordination: absolute anholonomic connectivity $\Gamma_{\hat{\varepsilon}\hat{\gamma}}^{\hat{\mu}}$, calculated in accordance with (3), relative anholonomic connectivity $\left\{ \begin{smallmatrix} \hat{\sigma} \\ \hat{a}\hat{b} \end{smallmatrix} \right\}$, specified by means of expansion (6) and relative holonomic connectivity $\tilde{\Gamma}_{\hat{a}\hat{b},\hat{\gamma}}$, obtained from expansion (46).

It is clear that it is possible only in the case if covariant derivatives from the metric tensor (9) for each connectivity are equal to zero. Let us prove that it is right. Using formulae (3), (9) and substituting them into the expression

$$\tilde{\nabla}_{\hat{\mu}}\hat{g}_{\hat{a}\hat{b}} = \hat{\partial}_{\hat{\mu}}\hat{g}_{\hat{a}\hat{b}} - \Gamma_{\hat{\mu}\hat{a}}^{\hat{\nu}}\hat{g}_{\hat{\nu}\hat{b}} - \Gamma_{\hat{\mu}\hat{b}}^{\hat{\nu}}\hat{g}_{\hat{a}\hat{\nu}}, \quad (51)$$

we ascertain that $\tilde{\nabla}_{\hat{\mu}}\hat{g}_{\hat{a}\hat{b}} \equiv 0$.

Using expansion (6) by means of (51) we find

$$\hat{\nabla}_{\hat{\mu}}\hat{g}_{\hat{a}\hat{b}} = \tilde{\nabla}_{\hat{\mu}}\hat{g}_{\hat{a}\hat{b}} + T_{\hat{\mu}\hat{a}}^{\hat{\nu}}\hat{g}_{\hat{\nu}\hat{b}} + T_{\hat{\mu}\hat{b}}^{\hat{\nu}}\hat{g}_{\hat{a}\hat{\nu}}. \quad (52)$$

As in the last formula the sum of two connectivity affine deformation tensors² forms zero, then $\hat{\nabla}_{\hat{\mu}}\hat{g}_{\hat{a}\hat{b}} = \tilde{\nabla}_{\hat{\mu}}\hat{g}_{\hat{a}\hat{b}} = 0$.

Finally from the equality

²We point out that unlike $\Pi_{\hat{b}\hat{\gamma}}^{\hat{\mu}}$ objects $T_{\hat{b}\hat{\gamma}}^{\hat{\mu}}$ are the tensors relatively anholonomic transformations. To prove that it is enough to calculate covariant derivatives of an arbitrary vector on connectivities $\Gamma_{\hat{\varepsilon}\hat{\gamma}}^{\hat{\mu}}$ and $\left\{ \begin{smallmatrix} \hat{\mu} \\ \hat{\varepsilon}\hat{\gamma} \end{smallmatrix} \right\}$ and to subtract one derivative from the other.

$$\nabla_{\hat{\mu}}\hat{g}_{\hat{a}\hat{b}} = \hat{\nabla}_{\hat{\mu}}\hat{g}_{\hat{a}\hat{b}} + T_{\hat{\mu}\hat{a},\hat{b}}^* + T_{\hat{\mu}\hat{b},\hat{a}}^* - 2L_{\hat{\mu}}\Sigma_{\hat{a}\hat{b}}, \quad (53)$$

$$T_{\hat{\mu}\hat{a},\hat{b}}^* = L_{\hat{\mu}}\Sigma_{\hat{a}\hat{b}} + L_{\hat{a}}\Sigma_{\hat{\mu}\hat{b}} - L_{\hat{b}}\Sigma_{\hat{\mu}\hat{a}}$$

it follows that

$$T_{\hat{\mu}\hat{a},\hat{b}}^* + T_{\hat{\mu}\hat{b},\hat{a}}^* - 2L_{\hat{\mu}}\Sigma_{\hat{a}\hat{b}} = 0. \quad (54)$$

Therefore we have

$$\tilde{\nabla}_{\hat{\mu}}\hat{g}_{\hat{a}\hat{b}} = \hat{\nabla}_{\hat{\mu}}\hat{g}_{\hat{a}\hat{b}} = \nabla_{\hat{\mu}}\hat{g}_{\hat{a}\hat{b}} = 0. \quad (55)$$

The mathematical apparatus developed in this paragraph describing properties of Lagrangian co-moving reference frames with prescribed law of motion (1) proposed that the proper time appeared in (1) as a time parameter. However often in describing the transition from IRF to NRF other time parameter is used, for example, the IRF time.

Therefore it is interesting to develop such an apparatus which is suitable for an arbitrary time parameter. We shall consider in (1) that $\xi^{\hat{0}}$ is the arbitrary time parameter. For 4-velocity V^{μ} in Lagrangian variables the relation is valid

$$V^{\mu} = \Theta \frac{\partial \Psi^{\mu}}{\partial \xi^{\hat{0}}}, \quad (56)$$

where Θ multiplier is determined from the normalizing condition of 4-velocity per unit.

$$\Theta^2 = \frac{1}{g_{\mu\nu} \frac{\partial \Psi^{\mu}}{\partial \xi^{\hat{0}}} \frac{\partial \Psi^{\nu}}{\partial \xi^{\hat{0}}}}. \quad (57)$$

Corresponding Lamé coefficients have the form

$$h_k^{\mu} = \left(\delta_{\varepsilon}^{\mu} - V^{\mu} V_{\varepsilon} \right) \frac{\partial \Psi^{\varepsilon}}{\partial y^k}, \quad h_0^{\mu} = \frac{\partial \Psi^{\mu}}{\partial \xi^{\hat{0}}} = \frac{V^{\mu}}{\Theta}, \quad (58)$$

$$h_{\mu}^k = \frac{\partial y^k}{\partial x^{\mu}} \rightarrow h_{\mu}^{\hat{0}} = \Theta V_{\mu}.$$

One can represent connectivity coefficients $\Gamma_{\hat{a}\hat{b}}^{\hat{\sigma}}$ in Minkowski space for anholonomic coordinates in the form (3) and expansion (6). We form the nonholonomy object $C_{\hat{a}\hat{b}}^{\hat{\sigma}}$ (5) from Lamé coefficients. Concrete form of the nonholonomy object depends on selected

Lamé coefficients which are determined depending on the time parameter along world lines of basis particles. For case (58) we find

$$C_{\hat{k}\hat{l}}^{\hat{0}} = \Theta \Omega_{\hat{k}\hat{l}}, \quad 2C_{\hat{0}\hat{k}}^{\hat{0}} = F_{\hat{k}} - \frac{\hat{\partial} \ln \Theta}{\hat{\partial} y^{\hat{k}}}, \quad C_{\hat{a}\hat{b}}^{\hat{k}} = 0, \quad (59)$$

where

$$\Omega_{\hat{k}\hat{l}} = \Omega_{\mu\nu} h_{\hat{k}}^{\mu} h_{\hat{l}}^{\nu}, \quad F_{\hat{k}} = F_{\mu} h_{\hat{k}}^{\mu}. \quad (60)$$

Metric coefficients for Lamé parameters (58) have the form

$$\hat{g}_{\hat{a}\hat{b}} = g_{\mu\nu} h_{\hat{a}}^{\mu} h_{\hat{b}}^{\nu}, \quad \hat{g}_{\hat{0}\hat{0}} = \frac{1}{\Theta^2}, \quad \hat{g}_{\hat{0}\hat{k}} = 0, \quad (61)$$

where $g_{\mu\nu}$ is the metric tensor in Eulerian coordinates of Minkowski space. Christoffel symbols are calculated in the usual way with substitution of partial derivatives by directional derivatives, and $\hat{\nabla}_{\hat{a}}$ operator is calculated by means of Christoffel connectivity. Commutation relations for directional derivatives are determined by general formulae (10)

$$\begin{aligned} \frac{\hat{\partial}^2}{\hat{\partial} y^{\hat{k}} \hat{\partial} y^{\hat{l}}} - \frac{\hat{\partial}^2}{\hat{\partial} y^{\hat{l}} \hat{\partial} y^{\hat{k}}} &= 2\Theta \Omega_{\hat{l}\hat{k}} \frac{\hat{\partial}}{\hat{\partial} y^{\hat{0}}} = 2\Omega_{\hat{l}\hat{k}} \frac{\partial}{\partial s}, \\ \frac{\hat{\partial}^2}{\hat{\partial} y^{\hat{k}} \hat{\partial} y^{\hat{0}}} - \frac{\hat{\partial}^2}{\hat{\partial} y^{\hat{0}} \hat{\partial} y^{\hat{k}}} &= \left(F_{\hat{k}} - \frac{\hat{\partial} \ln \Theta}{\hat{\partial} y^{\hat{k}}} \right) \frac{\hat{\partial}}{\hat{\partial} y^{\hat{0}}} = \\ &= \frac{1}{\Theta} \left(F_{\hat{k}} - \frac{\hat{\partial} \ln \Theta}{\hat{\partial} y^{\hat{k}}} \right) \frac{\partial}{\partial s}. \end{aligned} \quad (62)$$

For tensor components of the connectivity affine deformation we find

$$\begin{aligned} T_{\hat{0}\hat{k},\hat{0}} &= - \left(F_{\hat{k}} - \frac{\hat{\partial} \ln \Theta}{\hat{\partial} y^{\hat{k}}} \right) \frac{1}{\Theta^2}, \\ T_{\hat{0}\hat{0},\hat{k}} &= \left(F_{\hat{k}} - \frac{\hat{\partial} \ln \Theta}{\hat{\partial} y^{\hat{k}}} \right) \frac{1}{\Theta^2}, \\ T_{\hat{m}\hat{l},\hat{k}} &= T_{\hat{k}\hat{0},\hat{0}} = 0, \quad T_{\hat{0}\hat{l},\hat{k}} = T_{\hat{l}\hat{0},\hat{k}} = \frac{1}{\Theta} \Omega_{\hat{l}\hat{k}}, \\ T_{\hat{k}\hat{l},\hat{0}} &= - \frac{1}{\Theta} \Omega_{\hat{k}\hat{l}}. \end{aligned} \quad (63)$$

Construction of the relative anholonomic and holonomic curvature tensor is executed

in accordance with the same rules as earlier. Directional derivatives are connected with partial derivatives by the formula

$$\hat{\partial}_{\hat{a}} = h_{\hat{a}}^{\mu} \frac{\partial}{\partial x^{\mu}} = \frac{\partial}{\partial y^{\hat{a}}} + L_{\hat{a}} \frac{\partial}{\partial \xi^{\hat{0}}}, \quad (64)$$

$$L_{\hat{a}} \equiv \left(\delta_{\hat{a}}^{\hat{0}} - \Theta V_{\hat{a}} \right), \quad V_{\hat{a}} = V_{\mu} \frac{\partial x_{\mu}}{\partial y^{\hat{a}}}.$$

In accordance with (6) the anholonomic connectivity is expanded into the Christoffel connectivity part and the sum of nonholonomy objects. Christoffel connectivity part is calculated by the metric tensor (9) in accordance with formula (44). Obviously, that connectivity (44) differs from usual holonomic connectivity. In connectivity (44) directional derivatives are used instead of partial derivatives. On the basis of the determination of the directional derivative using (2) and (64) we find

$$\begin{aligned} \{ \hat{a}\hat{b}, \hat{\gamma} \} &= \tilde{\Gamma}_{\hat{a}\hat{b},\hat{\gamma}} + \tilde{\Gamma}_{\hat{a}\hat{b}\hat{\gamma}}, \\ \tilde{\Gamma}_{\hat{a}\hat{b}\hat{\gamma}} &= \frac{1}{\Theta} \left[L_{\hat{b}} \Sigma_{\hat{\gamma}\hat{a}} + L_{\hat{a}} \Sigma_{\hat{\gamma}\hat{b}} - L_{\hat{\gamma}} \Sigma_{\hat{a}\hat{b}} \right], \end{aligned} \quad (65)$$

$$\Sigma_{\hat{\gamma}\hat{a}} = \frac{1}{2} \Theta \frac{\partial \hat{g}_{\hat{a}\hat{b}}}{\partial \xi^{\hat{0}}}, \quad \Sigma_{\hat{0}\hat{0}} = \Sigma_{\hat{0}\hat{k}} = 0,$$

where $\tilde{\Gamma}_{\hat{a}\hat{b},\hat{\gamma}}$ is the holonomic Christoffel connectivity calculated in accordance with metric (61) for which we have

$$\begin{aligned} \tilde{\Gamma}_{\hat{0},\hat{k}\hat{l}} &= - \frac{1}{2} \frac{\partial \hat{g}_{\hat{k}\hat{l}}}{\partial \xi^{\hat{0}}}, \quad \tilde{\Gamma}_{\hat{0},\hat{0}\hat{l}} = \frac{1}{2} \frac{\partial \hat{g}_{\hat{0}\hat{0}}}{\partial y^{\hat{l}}}, \quad \tilde{\Gamma}_{\hat{0},\hat{0}\hat{0}} = \frac{1}{2} \frac{\partial \hat{g}_{\hat{0}\hat{0}}}{\partial y^{\hat{0}}}, \\ \tilde{\Gamma}_{\hat{n},\hat{0}\hat{l}} &= \frac{1}{2} \frac{\partial \hat{g}_{\hat{n}\hat{l}}}{\partial y^{\hat{0}}}, \quad \tilde{\Gamma}_{\hat{n},\hat{0}\hat{0}} = - \frac{1}{2} \frac{\partial \hat{g}_{\hat{0}\hat{0}}}{\partial y^{\hat{n}}}, \quad \tilde{\Gamma}_{\hat{k}\hat{l}}^{\hat{n}} = \tilde{\Lambda}_{\hat{k}\hat{l}}^{\hat{n}}, \end{aligned} \quad (65a)$$

where $\tilde{\Lambda}_{\hat{k}\hat{l}}^{\hat{n}}$ are the three-dimensional Christoffel symbols formed from three-dimensional tensor $\hat{\gamma}_{\hat{k}\hat{l}} = -\hat{g}_{\hat{k}\hat{l}}$.

The relative holonomic curvature tensor can be calculated in accordance with (49) or (50). The calculation in accordance with (49) results in relations

$$\begin{aligned}
 -\tilde{K}_{\hat{0}\hat{k},\hat{l}\hat{m}} &= \sqrt{\hat{g}_{\hat{0}\hat{0}}} \left(\nabla_{\hat{m}} \Sigma_{\hat{k}\hat{l}} - \nabla_{\hat{l}} \Sigma_{\hat{k}\hat{m}} \right), \\
 \tilde{K}_{\hat{i}\hat{k},\hat{l}\hat{m}} &= P_{\hat{i}\hat{k},\hat{l}\hat{m}} - \left(\Sigma_{\hat{k}\hat{l}} \Sigma_{\hat{i}\hat{m}} - \Sigma_{\hat{k}\hat{m}} \Sigma_{\hat{l}\hat{i}} \right), \\
 -\tilde{K}_{\hat{0}\hat{k},\hat{0}\hat{m}} &= -\hat{g}_{\hat{0}\hat{0}} \left(\frac{\partial \Sigma_{\hat{k}\hat{m}}}{\partial S} - \hat{g}^{\hat{q}\hat{r}} \Sigma_{\hat{k}\hat{q}} \Sigma_{\hat{m}\hat{r}} \right) - \\
 & - \frac{1}{2} \left[\frac{\partial^2 \hat{g}_{\hat{0}\hat{0}}}{\partial y^{\hat{k}} \partial y^{\hat{m}}} - \frac{1}{2} \hat{g}_{\hat{0}\hat{0}} \frac{\partial \hat{g}_{\hat{0}\hat{0}}}{\partial y^{\hat{i}}} \frac{\partial \hat{g}_{\hat{0}\hat{0}}}{\partial y^{\hat{m}}} - \Lambda_{\hat{k}\hat{m}}^{\hat{n}} \frac{\partial \hat{g}_{\hat{0}\hat{0}}}{\partial y^{\hat{n}}} \right].
 \end{aligned} \tag{65b}$$

It follows from (65) for Born rigid motions (that is at $\Sigma_{\hat{a}\hat{b}} = 0$) holonomic and anholonomic Christoffel symbols coincide, however relative anholonomic and holonomic curvature tensors are differed from each other due to the anholonomic addition (see (20)).

3. ELEMENT SQUARE OF RELATIVE CONTINUUM INTERVAL IN LAGRANGIAN COORDINATES

For example, we shall consider the motion of classic rigid body with the law of motion

$$x^a = \int_0^t v(\tau) d\tau + y^a, \quad x^0 = ct = \xi^{\hat{0}}. \tag{66}$$

Here the IRF time is selected as a time parameter $\xi^{\hat{0}}$. Element of the relative interval can be constructed from metric coefficients (61)

$$\begin{aligned}
 d\tilde{S}^2 &= \frac{1}{\Theta^2} d\xi^{\hat{0}^2} + g_{\mu\nu}^* \frac{\partial \Psi^\mu}{\partial y^{\hat{n}}} \frac{\partial \Psi^\nu}{\partial y^{\hat{k}}} dy^{\hat{n}} dy^{\hat{k}}, \\
 g_{\mu\nu}^* &= g_{\mu\nu} - V_\mu V_\nu.
 \end{aligned} \tag{67}$$

$g_{\mu\nu}^*$ is the projection operator in Minkowski space projecting the tensors on the hypersurface orthogonal to world lines of basis particles.

The relative interval element $d\tilde{S}^2$ differs from the absolute interval element (40) by the normalizing factor before the time coefficient. And, that is more important, that the holonomic element $d\xi^{\hat{0}} = cdt$ is included instead of the anholonomic element $dy^{\hat{0}}$ determined from (41). It is clear that the magnitudes of absolute and relative intervals are not equal. Use of the metric for absolute interval obtained by means of nonholonomic transformations results in zero nonholonomic curvature tensor. Nonholonomic and holonomic curvature

tensors differed from zero are obtained from zero nonholonomic curvature tensor by means of the procedure developed above.

Normalizing factor $1/\Theta^2$ can be calculated in accordance with (57). Use of the law of motion (66) results in the form of the interval element square (66)

$$d\tilde{S}^2 = \frac{1}{V_0^2} dx^{0^2} - (\delta_{nk} + V_n V_k) dy^{\hat{n}} dy^{\hat{k}}. \tag{68}$$

Relation (68) was obtained earlier by V.I. Rodichev [13], in this relation Eulerian coordinates X^k were included instead of Lagrangian coordinates y^k and the motion was not considered as certainly classic rigid.

For particular case when rigid box having at infinity zero velocity falls from infinity at the centrosymmetrical Sun field, the similar formula for the interval (68) is presented in known A. Sommerfeld book [14] with the reference to the unpublished Lents work. Based on this formula Sommerfeld got the interval in the Schwarzschild form using the Newton's law as a first approximation.

Interval (68) in the Rodichev form can be obtained from the interval (67) and for the arbitrary law of continuum motion

$$x^a = \Psi^a(y^{\hat{k}}, x^0), \quad x^0 = ct = \xi^{\hat{0}}, \tag{69}$$

if one introduces the following designation [15]

$$\frac{\partial \Psi^k}{\partial y^{\hat{n}}} dy^{\hat{n}} = dX^k, \tag{70}$$

which means that the element connecting two close Lagrangian particles is considered in Euler coordinates at the fixed instant of time t . Such method is used in the classical mechanics of continua when deriving the deformation tensor in Lagrangian co-moving reference frame (RF).

For arbitrary continuum motion (69) the relative interval element in Lagrangian coordinates has the form

$$d\tilde{S}^2 = \frac{1}{V_0^2} d\xi^{\hat{0}^2} - (\delta_{mn} + V_m V_n) \frac{\partial \Psi^m}{\partial y^{\hat{i}}} \frac{\partial \Psi^n}{\partial y^{\hat{k}}} dy^{\hat{i}} dy^{\hat{k}}. \tag{71}$$

Let us consider some particular RF cases realized by means of the law of motion (69) and metric (71).

3.1. UNIFORMLY ROTATING RF

Unlike the relativistic rigid NRF considered in previous part and realized in the Riemannian space-time we shall follow to the standard transition method [10].

We select the rest-frame in which we introduce cylindrical coordinates r_0, φ_0, z_0, t_0 and move to the rotating RF r, φ, z, t in accordance with formulae:

$r_0 = r, \varphi_0 = \varphi + \Omega t, z_0 = z, t_0 = t,$
 where the rotational speed Ω relatively z axis is considered as constant.

Passing on from Galilean coordinates (71) to cylindrical coordinates we obtain the expression for the relative interval in rotating NRF. The interval element has the form

$$d\tilde{S}^2 = \left(1 - \frac{\Omega^2 r^2}{c^2}\right) c^2 dt^2 - dr^2 - \frac{r^2 d\phi^2}{1 - \frac{\Omega^2 r^2}{c^2}} - dz^2. \quad (72)$$

To compare we present the range of interval in the standard consideration

$$dS^2 = \left(1 - \frac{\Omega^2 r^2}{c^2}\right) c^2 dt^2 - 2\Omega r^2 d\phi dt - dz^2 - r^2 d\phi^2 - dr^2. \quad (73)$$

Both formulas are correct if $r\Omega/c < 1$ and satisfy to the stiffness criterion both classic and Born relativistic one. However there is the significant difference between the metrics: metric (72) is realized in the Riemannian space-time and metrics (73) is realized in the flat Minkowski space. At $t = const$ metric (72) corresponds to the element of the "physical" space interval in the rotating reference frame in accordance with (43). Unlike (73) in (72) g_{0k} components of metric tensor are absent, this means the possibility of watches synchronization along any closed circuit [10].

The connection between the true time τ and the time of Minkowski space t is identical for both metrics

$$d\tau^2 = \left(1 - \frac{\Omega^2 r^2}{c^2}\right) dt^2. \quad (74)$$

Unlike the relativistic rigid NRF both metrics are correct only for finite distances from the rotation axis.

Metrics (72) permits a simple geometrical interpretation.

The relative interval element as well as in IRF in Cartesian coordinates is determined in accordance with Pythagoras theorem for the pseudo-Riemannian space-time: the squared element of the "physical" length is subtracted from the squared proper time (multiplied by the squared light velocity).

3.2. RELATIVISTIC (NONRIGID) UNIFORMLY ACCELERATED NRF

In Minkowski space there is no any law of motion which results in simultaneous fulfillment of two conditions: relativistic rigidity and uniformly acceleration [1-5]. Therefore we consider as the uniformly accelerated RF the motion of the charged dust in the constant electric field resulting in Logunov metric $dS^2 = (dx^0)^2 - (dx^1)^2 - (dx^2)^2 - (dx^3)^2,$ where $x_0 = ct, x^1, x^2, x^3$ are the Cartesian coordinates, and the law of continuum motion for the Logunov metric has the form

$$x^1(y^1, t) = y^1 + (c^2/a_0) \left[\sqrt{1 + a_0^2 t^2 / c^2} - 1 \right],$$

$$x^2 = y^2, x^3 = y^3, x^0 = y^0$$

or

$$x^1(y^1, \tau) = y^1 + c^2/a_0 [\cosh(a_0 \tau / c) - 1],$$

$$x^2 = y^2, x^3 = y^3, t = (c/a) \sinh(a_0 \tau / c),$$

where the IRF time is used as a time parameter, and τ is the proper time

$$dS^2 = \frac{c^2 dt^2}{1 + a_0^2 t^2 / c^2} - 2 \frac{a_0 t dt dy^1}{(1 + a_0^2 t^2 / c^2)^{1/2}} -$$

$$-(dy^1)^2 - (dy^2)^2 - (dy^3)^2,$$

$$dS^2 = c^2 (d\tau)^2 - 2 \sinh(a_0 \tau / c) c d\tau dy^1 -$$

$$-(dy^1)^2 - (dy^2)^2 - (dy^3)^2.$$

Substitution of the law of motion into (71) ($y^{\hat{k}} \rightarrow y^k$) results in the interval element in the form

$$d\tilde{S}^2 = \frac{c^2 dt^2}{1 + a_0^2 t^2 / c^2} - (1 + a_0^2 t^2 / c^2)(dy^1)^2 + (dy^2)^2 + (dy^3)^2. \quad (75)$$

Substitution of the law of motion into (71) (with the substitution $\Theta = 1$, $t \rightarrow \tau$) results in the squared interval in the form

$$d\tilde{S}^2 = c^2 d\tau^2 - \cosh^2\left(\frac{a_0 \tau}{c}\right)(dy^1)^2 + (dy^2)^2 + (dy^3)^2. \quad (76)$$

Formula (75) was obtained by V.I. Rodichev from other considerations [13] but in Euler coordinates (not Lagrange coordinates as in our case). It is clear that (76) can be obtained from (75) by means of the simple time transformation which is determined by the equality $t = (c/a_0)\sinh(a_0\tau/c)$.

The analysis of formulae (75) and (76) and the comparison with the similar Logunov's relations shows that the elements of the relative intervals (as in the rotary motion case) are calculated in accordance with the Pythagoras theorem for the pseudo-Riemann space, when the squared element of the "physical" length is subtracted from the squared proper time (multiplied by the squared light velocity).

The calculation of the relative curvature tensor for metric (76) results in one component differed from zero

$$\hat{R}_{0i,i}^{\hat{0}} = -\frac{a_0^2}{c^4} \cosh\left(\frac{a_0^2 \xi^{\hat{0}}}{c^2}\right). \quad (77)$$

For the scalar curvature we obtain

$$\hat{R} = -2\frac{a_0^2}{c^4}. \quad (77a)$$

In accordance with the standard viewpoint [10] the synchronization of the watches being at the same physical conditions that is at the same distance from the rotation axis is **absent**.

In our consideration *for the relative interval* such "paradox" does not arise.

In considering the rotary motion the watches being at the similar distance from the rotation axis have to show the same proper time. A mathematical transition to the relative interval can be realized by the elementary way: using $dy^{\hat{0}}$ in metric (40) at the fixed value of the Lagrangian particle coordinate $y^{\hat{k}}$ in (41). That results in the interval

$$d\tilde{S}^2 = d\xi^{\hat{0}2} + g_{\mu\nu}^* \frac{\partial \Psi^\mu}{\partial y^{\hat{n}}} \frac{\partial \Psi^\nu}{\partial y^{\hat{k}}} dy^{\hat{n}} dy^{\hat{k}}, \quad g_{\mu\nu}^* = g_{\mu\nu} - V_\mu V_\nu, \quad (78)$$

the length of which in the general case is not equal to the interval length (40).

Thus, from our viewpoint the NRF observer interval (that is the relative interval (78)) is differed from the IRF observer interval using NRF coordinates (40). It follows from the developed mathematical apparatus permitting to select the holonomic curvature tensor from zero anholonomic one, that usual Riemannian-Christoffel tensor calculated from the relative interval metric in the general case is differed from zero.

4. ACCELERATION ADDITION LAW, RELATIVE NRF CURVATURE TENSOR IN MINKOWSKI SPACE

One can ascertain the physical meaning of the relative curvature tensor on the basis of the analysis of a particle motion in an arbitrary NRF force field.

Let the continuum moves in Minkowski space in some force field. The field of 4-velocity of the medium in Euler variables is $V^{\hat{\mu}}$. At the same space in the other force field the particle moves with 4-velocity $U^{\hat{\mu}}$ not coinciding with $V^{\hat{\mu}}$.

The transition to NRF is realized by means of Lamé parameters (2) using the equation of motion

$$h_\alpha^{\hat{\mu}} \frac{dU^\alpha}{d\tilde{S}} = \frac{1}{m_0 c} h_\alpha^{\hat{\mu}} f^\alpha. \quad (79)$$

In formula (79) m_0 is the rest mass of the particle, f^α is the 4-force. From (2)-(6) using the equalities

$$\hat{\nabla}_{\hat{\mu}} h_{\hat{\alpha}}^{\nu} = h_{\hat{\gamma}}^{\nu} T_{\hat{\mu}\hat{\alpha}}^{\hat{\gamma}}, \quad \tilde{\nabla}_{\hat{\mu}} h_{\hat{\alpha}}^{\nu} = 0, \quad (80)$$

after simple transformations we obtain

$$\frac{d\hat{U}^{\hat{\mu}}}{d\tilde{S}} + \left\{ \begin{matrix} \hat{\mu} \\ \hat{\alpha}\hat{\beta} \end{matrix} \right\} \hat{U}^{\hat{\alpha}} \hat{U}^{\hat{\beta}} = \frac{1}{m_0 c} f^{\hat{\mu}} - T_{\hat{\alpha}\hat{\beta}}^{\hat{\mu}} \hat{U}^{\hat{\alpha}} \hat{U}^{\hat{\beta}}. \quad (81)$$

If the particle under consideration belongs to one of the NRF basis particles then $U^\mu = V^\mu$ and it follows from (14) that the second member of equation (81) vanishes. In other words for comoving NRF observers the relative first curvature vectors of basis particle world lines are equal to zero, and the relative space-time curvature is differed from zero. We rewrite equations (81) into components using obvious relation

$$d\tilde{S}^2 = dy^{\hat{0}^2} - dl^2 = \left(1 - \frac{u^2}{c^2}\right) dy^{\hat{0}^2}, \quad (82)$$

where u is the value of the relative particle velocity. Using expressions (14) and designations (38a) we obtain the motion equations relatively NRF in the form convenient for the comparison with the Zel'manov work [8]

$$\frac{dE}{d\tau} + m D_{\hat{i}\hat{k}} u^{\hat{i}} u^{\hat{k}} - m F_{\hat{i}} u^{\hat{i}} = c^2 V_{\mu} f^{\mu} \sqrt{1 - \frac{u^2}{c^2}}, \quad (83)$$

$$\begin{aligned} \frac{dp^{\hat{k}}}{d\tau} + \lambda_{\hat{n}\hat{i}}^{\hat{k}} p^{\hat{n}} u^{\hat{i}} + 2m \left(D_{\hat{i}}^{\hat{k}} + A_{\hat{i}}^{\hat{k}} \right) u^{\hat{i}} - m F^{\hat{k}} &= \\ = c f^{\hat{k}} \sqrt{1 - \frac{u^2}{c^2}}. \end{aligned} \quad (84)$$

The following designations are introduced in formulae (83) and (84):

$$E = \frac{m_0 c^2}{\sqrt{1 - \frac{u^2}{c^2}}}, \quad p^{\hat{i}} = \frac{m_0 u^{\hat{i}}}{\sqrt{1 - \frac{u^2}{c^2}}}, \quad m = \frac{E}{c^2}, \quad d\tau = \frac{dy^{\hat{0}}}{c}, \quad (85)$$

where E is the relative (chronometrically invariant (c.i.) [8]) particle energy, m is the relative (c.i.) mass, and $p^{\hat{i}}$ is the relative (c.i.) pulse. The left-hand members of equalities (83)

and (84) are identical to the left-hand members of equalities in world motion equations [8]. One can easy prove the equality of the right-hand members. Really for the holonomic frames obtained from (1) in the comoving NRF the equality is valid

$$\begin{aligned} V_{\mu} f^{\mu} &= \hat{f}^{\hat{0}} = V_{\hat{0}} f^{\hat{0}} + V_{\hat{k}} f^{\hat{k}} = \\ &= \sqrt{g_{\hat{0}\hat{0}}} f^{\hat{0}} + \frac{g_{\hat{0}\hat{k}}}{\sqrt{g_{\hat{0}\hat{0}}}} f^{\hat{k}} = g_{\hat{0}\hat{\alpha}} f^{\hat{\alpha}} = \frac{f_{\hat{0}}}{\sqrt{g_{\hat{0}\hat{0}}}}, \end{aligned} \quad (86)$$

use of this equality proves the coincidence of the right-hand members of equations (83) and work [8]. The proof for (84) is similar. Thus, in spite of the difference of our transition method to NRF and the T.C.I. method, the motion equations relatively NRF coincide.

One can write equation (82) after the convolution with $h_{\hat{\mu}}^{\alpha}$ in Minkowski space in the form covariant relatively arbitrary holonomic transformations of Eulerian coordinates. Using (14) after simple transformations we obtain

$$h_{\hat{\mu}}^{\alpha} \frac{\hat{D}\hat{U}^{\hat{\mu}}}{d\tilde{S}} \equiv K^{\alpha} = \frac{f^{\alpha}}{m_0 c} - 2g^{\alpha\beta} (U^{\nu} V_{\nu}) U^{\sigma} \nabla_{[\sigma} V_{\beta]}. \quad (87)$$

In relation (87) K^{α} is the relative 4-acceleration of the particle relatively NRF in IRF coordinates, orthogonal to the 4-velocity U_{α} , $f^{\alpha}/(m_0 c)$ is the absolute 4-acceleration of the particle, the last term in (84) contains the reference-frame acceleration and the Coriolis acceleration. Thus, relation (87) is the special relativistic acceleration addition law turning into the classic law in a non-relativistic approximation.

We point out that the relative 4-acceleration appeared as a result of the calculation of the absolute derivative in NRF from the relative 4-velocity of the particle by means of the Christoffel connectivity part (6). Therefore, one can call the curvature tensor (8) $\hat{R}_{\hat{\alpha}\hat{\beta}\hat{\gamma}}^{\hat{\mu}}$ as the relative NRF curvature tensor. Using by the equality

$$\hat{\nabla}_{\hat{\nu}} T_{\hat{\mu}\hat{\alpha}}^{\hat{\gamma}} = \tilde{\nabla}_{\hat{\nu}} T_{\hat{\mu}\hat{\alpha}}^{\hat{\gamma}} - T_{\hat{\nu}\hat{\epsilon}}^{\hat{\gamma}} T_{\hat{\mu}\hat{\alpha}}^{\hat{\epsilon}} + T_{\hat{\nu}\hat{\mu}}^{\hat{\epsilon}} T_{\hat{\epsilon}\hat{\lambda}}^{\hat{\gamma}} + T_{\hat{\nu}\hat{\lambda}}^{\hat{\epsilon}} T_{\hat{\mu}\hat{\epsilon}}^{\hat{\gamma}}, \quad (88)$$

one can rewrite the curvature tensor (8) in the form

$$\hat{R}_{\hat{\nu}\hat{\mu}\hat{\lambda}}^{\hat{\nu}\hat{\gamma}} = -2\hat{\nabla}_{[\hat{\nu}}T_{\hat{\mu}]\hat{\lambda}}^{\hat{\gamma}} - 2T_{[\hat{\nu}|\hat{\lambda}]^{\hat{\gamma}}}T_{\hat{\mu}]\hat{\epsilon}}^{\hat{\gamma}}. \quad (89)$$

Using equality (80) and convolving the curvature tensor (89) by means of Lamé coefficients we obtain the expression for the relative curvature tensor in Minkovsky space

$$h_{\hat{\nu}}^{\sigma}h_{\hat{\alpha}}^{\nu}h_{\hat{\beta}}^{\mu}h_{\hat{\delta}}^{\lambda}\hat{R}_{\hat{\nu}\hat{\mu}\hat{\lambda}}^{\hat{\nu}\hat{\gamma}} = R_{\alpha\beta,\delta}^{\dots\sigma} = -2\partial_{[\alpha}T_{\beta]\delta}^{\sigma} - 2T_{[\alpha|\delta]}^{\epsilon}T_{\beta]\epsilon}^{\sigma}. \quad (90)$$

The $T_{\nu\mu}^{\epsilon}$ tensor in Minkovsky space has the form

$$T_{\nu\mu}^{\epsilon} = F^{\epsilon}V_{\nu}V_{\mu} - V^{\epsilon}(\Omega_{\nu\mu} + F_{\mu}V_{\nu}) + V_{\nu}\Omega_{\mu}^{\epsilon} + V_{\mu}\Omega_{\nu}^{\epsilon}. \quad (91)$$

After transformations one can represent the tensor in the form

$$T_{\nu\mu,\epsilon} = \frac{1}{2}[F_{\nu\mu}V_{\epsilon} + F_{\epsilon\nu}V_{\mu} + F_{\epsilon\mu}V_{\nu}], \quad (92)$$

$$F_{\mu\nu} = 2\nabla_{[\nu}V_{\mu]}.$$

The tensor field of the relative NRF curvature tensor arises in the flat space-time as the result of the division of zero non-holonomic curvature tensor into two nonzero parts. This field is not destroyed by no holonomic transformations both containing the time and not containing the time. We point out that in formula (90) when using the curvilinear coordinates in Minkovsky space the partial derivatives are substituted by the covariant ones.

Although the form of the relative curvature tensor (90) is similar to the Riemann-Christoffel tensor, however the true tensors of the affine connectivity deformation determined in (6) and expressed in the Eulerian coordinates of the Minkovsky space (92) are included in the tensor instead of the connectivity coefficients (not tensors).

For example, we consider the non-relativistic irrotational dust motion in the Newton gravitational field. We save the terms with the multiplier no more then $1/c^2$ in the

relative curvature tensor and in the relative Ricci tensor. In this approximation from (29) and (36) we have

$$\begin{aligned} \tilde{R}_{\hat{a}\hat{b},\hat{c}\hat{q}} &\approx 0, \quad \tilde{R}_{\hat{a}\hat{b},\hat{c}\hat{0}} \approx 0, \quad \tilde{R}_{\hat{0}\hat{b},\hat{c}\hat{0}} \approx -\hat{\nabla}_{(\hat{b}}F_{\hat{c})}, \\ \tilde{R}_{\hat{b}\hat{c}} &\approx -\hat{\nabla}_{(\hat{b}}F_{\hat{c})}, \quad \tilde{R}_{\hat{b}\hat{0}} \approx 0, \quad \tilde{R}_{\hat{0}\hat{0}} \approx -\hat{\nabla}_{\hat{n}}F^{\hat{n}}. \end{aligned} \quad (93)$$

As $F^{\hat{b}}$ are the space components of the 4-acceleration, then in the non-relativistic case when motion in the Newton field $F^{\hat{b}} = a^{\hat{b}}/c^2$, where $a^{\hat{b}}$ is the usual three-dimensional acceleration. From the Poisson equation we obtain

$$-\hat{\nabla}_{\hat{n}}a^{\hat{n}} = 4\pi k\rho, \quad (94)$$

where k is the gravitational constant, ρ is the medium density. As a result we have

$$\tilde{R}_{\hat{0}\hat{0}} = \frac{4\pi k\rho}{c^2}, \quad \tilde{R}_{\hat{b}\hat{0}} \approx 0, \quad \tilde{R}_{\hat{b}\hat{c}} = -\frac{1}{c^2}\hat{\nabla}_{(\hat{b}}F_{\hat{c})}. \quad (95)$$

The first and the second equalities in expression (95) coincide with the corresponding Einstein equations in the synchronous reference frame, the last equality does not coincide.

Let us consider the simplest properties of the relative curvature tensor in Minkovsky space. It follows from expression (92) for the tensor of the affine connectivity deformation $T_{\nu\mu}^{\epsilon}$ in Minkovsky space that for the irrotational motions it has the form

$$T_{\nu\mu}^{\epsilon} = F^{\epsilon}V_{\nu}V_{\mu} - V^{\epsilon}F_{\mu}V_{\nu} = g^{\epsilon\sigma}V_{\nu}\left(\frac{\partial V_{\sigma}}{\partial x^{\mu}} - \frac{\partial V_{\mu}}{\partial x^{\sigma}}\right). \quad (96)$$

If the irrotational motion is rigid, this results in zero relative curvature tensor. Thus, the translation motion of the relativistic rigid body does not result in the appearance of the relative space-time curvature.

For arbitrary motions the relative Ricci tensor can be represented in the from

$$R^{\beta\gamma} = -\frac{\partial T^{\beta\gamma\alpha}}{\partial x^{\alpha}} - \frac{\partial F^{\gamma}}{\partial x_{\beta}} + \Omega_{\alpha\epsilon}\Omega^{\alpha\epsilon}V^{\beta}V^{\gamma} - \Omega^{\gamma\epsilon}F_{\epsilon}V^{\beta}. \quad (97)$$

Scalar relative curvature R is calculated in accordance with the formula

$$R = -2 \frac{\partial F^\gamma}{\partial x^\gamma} + \Omega_{\alpha\epsilon} \Omega^{\alpha\epsilon}. \tag{98}$$

The relative Einstein tensor $G^{\beta\gamma}$ is determined by the expression

$$G^{\beta\gamma} = -\frac{\partial T^{\beta\gamma\alpha}}{\partial x^\alpha} - \frac{\partial F^\gamma}{\partial x_\beta} + \Omega_{\alpha\epsilon} \Omega^{\alpha\epsilon} V^\beta V^\gamma - \Omega^{\gamma\epsilon} F_\epsilon V^\beta + g^{\beta\gamma} \frac{\partial F^\alpha}{\partial x^\alpha} - \frac{1}{2} g^{\beta\gamma} \Omega_{\alpha\epsilon} \Omega^{\alpha\epsilon}. \tag{99}$$

For irrotational motions the relative Ricci tensors and the Einstein tensors can be represented in the form

$$R^{\beta\gamma} = \frac{\partial(F^{\gamma\alpha} V^\beta)}{\partial x^\alpha} - \frac{\partial F^\gamma}{\partial x_\beta}, \tag{100}$$

$$G^{\beta\gamma} = \frac{\partial(F^{\gamma\alpha} V^\beta)}{\partial x^\alpha} - \frac{\partial F^\gamma}{\partial x_\beta} + g^{\beta\gamma} \frac{\partial F^\alpha}{\partial x^\alpha} = 2 \frac{\partial}{\partial x^\alpha} (g^{*\beta[\gamma} F^{\alpha]}), \tag{101}$$

where $g^{*\beta\gamma}$ is the projection operator introduced in (40). One can see from (101) that the relative Einstein tensor for irrotational motions identically satisfies to the conservation law

$$\frac{\partial G^{\beta\gamma}}{\partial x^\gamma} \equiv 0, \tag{102}$$

however it is not a symmetrical one.

5. RELATIVE CONTINUUM CURVATURE TENSOR IN NEWTON MECHANICS

Let us investigate in the Newton approximation the space-time metric for observers moving together with the medium neglecting by the value v^2/c^2 as compared with the unit. In this approximation metrics (40) reduces to the form

$$dS^2 = c^2 dt^2 - \delta_{mn} \frac{\partial \Psi^m}{\partial y^k} \frac{\partial \Psi^n}{\partial y^i} \partial y^k \partial y^i. \tag{103}$$

In metric (103) the Cartesian coordinates are selected as the Euler IRF coordinates, where $g_{mn} = -\delta_{mn}$, t is the Newton absolute time. It should be pointed out that *metrics (103) in the general case*

is the Riemannian one with the flat spatial section. At first this result is improbable, however metric (103) permits simple geometrical and physical interpretation.

For example, let us consider the nonrigid rod, the elements of the rod move along its axis with different velocities. A particle moves near the rod and parallel to it with the velocity exceeding the velocities of the rod particles. We agree that the observers at the rod use the IRF watch of Minkovsky space. Let when the particle caught up with the back end of the rod the watch reading is t_1 , and at the over-taking point the watch showed t_2 . The passing time is $(t_2 - t_1)$. It is clear that one can calculate *the relative length of the particle world line* when the rod passing in accordance with Pythagoras theorem. *The relative length of the particle world line* when the rod has infinitesimal dimensions is determined by formula (103). Interval element (103) is obtained from the pseudo-Euclidian interval by means of the motion law $x^n = \Psi^n(y^k, t)$, and the differential with respect to x^n is calculated at the fixed t value, that is it is not a complete. Therefore, the squared interval element obtained by the subtraction of the squared spatial element specified in the Lagrange comoving NRF from the squared time element in the general case results in non-Euclidian space-time with the flat spatial section.

Usually when transiting from IRF to NRF one considers *the element of the absolute length of the particle world line.* The interval element is obtained from the pseudo-Euclidian interval by means of the motion law $x^n = \Psi^n(y^k, t)$, and the differential with respect to x^n is complete. Therefore, the squared element (as opposite to (103)) contains the terms depending on the absolute particle velocity, g_{00} component changes and g_{0k} components of the metric tensor differed from zero appear. However the space-time remains flat. Obviously, *the absolute*

length of the world line of the considered particle is not equal to the relative length of the world line of the particle.

The spatial metric in the Lagrange comoving NRF in accordance with (103) has the form

$$\hat{\gamma}_{\hat{k}\hat{l}} = \delta_{mn} \frac{\partial \Psi^m}{\partial y^{\hat{k}}} \frac{\partial \Psi^n}{\partial y^{\hat{l}}}. \quad (104)$$

As is known from the continuum mechanics [16]

$$\frac{d\hat{\gamma}_{\hat{k}\hat{l}}}{dt} = 2\hat{\sigma}_{\hat{k}\hat{l}}, \quad (105)$$

where $\hat{\sigma}_{\hat{k}\hat{l}}$ is the tensor of deformation rates in the comoving RF (reference system). As when moving Lagrange coordinates $y^{\hat{k}}$ of each particle remain constant, then $dy^{\hat{k}}/dt = 0$, and therefore

$$\frac{d\hat{\gamma}_{\hat{k}\hat{l}}}{dt} = \frac{\partial \hat{\gamma}_{\hat{k}\hat{l}}}{\partial t} + \frac{\partial \hat{\gamma}_{\hat{k}\hat{l}}}{\partial y^{\hat{m}}} \frac{dy^{\hat{m}}}{dt} = \frac{\partial \hat{\gamma}_{\hat{k}\hat{l}}}{\partial t} = 2\hat{\sigma}_{\hat{k}\hat{l}}. \quad (106)$$

Let us consider the motion of the airfree gas in the Newton gravitational field using the motion equation in the Euler form and the continuity equation

$$\frac{\partial v_a}{\partial t} + v^k \frac{\partial v_a}{\partial x^k} = g_a, \quad \frac{\partial \rho}{\partial t} + \frac{\partial}{\partial x^a} (\rho v^a) = 0. \quad (107)$$

Differentiating equation (107) with respect to x^b we have

$$\frac{\partial}{\partial t} (\sigma_{ab} + \omega_{ab}) + (\sigma_{kb} + \omega_{kb}) (\sigma_{ak} + \omega_{ak}) +$$

$$+ v^k \frac{\partial}{\partial x^k} (\sigma_{ab} + \omega_{ab}) = \frac{\partial g_a}{\partial x^b} \quad (108)$$

or

$$\frac{d}{dt} (\sigma_{ab} + \omega_{ab}) + (\sigma_{kb} + \omega_{kb}) (\sigma_{ak} + \omega_{ak}) = \frac{\partial g_a}{\partial x^b}, \quad (109)$$

where

$$\sigma_{ab} = \frac{1}{2} \left(\frac{\partial v_a}{\partial x^b} + \frac{\partial v_b}{\partial x^a} \right), \quad \omega_{ab} = \frac{1}{2} \left(\frac{\partial v_a}{\partial x^b} - \frac{\partial v_b}{\partial x^a} \right). \quad (110)$$

In (110) σ_{ab} , ω_{ab} are the deformation and the rotational velocity tensors in the non-relativistic mechanics in the Euler variables.

Convolving (108) on a, b we obtain in the Lagrangian coordinates

$$\begin{aligned} \frac{\partial}{\partial t} \hat{\sigma}_{\hat{a}}^{\hat{a}} + \hat{\sigma}_{\hat{b}}^{\hat{k}} \hat{\sigma}_{\hat{k}}^{\hat{b}} &= \frac{\partial g_a}{\partial x^a}, \quad \sigma_{ab} = \frac{\partial v_a}{\partial x^b} = \frac{\partial v_b}{\partial x^a}, \\ \frac{\partial \sigma_a^b}{\partial x^b} &= \frac{\partial \sigma_b^a}{\partial x^a}. \end{aligned} \quad (111)$$

The last relation in the Lagrangian coordinates is reduced to the form

$$\hat{\nabla}_{\hat{b}} \hat{\sigma}_{\hat{a}}^{\hat{b}} - \hat{\nabla}_{\hat{a}} \hat{\sigma}_{\hat{b}}^{\hat{b}} = 0, \quad (112)$$

where the covariant derivatives are calculated in accordance with metric (104). To calculate the Ricci tensor we use metrics (103) and the result [10] for the synchronous frame of reference with the flat spatial metric

$$\hat{R}_{\hat{0}\hat{0}} = -\frac{1}{c^2} \left(\frac{\partial}{\partial t} \hat{\sigma}_{\hat{a}}^{\hat{a}} + \hat{\sigma}_{\hat{b}}^{\hat{k}} \hat{\sigma}_{\hat{k}}^{\hat{b}} \right), \quad (113)$$

$$\hat{R}_{\hat{0}\hat{a}} = \frac{1}{c} \left(\hat{\nabla}_{\hat{b}} \hat{\sigma}_{\hat{a}}^{\hat{b}} - \hat{\nabla}_{\hat{a}} \hat{\sigma}_{\hat{b}}^{\hat{b}} \right), \quad (114)$$

$$\hat{R}_{\hat{a}\hat{b}} = \frac{1}{c^2} \left(\frac{\partial}{\partial t} (\hat{\sigma}_{\hat{a}\hat{b}}) + \hat{\sigma}_{\hat{a}\hat{b}} \hat{\sigma}_{\hat{k}}^{\hat{k}} - 2\hat{\sigma}_{\hat{a}}^{\hat{k}} \hat{\sigma}_{\hat{b}\hat{k}} \right). \quad (115)$$

One can show that when the rotations are absent the equality is valid

$$\frac{\partial}{\partial t} \hat{\sigma}_{\hat{a}\hat{b}} = \left(\frac{d\sigma_{kl}}{dt} + 2\sigma_{ml} \sigma_{mk} \right) \frac{\partial \Psi^k}{\partial y^{\hat{a}}} \frac{\partial \Psi^l}{\partial y^{\hat{b}}}, \quad (116)$$

using the equality for expression (115) we have

$$\hat{R}_{\hat{a}\hat{b}} = \frac{1}{c^2} \left(\frac{d\sigma_{kl}}{dt} + \sigma_{kl} \sigma_m^m \right) \frac{\partial \Psi^k}{\partial y^{\hat{a}}} \frac{\partial \Psi^l}{\partial y^{\hat{b}}}. \quad (117)$$

Taking into account (109) when the rotations are absent we find

$$\hat{R}_{\hat{a}\hat{b}} = \frac{1}{c^2} \left(\frac{\partial g_k}{\partial x^l} + \sigma_{kl} \sigma_m^m - \sigma_{km} \sigma_l^m \right) \frac{\partial \Psi^k}{\partial y^{\hat{a}}} \frac{\partial \Psi^l}{\partial y^{\hat{b}}}. \quad (118)$$

The medium moving in the eigen gravitational field has $g_a = \partial \phi / \partial x^a$, where ϕ is the potential of the gravitational field satisfying to the Poisson equation. From relations (111) and the Poisson equation for (113) we find

$$\hat{R}_{\hat{0}\hat{0}} = \frac{4\pi k \rho}{c^2}. \quad (119)$$

Relation (114) taking into account (112) forms

$$\hat{R}_{\hat{0}\hat{a}} = 0. \quad (120)$$

We present expression (118) in aggregate with the Poisson equation in the form convenient for further investigations

$$\hat{R}_{\hat{a}\hat{b}} = \frac{4\pi\rho k}{c^2} \hat{\gamma}_{\hat{a}\hat{b}} + \hat{F}_{\hat{a}\hat{b}},$$

$$\hat{F}_{\hat{a}\hat{b}} = \left(\frac{\partial g^m}{\partial x^m} \delta_{kl} + \frac{\partial g_k}{\partial x^l} + \sigma_{kl} \sigma_m^m - \sigma_{km} \sigma_l^m \right) \frac{\partial \Psi^k}{\partial y^{\hat{a}}} \frac{\partial \Psi^l}{\partial y^{\hat{b}}}. \quad (121)$$

Relations (119)-(121) provided that in the last expression $\hat{F}_{\hat{a}\hat{b}} = 0$ are the Einstein equations written in the synchronous frame of reference for the dust-like matter [10]. Obviously, that in the general case $\hat{F}_{\hat{a}\hat{b}} \neq 0$, as at the same force field the congruencies of the world lines of the medium particles have a greater arbitrariness.

Let us ascertain at what particular conditions the NRF geometry determined with the laws of the Newton mechanics and the geometry of the synchronous frame of reference for the dust-like matter determined with the Einstein equations coincide. It follows from metric (104) that the sought for solutions of the Einstein equation in the case of flat spatial sections are valid. And the coincidence of the Einstein equation solutions with the solutions of the Newton mechanics is possible if one imposes the constrain on the congruency of the world lines of the basis particles

$$\hat{F}_{\hat{a}\hat{b}} = 0. \quad (122)$$

Let us investigate the spherical-symmetrical continuum motions with the following velocity field in Euler variables in Cartesian coordinates

$$v_a = v(r, t) n_a, \quad n_a = \frac{x_a}{r}, \quad n_a n_a = 1. \quad (123)$$

Using Euler equations (107) and symmetry conditions (123) we obtain the expression for system (122)

$$\frac{1}{r} \frac{\partial v}{\partial t} = \Delta \phi, \quad \frac{1}{r} \frac{\partial v}{\partial t} + \frac{v^2}{r^2} + \frac{2}{r} \frac{\partial \phi}{\partial r} = \Delta \phi. \quad (124)$$

Let us consider some particular cases of the system solution:

1. For the radial motion of the airfree medium in the Newton central symmetrical gravitational field created by the massive solid with the mass

center located at the origin of coordinates we have

$$\Delta \phi = 0, \quad \phi = -\frac{kM_0}{r}, \quad v^2 = 2kM_0 \left(\frac{1}{r} - \frac{1}{r_0} \right) + v_0^2, \quad (125)$$

where M_0 is the mass of the solid created the field, v_0 is the velocity at $r = r_0$. From the compatibility of expressions (124) and (125) we obtain

$$\frac{\partial v}{\partial t} = 0, \quad v^2 = 2kM_0 \frac{1}{r}. \quad (126)$$

Solution (126) is the particular case of (125) provided the medium at the infinity is at rest. Integrating (126,) we obtain

$$r = \pm \left(\frac{3c}{2} \right)^{2/3} F^{1/3} (t_0 - t)^{2/3}, \quad F \equiv \frac{2KM_0}{c^2} = r_g, \quad (127)$$

where r_g is the gravitational radius. We point out that in the latter relation the light velocity c is artificially introduced for the convenience of the comparison with other results, and as a result, it is cancelled in this formula as it should be when integrating the motion equations in the non-relativistic mechanics. Selection of the sign depends on the character of the particle motion. When moving on the radius to the center the sign "plus" is selected, and the sign "minus" is selected when extension from the center. Constant t_0 is selected from the demand that at $t = 0$ it should be $r = r_0$, where r_0 is the Lagrange coordinate. Obviously when falling the particles on the center the current radius of the Lagrange particle $r(r_0, t)$ is decreased, therefore $t < t_0$.

The metrics (103) in the spherical coordinate system has the form

$$dS^2 = c^2 dt^2 - \left(\frac{\partial r}{\partial r_0} \right)^2 dr_0^2 - r^2 (d\theta^2 + \sin^2 \theta d\phi^2). \quad (128)$$

Using the law of motion (127) and considering that

$$R \equiv \frac{2}{3} \frac{r_0^{3/2}}{r_g^{1/2}}, \quad (129)$$

we have the expression for the interval element

$$dS^2 = c^2 dt^2 - \frac{dR^2}{\left[\frac{3}{2r_g}(R-ct) \right]^{2/3}} - \left[\frac{3}{2}(R-ct) \right]^{4/3} r_g^{2/3} (d\theta^2 + \sin^2 \theta d\varphi^2), \quad (130)$$

which exactly coincides with the known Lemaître metric in GR [10]. For our case the interval element of the Lemaître metrics means the squared relative length of the test particle world line moving relatively free falling on the radius to the center of non-interacting with each other particles in the Newton central symmetrical gravitational field. The falling particles having zero velocity at the infinity form the NRF basis. The character of the forces acting on the test particle does not matter.

Although metric (130) is identical to the corresponding GR metric, however in our case the coordinates and the time determining the metric have a clear metric sense that is absent in GR in principle. For example, the fall time T of the basis particle from the initial radius value r_1 to the current value $r(r_1, T)$ is the finite value and it is determined by formula

$$T = \frac{2}{3} \left[\frac{r_1}{c} \left(\frac{r_1}{r_g} \right)^{1/2} - \frac{r}{c} \left(\frac{r}{r_g} \right)^{1/2} \right], \quad (131)$$

which corresponds to the GR formula when the particle proper time is used as the time [17]. In our case the Newton time t plays the role of the proper time.

2. Following to [10, 17] we consider the Newton uniform isotropic cosmological model, for which we have

$$v(r, t) = H(t)r. \quad (132)$$

Taking into account Euler equations, we write system (124) in the form

$$\frac{1}{r} \frac{\partial v}{\partial t} = -4\pi k \rho, \quad \frac{3}{r} \frac{\partial v}{\partial t} + \frac{v^2}{r^2} + \frac{2v}{r} \frac{\partial v}{\partial r} = -4\pi k \rho. \quad (133)$$

From equations (132), (133) we find

$$\frac{\partial H}{\partial t} = -4\pi k \rho, \quad \frac{\partial H}{\partial t} + H^2 = -\frac{4}{3} \pi k \rho. \quad (134)$$

Whence

$$H^2 = \frac{8}{3} \pi k \rho, \quad (135)$$

that corresponds to the extension case when the density is equal to the critical one. Since the law of the Universe evolution in the Newton approximation was derived in [17] for the arbitrary density, then using the results [17] we find the law of extension for our case

$$r = r_0 \left(\frac{t - t_\infty}{t_0 - t_\infty} \right)^{2/3}, \quad (136)$$

where $(t_0 - t_\infty)$ is the "age" of the homogeneous model of the Universe. Substitution of (136) into (128) results in the expression for the squared interval

$$dS^2 = c^2 dt^2 - \left(\frac{t - t_\infty}{t_0 - t_\infty} \right)^{4/3} \left[dr_0^2 - r_0^2 (d\theta^2 + \sin^2 \theta d\varphi^2) \right], \quad (137)$$

which corresponds to the model with the flat (Euclidean) GR space [18-25].

6. CONCLUSION

The strangest result obtained in this work is that the exact solutions of the Einstein equations are contained as the particular cases of the non-relativistic Newton mechanics but not vice-versa.

REFERENCES

1. Podosenov SA. *Geometricheskie svoystva neinertial'nykh sistem otsbeta v rehyativistskoy mekhanike. V kn.: Diskussionnye voprosy teorii otnositel'nosti i gravitatsii.* [Geometrical properties of noninertial reference frames in relativistic mechanics. In: Debatable problems of theory of relativity and gravitation]. Moscow, Nauka Publ., 1982, p. 95-103.
2. Podosenov SA. *Prostranstvo, vremya i klassicheskie polya svyazannykh struktur* [Space, time and classical fields of bound

- structures]. Moscow, Sputnik+ Publ., 2000, 445 p.
3. Podosenov SA, Potapov AA, Sokolov AA. *Impul'snaya elektrodinamika shirokopolosnykh radiosistem i polya svyazannykh struktur* [Pulse electrodynamics of wideband radio systems and fields of bound structures]. Edited by AA. Potapov. Moscow, Radiotekhnika Publ., 2003, 720 p.
 4. Podosenov SA. *Novy metod rascheta polya v prostranstve-vremeni svyazannykh struktur* [New method of field calculation in space-time of bound structures]. Monograph. LAP LAMBERT Academic Publishing, 2011.
 5. Podosenov SA, Potapov AA, Foukzon J, Men'kova ER. *Negolonomnye, fraktal'nye i svyazannye struktury v rehyativistskikh sploshnykh sredakh, elektrodinamike, kvantovoy mekhanike i kosmologii. V 3-eh tt. Pod red. d.f.-m.n., prof. AA Potapova. T.1: Teoriya impul'snogo izlucheniya i vzaimodeystvie polya s golonomnymi i fraktal'nymi ob'ektami* [Nonholonomic, Fractal and Bound Structures in Relativistic Continua, Electrodynamics, Quantum Mechanics and Cosmology. In three books. Book 2. Force Fields in Bound and Nonholonomic Structures]. Moscow, LENAND URSS, 2015, 432 p.
 6. Podosenov SA. *Struktura tenzora krivizny NSO v STO. V kn.: Teoriya odnositel'nosti i gravitatsiya* [Structure of NRF curvature tensor in SRT. In: Theory of relativity and gravitation]. Moscow, Nauka Publ., 1976, p. 107-114.
 7. Schouten Jan Arnoldus. *Tensor Analysis for Physicists*, 2d edn., New York: Dover Publications, 1989.
 8. Zel'manov AL. *Khronometricheskie invarianty i soputstvuyushchie koordinaty v obshchey teorii odnositel'nosti* [Chronometric invariants and comoving coordinates in general relativity theory]. DAN SSSR, 1956, 107(6):815-818 (in Russ.).
 9. Podosenov SA. *Diss. na soiskanie uch. step. kand. fiz.-mat. nauk. Rehyativistskaya mekhanika deformiruemoy sredy v tetradnoy formulirovke* [Thesis Ph. D. Phys.-math. Relativistic deformable medium mechanics in tetrad formulation]. Moscow, UDN Publ., 1972.
 10. Landau LD, Lifshitz EM. *The Classical Theory of Fields*, 4th ed. Butterworth-Heinemann, 1975, 429 p
 11. Rashevsky PK. *Rimanova geometriya i tenzornyy analiz* [Riemann geometry and tensor analysis]. Moscow, Nauka Publ., 1967.
 12. Dehnen H. *Über allgemein-relativistische Dynamik. Wissensch. Zeitschr. der Friedrich-Schiller Universität, Jena, Math.-Naturw. Reihe. H. 1. Jahrg., 1966, 15:15-23.*
 13. Rodichev VI. *Teoriya tyagoteniya v ortogonal'nom repere* [Gravitational theory in orthogonal frame]. Moscow, Nauka Publ., 1974.
 14. Sommerfeld A. *Electrodynamik. Vorles. üb. Theor. Phys., Band 3, Geest&Portig K.-G. Verlag, Leipzig, 1949.*
 15. Podosenov SA. *Geometricheskie svoystva soputstvuyushchikh sistem otscheta v spetsial'noy teorii odnositel'nosti. V kn.: Teoriya odnositel'nosti i gevitatsiya* [Geometrical properties of comoving reference frames in special theory of relativity. In book: Theory of relativity and gravitation]. Moscow, Nauka Publ., 1976:100-106.
 16. Sedov LI. *A course in continuum mechanics. Volumes I-IV.* Wolters-Noordhoff Publishing, Netherlands, 1971.
 17. Zel'dovich YaB, Novikov ID. *Rehyativistskaya astrofizika* [Relativistic astrophysics]. Moscow, Nauka Publ., 1967.
 18. Podosenov SA, Potapov AA, Foukzon J. *Electrodynamics of a Continuous Medium in a System with Specified Structure. Physics of Wave Phenomena, 2012, 20(2):143-157.*

19. Podosenov SA, Foukzon J, Potapov AA. A Study of the Motion of a Relativistic Continuous Medium. *Gravitation and Cosmology*, 2010, 16(4):307.
20. Foukzon J, Podosenov SA, Potapov AA. Relativistic length expansion in general accelerated system revisited. <http://arxiv.org/pdf/0910.2298v1>.
21. Podosenov SA, Potapov AA, Foukzon J, Men'kova ER. Geometry of Noninertial Bases in Relativistic Mechanics Continua and Bell's Problem Solution. *International Journal of Recent Advances in Physics (IJRAP)*. Wireilla Scientific Publications, 2014, 3(1):23-37. <http://wireilla.com/physics/ijrap/current2014.html>.
22. Podosenov SA, Foukzon J, Potapov AA, Men'kova ER. About Nonlinear Classic Field Theory of Connected Charges. *International Journal of Recent Advances in Physics (IJRAP)*. Wireilla Scientific Publications, 2014, 3(2):1-20.
23. Podosenov SA, Foukzon J, Potapov AA, Men'kova ER. About Modelling of the Gravitational Fields. *International Journal of Recent Advances in Physics (IJRAP)*. Wireilla Scientific Publications, 2015, 4(1):1-19.
24. Podosenov SA, Foukzon J, Potapov AA, Men'kova ER. Classical and Quasi-classical Consideration of Charged Particles in Coulomb Field of Bound Charges. *International Journal of Recent Advances in Physics (IJRAP)*. Wireilla Scientific Publications, 2015, 4(1):67-89.
25. Podosenov S.A. Uravneniya struktury v ralyativistskoy mekhanike sploshnykh sred i reshenie paradoksa Bella [Structure equations in relativistic mechanics of continuum and Bell's paradox solution]. *Sovremennye naukoemkie tekhnologii*. 2014, 3:132-138 (in Russ.).

PRINTER TECHNOLOGIES IN ELECTRONICS. MATERIALS AND DEVICES FOR PRINTING – FIRST RUSSIAN SEMINAR (Moscow, December 15, 2017)

Denis Yu. Kornilov, Sergey V. Tkachev, Evgeny V. Zaytsev, Vitaly P. Kim, Alexey E. Kushnir

VNIIalmaz, <http://www.vniialmaz.ru>, LLC AkKoLab, <http://www.akkolab.ru>
 Moscow 129110, Russian Federation

kornilovdenis@rambler.ru, tkachev_svmsu@mail.ru, gliese3@gmail.com, vp.kim@physics.msu.ru,
kushnir.a.e@gmail.com

Abstract. The review of the reports of the first Russian seminar on problems of printer technologies in electronics and other fields of technology, as well as on materials and devices for printing, is presented. The seminar was held in Moscow by the company "AkKo Lab" LLC in the All-Russian Research Institute of Natural, Synthetic Diamonds and Tools (VNIIAlmaz) on December 15, 2017, under the supervision of Dr Sci Chem, prof. Sergey P. Gubin. 10 reports presented by the seminar participants from Moscow, Zelenograd, Novosibirsk, Tomsk, Saransk and Dormagen (Germany, Nordrhein-Westfalen) were heard and discussed. The reports were distinguished by high level, acute relevance and variety of staging decisions. The work of the seminar is planned to continue.

Keywords: nanoinks based on metal nanoparticles, coordination compounds of metals, carbon nanotubes, graphene and fluorografen, ceramics, inkjet, aerosol and roll printing, microplotter printing, printer electronics, sensors

UDC 004.356.2, 338.27:004

Bibliography – 3 references

Received 16.12.2017

RENSIT, 2017, 9(2):181-204

DOI: 10.17725/rensit.2017.09.181

CONTENTS

1. INTRODUCTION (181)
2. WELCOME SPEECH BY S.P. GUBINA (182)
3. SILVER, GOLD AND PLATINUM NANO-INK. PRODUCTION AND APPLICATION (183)
4. SUCCESSES AND PROBLEMS IN THE PRODUCTION OF R2R LARGE-SCALE PRINTED ELECTRONICS (185)
5. CREATION OF A CLUSTER OF PRINTED ELECTRONICS BASED ON THE CENTER FOR NANOTECHNOLOGIES AND NANOMATERIALS OF THE REPUBLIC OF MORDOVIA (186)
6. MICROPLOTTER PRINT OF ELECTRODES FOR ULTRATHIN ORGANIC FIELD EFFECT TRANSISTORS (188)
7. FUNCTIONAL INKS BASED ON METAL COORDINATION COMPOUNDS FOR THE CREATION OF THIN-FILM OXIDE NANOSTRUCTURES USING PRINTED TECHNOLOGIES (190)
8. AEROSOL CVD SYNTHESIS OF SINGLE-LAYER CARBON NANOTUBES FOR FLEXIBLE ELECTRONICS (193)
9. PRINTER TECHNOLOGY IN ELECTRONICS (196)

10. 2D PRINTING OF TEST HETEROSTRUCTURES WITH MATERIALS BASED ON GRAPHENE (196)
 11. CERAMIC "INKS" OF LOW-TEMPERATURE CURING BASED ON INORGANIC MATERIALS (199)
 12. ADDITIVE TECHNOLOGIES FOR GAS SENSORS (200)
 13. CONCLUSION (204)
- REFERENCES (204)

1. INTRODUCTION

The first Russian seminar on printer technologies in electronics, entitled "Printer technologies in electronics and other fields of technology: Materials and devices for printing" was conceived and initiated by the famous Russian expert on nanochemistry – Professor Sergey P. Gubin, Doctor of Chemistry, laureate of the State Prize of the USSR, Honored Scientist of Russia, Head of the Laboratory of Chemistry of Nanomaterials of the Kurnakov Institute of General and Inorganic Chemistry of Academy of Sciences of Russia.

Sergey P. Gubin for more than 7 years is the scientific leader of the scientific and production company LLC AkKo Lab, specializing in the development and manufacture of unique innovative materials and energy storage devices based on them – innovative batteries, supercapacitors, ionistors, solar cells, microelectronic devices by inkjet printing with the use of graphene and functional nanoparticles, etc. Years of work in this field in cooperation with many groups of specialists from Russia and abroad caused the demand. The possibility of carrying out this work was provided by the VNIImaz administration, bearing in mind the 6-year work of the seminar in its graphene conference hall, Moscow, and then the Russian one with international participation [1], whose work was completed in the spring this year.

Representatives of commercial companies, research institutes of the Russian Academy of Sciences and other departments, universities, state funds of Russia and foreign research and commercial centers take part in this seminar, more practical than the seminar "Graphene – molecule and 2D crystal". Organizational fee is not provided. Within the framework of the seminar it is planned to hold presentations of participants' works and organize roundtables to discuss various aspects of the current state and future prospects of printer technologies in Russia. The organizers intend to create the conditions necessary for building business contacts for all participants.

Information about the seminar is posted on the website of AkKo Lab LLC <http://www.akkolab.ru>, and also together with the abstracts of papers and articles on the materials of the seminar in the Russian bilingual peer-reviewed journal "Radioelektronika. Nanosistemy, Informatsionnye Tekhnologii (RENSIT)", which is included in the international abstract databases SCOPUS, EBSCO and Ulrich's Periodicals Directory, DB RINC, RUNEB, RJ and DB VINITI RAS.

More than 40 specialists from Moscow and Novosibirsk, Tomsk and Saransk, Zelenograd and Dormagen (Germany, North Rhine-Westphalia) took part in the first 7-hour (with a break) meeting of the seminar. Materials received in France and Finland were presented. After the introductory speech of the general director of LLC AkKo Lab, Mark M. Geller, and the welcome speech of the scientific leader of the company Sergey P. Gubin, 10 reports, including the poster materials of AkKo Lab LLC, were heard and actively discussed. The entire course of work was covered by video shooting by the employees of LLC "AkKo Lab" with the posting of materials on the site <http://www.rensit.ru>.

2. WELCOME SPEECH. Sergey P. Gubin, Dr Sci Chem, Kurnakov IGIC of RAS, Sci Head of LLC "AkKo Lab", Moscow

I will be short enough to go directly to the work program. All, apparently, already know and feel that to replace the classical electronics comes post-silicon electronics, soft electronics, electronics on soft carriers, on paper, leather, including, and on human skin, on polymers, on flexible systems of very different origin, on fibers, etc. etc. And all this is based and has arisen not from scratch. The fact is that many researchers for 20 years, or even more, and we, including, engaged in nanoparticles - the basis of nanotechnology, and for the first time on the basis of nanoparticles we created ink, the so-called silver ink 6 years ago. For the first time, the line on the substrate was printed with these inks, heated to a low temperature, and a conductive strip on a polymer base was obtained. It was a long time ago, and now this area, as you all know, is developing very rapidly. And of course the future behind this field of technology, electronics and related fields.

Sometimes they say: Sergei Pavlovich (when I speak in some classrooms), well, you, seriously, what are you saying? This, of course, is more of a mind game, it's more for such scientific interest. Well, who can replace classical electronics

on silicon and adjacent substrates, in which hundreds of billions of dollars are invested all over the world, which has been developing over the past 50 years, where much has been done, etc., etc., and etc. It's impossible.

In such cases, I usually do not argue. I propose to open the Internet and go to the transport museum, which is in so many cities around the world. In the transport museum you will see on the screen a magnificent photo of one of the last marks of the locomotive. The people sitting in the hall are mostly young people. But there are those who saw these giants in action. I traveled for the first time to Leningrad in the year 1955 on the "Red Arrow" and this train carried locomotive. At that time locomotives were the basis of the movement. It was invested so much efforts, in the world there were dozens of factories. In the year 1955, about 10 thousand locomotives were produced all over the world. And when next to them appeared the first two-carriages electric train Moscow-Mytishchi, gray carriages, some wire up there stretches, it looked very frivolous at the time. Highly. It was hard to believe that the prospect was behind these carriages. Well, now we know - these locomotives are in museums, and where are the electric trains? They speed almost 500 km per hour in some countries moving in all directions.

The same will be in the area in which we are now working. Undoubtedly, the prospect here is quite obvious, and progress and achievements in this area are inevitable, and we are doing right that all forces are spending their energy on the development of this direction in a variety of ways and in various applications. And in order for this matter to become more intensive, we try to connect it with those who are engaged in science. And here, at the first seminar on this topic, there are representatives of scientific institutions (I myself am also at the main work at the Institute of General and Inorganic Chemistry of the Russian Academy of Sciences) and representatives of different kinds of structures and organizations that work directly with materials on this basis.

There are many problems here and today we will begin this work to unite our efforts, to identify those interesting moments that are associated with the development of this direction

In my short such introduction, I would have remembered only this. I am with a lot of respect for Samsung. For the simple reason that 30 years ago Gennady Borisovich Khomutov and I published some patents and they bought two patents from us. We were still young, inexperienced, hoping that something would come of it. But they quietly bought our patents and put them under the cloth. Since then, there has been no development of this direction. And I love this company, in quotes, so to speak, fell in love, and I always follow its achievements. So last week they reported that they had created a pullover, an ordinary pullover, inside of which there are systems that allow you to accumulate electricity as a result of the activity of the human body, both its heat and its movement, and this electricity is enough to charge your gadget. Any. From this pullover.

This suggests that research and practical developments in this direction are very intensive. Those who follow the literature, knows that now just a boom of work in this direction. And we need to try to find those points, those places where we can be successful in our country and try to develop these directions, come out to the leadership with these or other proposals to support it financially and to ensure that this direction becomes sufficiently significant, if not to say, the key in the development of our branch.

So thank you for attention and turn to our program

3. SILVER, GOLD AND PLATINUM NANO-INK. PRODUCTION AND APPLICATION. **Kim VP, PhD Phys&Math., Project Manager of LLC "AkKo Lab", Moscow**
The company "AkKo Lab" LLC (LLC "AkKo Lab") is a commercial organization that deals with a number of projects, one of which is devoted to printed electronics. The project has

been developing since 2009, and seems to be the first in Russia. Printing technologies are based on printers (aerosol, inkjet, roll, etc.), functional nanoinks (based on polymers and nanoparticles) and electronic devices and components, printed with printers using nanoinks. Advantages of this technology: the flexibility of electronic devices (electronic circuits on flexible substrates - paper, polymer film, textiles, etc.) and economic benefits (cheaper and faster production). The technology is two-stage: direct printing and low-temperature annealing, in contrast to traditional multi-stage chip manufacturing technologies, which include the high-temperature annealing stage. This allows using in this technology flexible substrates that are sensitive to heat (paper, films, clothing, etc.). This involves many commercial companies, government and research groups. Impressive figures are published on the assessment of market volume and growth rates, it is clear that the quality of products is growing and the number of specializing companies is expanding. Along with laboratory experiments and small-scale production, roll-to-roll printers are now being manufactured that allow the printing of large-scale chips, flexible solar cells, printed circuit boards, etc. on a large scale. Now these are hundreds of companies, in which the employees of "AkKo Lab" were convinced, participating in the next exhibition Printed Electronics Europe 2017, held May 10-11 in Berlin. The exhibition was visited by more than 3500 participants, more than 225 companies presented their developments in the field of printer electronics.

The company "AkKo Lab" has developed several types of nanoinks based on metallic nanoparticles - gold, platinum and silver (Fig. 1). To such inks printer manufacturers make very high and specific requirements. There are a number of parameters that need to be maintained in order to use the ink in

the printing of electronic components, in particular, particle concentration, their size, size dispersion, surface tension, viscosity, etc. So if massive silver melts at a temperature of more than 900°C, silver particles with dimensions of about 10 nanometers begin to cake at 100°C, which allows to obtain conductive structures on substrates that degrade at temperatures above 100°C. In 2015, the ink of the company "AkKo Lab" successfully confirmed its quality in the research center of Fujifilm Dimatix, Inc. (Santa Clara, California, USA), one of the largest printer manufacturers. According to the results of these studies, the company "AkKo Lab" is included in the recommendation list of Fujifilm Dimatix, Inc. which consists of 12 companies, available online to all owners of Fujifilm Dimatix printers. "AkKo Lab" is the only company from Russia that passed these test tests. In the list you can see manufacturers of nanoinks from the USA, France, Japan, etc. In general, manufacturers and developers of ink in the world is quite a lot, which is caused by high competition. However, not everyone can demonstrate the quality of the product. After the inclusion of "AkKo Lab" in this recommendatory list, we have orders, mainly from abroad (England, France, Spain, South Korea, etc.). In turn, in Russia, this is devoted to research works carried out by individual scientific groups in universities and commercial structures. In order to increase the sales volume and show the practical suitability of the product, we cooperate with many companies and institutions. The result of such R&D is the printed working electronic devices (Fig. 2, 3), and to bring it to mass production is already the next level that is in Russia at the initial stage. Thus, "AkKo Lab" today is a company that has already established

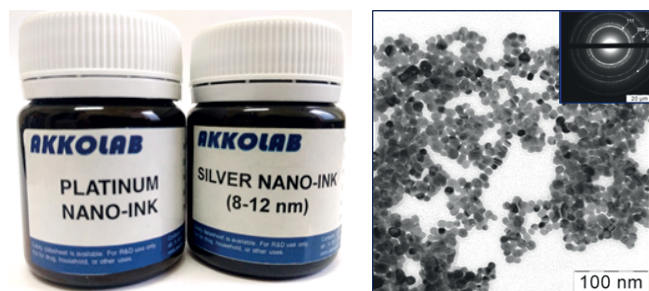


Fig. 1. Nanochernila company "AkKo Lab."

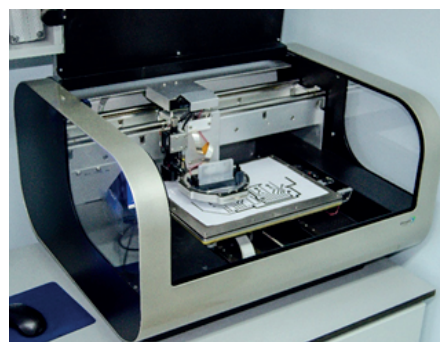


Fig. 2. Printer Fujifilm Dimatix.

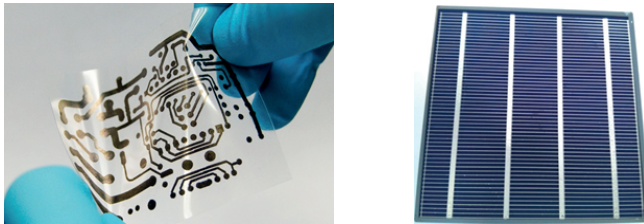


Fig. 3. Printed samples of conductive structures on a transparent film and a solar battery.

a small-scale production and implementation of nanoinks, has confirmed their quality at the highest level and can currently produce nanoinks in volume up to a liter a month. This is not such a large volume, which is in demand in the market. Now the demand is growing, it is necessary to keep up with it and present the appropriate quality of the product. Moreover, in order for the Russian company to take place on the foreign market, it is necessary to cover our activities. On the Internet, the dynamics of news in this area can be monitored on the portal of Printed Electronics World (<https://www.printedelectronicsworld.com>) – the source of global news on printed, organic and flexible electronics. Where we also publish the results of our experimental work. Today, printer technologies are an interesting, rapidly developing and, I'm sure, profitable area.

4. RECENT PROGRESS AND CHALLENGES IN R2R MANUFACTURING OF LARGE AREA PRINTED ELECTRONICS.

Busch Martin, Dr.-Ing., Business Development Manager "Coatema Coating Machinery GmbH" (Dormagen, Germany)

For 40 years Coatema Coating Machinery GmbH has been designing and constructing coating and laminating equipment for fabrics, carpets, artificial leather, etc. Most substrates



Fig. 4. Flexible autonomous cost efficient energy source and storage.

and chemicals can be treated with Coatema equipment either in sheet form or from rolls. Approximately since 2003, Coatema focuses on new markets, now a third of our equipment – for the production of printed electronics. Coatema equipment develops and manufactures advanced flexible electronic technologies, such as OLED lamps and signboards, organic sensors, smart packaging, OLED displays, optical coatings, RFID applications and flexible printing processes. There is a large equipment for this. First we produced small coatings, searched for suitable chemistry, viscosity and other parameters on small machines, the smallest shaft-on-shaft machine by 500 mm, then more, now – the



Fig. 5. R2R in nitrogen environment

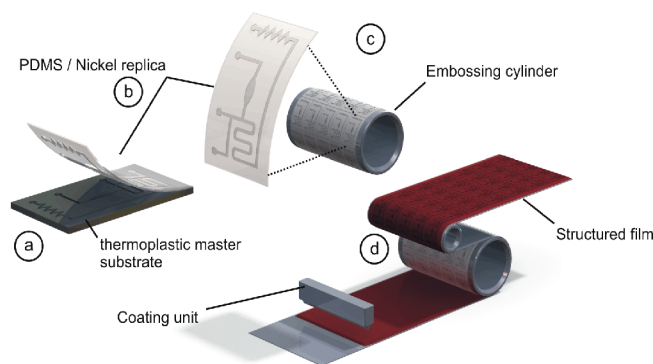


Fig. 6. *Nanoimprinting system.*

largest line in Europe, on which a 55 m long substrate is produced.

To solve the problems, there are more than 30 different spray systems and systems for printing. The most interesting system for encapsulation, which protects electronics and ink from water, oxygen and other gases. It is used not only for protection, but also as a function, when it is necessary to have a very even layer of electrolyte on a large scale. With a low viscosity, it is difficult to obtain an even and good surface. A mask is used in which the ink lies where necessary. Last year, a new scheme was applied, usually this is one unit, which has a hole that allows to make minimal movements when applying ink. This works about 2 milliseconds, very quickly, which is not an easy task for production. Other systems, for very small structures (micrometers) are slow, for large structures can be faster, the system is very dense and flexible, because the costs for a single substrate are the same as for a macroprint. New systems that use microstructures or nanostructures allow printing up to 50-70 nm. Earlier it could be realized only with the use of vacuum systems. Now we dispense with this and with a roll press. The liquid polymer is applied to the film substrate, the structure is printed in the micro- and nanometer mode, at the same time here it is dried by ultraviolet and then separated from the shaft. This structure is already in a solid state. This gives great opportunities for different systems, for example, for displays

– more light, for photovoltaic it absorbs better, for nutrient media – bacteria can not grow well, because structure hinders.

The firm invites to itself to Germany if not to buy cars, then to try on them the systems.

5. CREATION OF A CLUSTER OF PRINTED ELECTRONICS ON THE BASIS OF THE CENTER FOR NANOTECHNOLOGIES AND NANOMATERIALS OF THE REPUBLIC OF MORDOVIA. Krakhin D.N., Dir. of Center for Nanotechnologies and Nanomaterials of the Republic of Mordovia, Saransk.

The topic of the report is not so much printer technology, as the organization of business on these technologies. Our experience shows that this business is promising.

Nanocentre of the Republic of Mordovia is a joint venture between Rusnano and the Republic of Mordovia, i.e. Rusnano with their source – the budget, and the republic, and the center invests this money in the company that it creates. The center is part of the venture-building network of nanocenters, which is organized by the structures of Rusnano. For today, there are 15 nanocenter in Russia, which annually from scratch, create 150-200 start-ups, and the result of this work for a few years now in Russia created about 900 technological start-ups, this is half of all operating start-ups in Russia. We work in the technical sphere, we do not deal with IT, it's the business of Rusnano.

Nanocenter as a whole is a business to create a business, the nanocenter tries to serially create companies for subsequent sale and make it faster and cheaper than is customary. Throughout the world, start-up technology companies are developing from scratch to success for about 20 years. We are trying to reduce this period to 10 years due to the fact that we add a certain component of seriality and by investing in the infrastructure of the chosen specialization.

Nanocentre of Mordovia has chosen for itself the following specialization – power electronics,

new materials, modern lighting technology, devices. For 5 years of operation, the nanocenter created about 50 startups with different specializations, and printing technologies in this portfolio occupy a key role.

The choice of this industry – printing technology, happened by chance. Several years ago Saransk visited the Finnish company VTT (Oulu) for the production of light-emitting technologies. We managed to conclude a transfer agreement with her on this part of the technology, we invested a corresponding start-up, which for today promotes the serial production of a light-emitting film produced by a roll method, its conductive tracks are printed on a polymer substrate, LEDs are mounted and we get some super- which is used with such a form factor, where before the advent of such technology it was impossible to use light. An example is a windshield of a bus where the film is laminated inside the glass and can be a full-fledged display for indicating route information. Today it is a pilot project of the world's leading glass manufacturer. Other applications are possible that allow the integration of light-emitting elements into building materials, wallpaper-like materials, textile elements, etc. To date, this is one of the few examples of the use of printed technology. A joint center in collaboration with the Finns has been created to improve this technology and develop practical aspects of its application.

A research center for printed electronics is being created, focusing on sheet printing and the creation of hybrid electronics. Defined several key tasks. First and foremost – application applications through the creation of start-ups, in close communication with different partners, in order to obtain up-to-date information about where this industry is heading. It is planned to work not only on applied things, but also with materials, arranging some kind of vertical integration of this direction, in the future we will scale

our activities, because in the laboratory scale it is impossible to conduct business.

A laboratory equipped with the most up-to-date equipment for printed electronics was created (**Fig. 7**): these are the preparation facilities for substrates, printers, equipment for drying the material, analytical equipment, a glovebox for working in an inert environment, everything necessary to work in this direction. The created team is already working on the selection of materials, development of printing methods, the creation of components, some integrated devices for the use of printed methods. The company has implemented several custom-made R&D, for example, methods have been developed for manufacturing a laminating film for low-temperature sintering for a large power electronics plant in Saransk, radio frequency modification methods for one of the Rusnano project companies, etc.

To date, the world is serious about replacing silicon chips with plastic materials with radio frequency modification. On such a plastic chip we apply a printed UHF RFID antenna based on an electroconductive paste of our own production (working range – UHF, reading range 3 m), in a single technological cycle a label is made and printed on the product package. Now this is a general trend, when in the production of a product such a label is sewn up to carry out tracking of products throughout its life cycle.

Another one of our product is stretchable



Fig. 7. *Laboratory of printed electronics.*

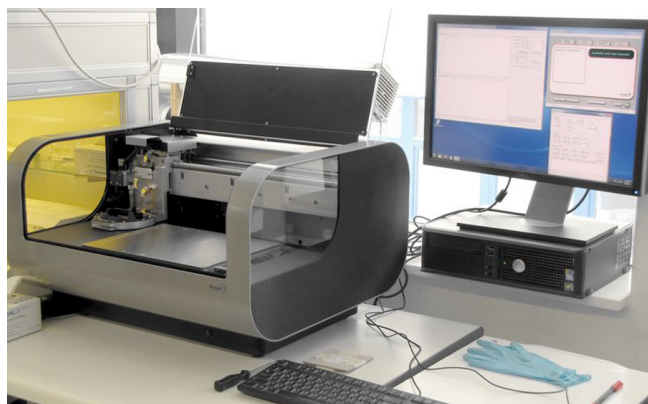


Fig. 8. *Stretched current-conducting paste.*

electrically conductive pastes (**Fig. 8**). For clothing, it is important that the ink that provides current carrying is in the elements that stretch. It was possible to develop a stretchable paste, which is not inferior to the international analogs declared in open sources, but we are still making a substantial reduction in the cost of this paste due to the introduction of metals in addition to silver. For example, copper, coated with silver - the cost of the paste fell by 20-30%.

In 2016, our company TC "Printing Technologies" became a member of the Finnish industrial cluster PrintoCent, which includes more than 40 companies from around the world - dozens of startups, SME companies such as ASUS GROUP, LSE companies such as Nokia, BASF, etc. Such clusters include not only research and development centers, there are large businesses that form today's request for the technology of printed electronics for its subsequent introduction into their products. Companies such as the manufacturer of sheet equipment Konen, the glass company Pilkington, the Finnish manufacturer of wearable electronics are companies with multimillion-dollar turnovers, plus those stratapes that produce certain series around this infrastructure.

Startup is a product company that forms its product based on market requirements, potential consumers. One example - the startup PrintoSense solves the problem of bringing to the market modern print sensors for various applications. The company has established a small-scale production of sensors: biosensors, capacitive sensors, piezoresistive and piezoelectric, optical, temperature and humidity sensors, gas

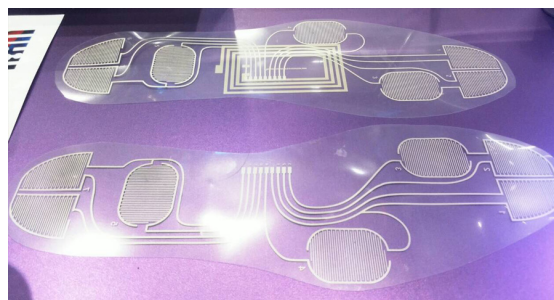


Fig. 9. *Insoles for shoes with built-in pressure sensors.*

sensors, pressure sensors. There is a whole catalog of sensors that are widely used in the same automobile industry - tire pressure, measuring the fit of the windshield wiper against the glass, the density of the doors, as well as various examples of ergonomic applications, such as chairs, where you need to measure the degree of depression. Bending sensors - measuring the degree of bending of elements in robotics, fitness, sports equipment, orthopedics, restorative medicine, in the gaming industry. Startup SmartStep - manufacture of insoles for sports, for medical rehabilitation (**Fig. 9**). Flexible LED RGB screen, displays on the basis of transparent, thin films used in windows, which do not yet serve as an advertising element, provide light transmission from the outside, and outside can carry information for stores, service centers, including decorative.

We are now at the very beginning of the journey, we have created a laboratory, a certain system of start-ups and partners. Next year, we plan to invest in contract production, semi-industrial, for 1-10 thousand pieces of products. In the future, we need to scale up to full-fledged production, so that those startups with whom we work can serially produce these products. Thus, this message shows the cluster and its components with the prospect of creating an industrial structure with developed cooperation.

6. MICROPLOTTER PRINT OF ELECTRODES FOR ULTRATHIN ORGANIC FIELD-EFFECT TRANSISTORS.

Parashchuk DYu, Dr Sci Phys&Math, Prof., Physics Faculty, Lomonosov Moscow State University, International Laser Center of MSU.

Organic electronics is a booming branch. At the Physics Faculty of the Lomonosov Moscow

State University there is the laboratory of organic electronics (Chair of General Physics and Wave Processes), mostly young people, there is an annual school in the Moscow region, the 4th school on organic electronics has already passed.

In organic electronics, low cost, flexibility, and transparency are attracted. In terms of speed, organic electronics is far from silicon. You can do not fast computers, but lighting devices, sensors, sensors, batteries (solar), etc. Another problem is instability of organic matter.

The problem of forming an organic transistor is solved on a silicon substrate no more than a centimeter, we clean it, we check the surface, we introduce the transistors with a microplotter. An organic transistor is a device about three electrodes, has an active layer, and two drain-source electrodes that form an ohmic contact. The third electrode is a branch, it is separated by an insulator, with the help of a voltage on the gate it is possible to change the conductivity of an organic conductor. This is the basis of all devices. The carrier layer has a size of the order of one molecule (1 nm), where the charge carriers move in contact with the dielectric. The main characteristic of such a device is the mobility of a charge carrier of tens of cm per square inch, amorphous silicon is about 1. Such transistors can already be comparable or better than amorphous silicon transistors that are used on all liquid crystal screens.

When we print the electrodes, we need from ink in addition to their viscosity-type parameters, etc., the work function for these inks. It is determined by the metal that is there, and its size. Because when it comes to semiconductor devices, we need to ensure the injection of electrons into either the valence band or the conduction band of electrons. Therefore, you need to have metals with different work functions. And not like gold (in gold ink) about 5 eV, but much lower and much higher. For all light-emitting devices, it is necessary to ensure the injection of electrons and holes, so that the electron is at the level of 3 eV, and the hole is 5 eV, then luminescence will

appear and the energy of the transition will go to light.

We are working on ultrathin organic transistors of a molecule-wide thickness and the production of electron and hole conductivity by liquid-phase methods. Transistors with such conductivity allow creating a light-emitting device. Substances such as teraphene phenylene oligomers with ten alkyl substituents, and other substances with electron and hole conductivity or only with hole conductivity were used. At this stage, only hole conductivity was investigated. As the semiconductor layer, ultrathin crystals obtained by annealing in solvent vapors were used. Growth of the semiconductor layer in the solvent vapor (quite a new direction): a solution with a concentration of 0.11-0.23 g/l is applied to the cleaned substrate, the substrate is centrifuged, unwound at a speed of 200-1000 rpm (the parameter varies), then the substrate is placed in a closed atmosphere in a Petri dish) for 4 hours at room temperature, is closed, where crystal growth occurs. Using a concentration of 0.13 g/l provides for the production of thin crystals of large area. X-ray diffraction analysis showed that the oligomer used gives a monolayer single crystal of very large dimensions.

Then, using liquid-phase methods, electrodes are applied to these layers. We use the method of plotter microprinting on a silicon substrate. The microplotter (GIX Miroplotter Desktop (SonoPlot), **Fig. 10**) is equipped with a 3D



Fig. 10. The microplotter GIX Miroplotter Desktop (SonoPlot)

positioner with a precision of 20 microns for accurate application of liquid substances (points, continuous lines, arcs) as electronics components. Equipped with a piezoelectric dispenser (a minimum volume of 1.8 picles, a viscosity of not more than 450 cPs) for non-contact drawing of a pattern with a minimum element size of 30 microns. Equipped with a digital video camer.

As the ink used PEDOT:PSS, mixed with dimethyl sulfoxide, which increases the conductivity of the electrodes. Water is usually added. To reduce the work function, a surfactant was sometimes added to closely adhere the electrode to the crystal. But the surfactant destroys the contact area of the crystal and then was not used in the manufacture of transistors. Printing technology – drip or solid. Drip application to the right and left of the crystal creates a semiconductor channel, but the drop destroys contact with the crystal, being carried away by the capillary. Solid print – the capillary moves along the surface of the substrate.

After drying, the transistors are scratched out (so that there is no leakage of charge), separated from each other, using a micropipette or a special probe under a microscope and placed in an argon atmosphere. We get an organic semiconductor transistor and examine its characteristics.

Characteristics of transistors based on an ultra-thin crystal DD-5T (**Table 1**). The current volt-ampere curves show that the obtained values of the transfer characteristics in the saturated mode ($V_{sat} = -50B$) and the output characteristics are not high, but in such a thin crystal at low currents the current density is very high, besides these substances have luminescent properties. I.e. it is possible to combine the properties of conductivity and luminescence.

Table 1

Characteristics of transistors based on an ultra-thin crystal DD-5T.

Saturated Mode			Linear Mode	
$\mu_{sat}, \text{sm}^2/\text{Vs}$	V_{Tsat}, B	I_{on}/I_{off}	$\mu_{lin}, \text{sm}^2/\text{Vs}$	V_{Tlin}, B
0.310±0.015	+28	7500	0.25±0.013	+26

Advantages. 1. High characteristics of devices: on these substances with the help of other methods, higher characteristics were not obtained. 2. Ease of use: do not use vacuum methods to printing electrodes. 3. The devices do not degrade over time (which is not always possible with organic electrodes): the mobility does not change for 3-4 months.

Disadvantages – it is not always possible to form a semiconductor channel, you may need to use other inks.

So, in our work, optimal "ink" was selected for printing electrodes. Using printed methods, transistors with high hole conductivity were obtained on the basis of ultrathin crystals.

Requires "ink" for electrodes for efficient injection into wide-band organic semiconductors with an output function of 5.5-6 eV for holes and 4 eV for electrons, so that recombination of electrons and holes can occur with the release of a quantum of light.

7. FUNCTIONAL INKS BASED ON METAL COORDINATION COMPOUNDS FOR THE CREATION OF THIN-FILM OXIDE NANOSTRUCTURES USING PRINTED TECHNOLOGIES. Simonenko NP, PhD Techn., Kurnakov IGIC RAS, Moscow

Thin-film structures are in demand when creating transistors, receptor layers in sensorics, detectors of various gases, solar batteries, energy storage devices, transparent electrodes and various optical devices. The technology for the production of functional ink is also rapidly growing in interest in the technologies for creating thin-film structures based on them. The main methods for obtaining thin films are chemical CVD and physical PVD deposition of the gas phase, dip-coating, spin-coating and, more recently, called additive technologies. Additive Manufacturing (3D printing, layered synthesis): stereolithography, fusing, selective laser sintering, laser sintering of metal, 3D printing, lamination, inkjet printing with polymers and inkjet printing with ink. As the most popular is such additive technology as

inkjet printing inks. As the ink are a variety of liquid media – dispersions, solutions of different viscosities, etc. We in our work in cooperation with AkKo Lab and MIPT used such printing devices to create various thin film structures like the Dimatix DMP-2831 inkjet printer and the Sonoplot GIX Microplotter II microplotter. There are a lot of devices for printing, printing technologies are actively developing, but in order to create structures of complex chemical composition, a problem arises in functional inks. These inks, in addition to what is lacking, must still be subject to rheological requirements, and etc. properties. When printing dispersions of nanoparticles, as is known, there are big problems, this is the effect of a "coffee stain", when the solid phase of the ink is distributed unevenly over the substrate and some structures are formed. This process is difficult to control, it is difficult to predict the electrophysical and other functional properties of the resulting materials. In addition, the use of nanoparticles results in clogging of printheads with nanoparticles, there is a need to suppress sedimentation of particles and stabilize these dispersions and sufficiently stringent requirements for the particle sizes that are components of these inks.

As a functional ink, we propose to use not the dispersions of nanoparticles (without detracting from their merits), but the true solutions of the coordination compounds of metals with the specified composition of the coordination sphere. These solutions (in organic solvents), in connection with what are true, immediately eliminate some of the disadvantages of the dispersions. There is no big problem associated with sedimentation of particles, the effect of the "coffee stain" is suppressed, the process of clogging of the printheads is eliminated. Thus, using these solutions, it is possible to apply thin films on different substrates. At the first stage we apply a film of a solution based on heteroligand metal complexes. Due to the processes of

polycondensation, hydrolysis, a cross-linking occurs, a polymeric coating is formed in the form of a polymer network. The next step is the crystallization under various influences – temperatures, optical effects, etc. At the same time, a crystalline oxide coating is formed whose properties – thickness, roughness, porosity – depend on the properties of the initial components, which are coordination compounds with a given reactivity. We obtain coordination compounds of the given chemical composition, we study the coordination environment, the degree of screening of the central atoms affects the rheological properties of the functional inks obtained. In particular, the dependence of the rheological properties of ink solutions on the composition of the coordination sphere is given as an example. As can be seen, the degree of replacement of one ligand by another ligand by several percent leads to a change in the kinetics, a change in rheological properties by an order of magnitude. That one can use and control the processes of structuring, self-assembly on a substrate. As an example, we obtained a thin film of nickel oxide. The temperature dependence shows that in the range from room temperature to about 200°C, the electrical resistance decreases by 3 orders of magnitude. In addition, it is shown that the thickness of the film significantly affects the electrophysical properties. In particular, if the number of layers increases by a factor of 2, then the resistance can be reduced by several times.

On the example of manganese dioxide, a similar experiment was conducted: a xerogel film was applied to the specialized sensor using manganese coordination compounds. The film was subjected to a stepwise heat treatment. The temperature dependence of the electrical resistivity shows that in the course of this treatment the process of crystallization of manganese oxide proceeded and the resistance in the temperature range

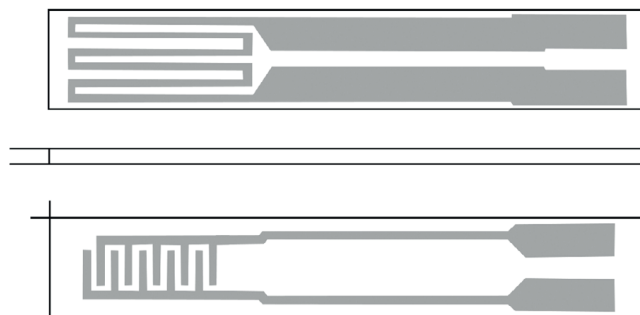


Fig. 11. Scheme of the sensor; white color - Al_2O_3 -ceramic, gray - Pt-electrodes and microheater.

from room temperature to $200^\circ C$ decreases by 3 orders of magnitude or more.

In cooperation with AkKo Lab, we printed with our inks – titanium oxide doped with zirconium TiO_2-ZrO_2 was applied by three layers of functional ink (10 mol%) to the region of the interdigital probe electrodes (**Fig. 11**, bottom, left) by high-resolution inkjet printing method. A polymer film was formed, with subsequent heat treatment, titanium oxide doped with zirconium crystallized. The film is very thin, not individually fixed. With the help of Raman spectroscopy it has been shown that it does exist. The microstructure was studied by scanning electron microscopy. It is seen that this film is a grid consisting of particles of about 10-20 nm in size, arranged in a certain way. It should be noted that there are also defects in the size of hundreds of nm, sometimes microns. They are caused primarily by the heterogeneity of the substrate, in this case, its roughness of tens of micrometers. This is critical for such thin films, therefore the quality of the substrate determines further functional properties. It was shown that the size of one pixel of a given composition of titanium oxide doped with zirconium is approximately $35 \mu m$, the structure is obtained using a Dimatix printer.

The obtained film of titanium oxide with zirconium was studied for the fact of detection of various gases. It has been shown that when using it as a component of resistive sensors, the concentration of oxygen can be detected in a wide range: the resistance of the film increases with increasing contact with oxygen, this response

increases with decreasing operating temperature of the sensor. It is also shown that the stability of this response during playback is high enough.

With the help of a microplotter, the processes of printing thin-film structures were also studied. In particular, in cooperation with MIPT, structures of various shapes, including concentric circles of manganese and in the form of a grid, were obtained on glass substrates. Quartz and silicon substrates also produced concentric circles of CeO_2-ZrO_2 , with a line width in the range of 100-200 μm approximately. Thin-film structures of cerium oxide composition were obtained on alumina substrates. It was shown that the speed of moving the needle of the microplotter significantly affects the microstructure of the film systems, and with increasing the displacement of the needle from 1 mm/s to 5 it can be seen that the structures are uneven.

It has also been shown that the ink created on the basis of coordination compounds can be used in hand-held type printers of the type of markers into which these inks can be poured and manually create some thin-film structures, in particular, a line width of about 500 μm was obtained.

Thus, as a result of our work, a technology was developed to produce functional inks based on metal coordination compounds to create thin-film nanostructures of complex chemical composition using high-resolution printing technology. It is shown that the obtained thin oxide films can be used as receptor components of resistive gas sensors and in other applications, depending on their chemical composition.

8. AEROSOL CVD SYNTHESIS OF SINGLE-WALLED CARBON NANOTUBES FOR FLEXIBLE ELECTRONICS. Albert G.

Nasibulin, Dr Sci Techn, Prof. of the Skolkovo Institute of Science and Technology, Moscow

While in Finland, at the Helsinki Aalto University, where I worked for 16 years, we developed a method for producing single-walled carbon nanotubes (SWNTs) in the gas phase, an aerosol CVD method for their synthesis [2]. I will explain

my method using the example of the ferrocene vapor $FeC_{10}H_{10}$ decomposition method (Fig. 12). Ferrocene is an organometallic compound, quite volatile at room temperature and at a pressure of 8 pascals, blowing carbon monoxide, which in this case plays two roles: a carrier gas and a carbon source for the growth of nanotubes. Carbon monoxide passes through the cartridge, which is filled with ferrocene powder, saturated with vapors, and then the vapor-gas mixture enters the water-cooled pipe directly into the hot reactor with a temperature of about $1000^{\circ}C$. In it, ferrocene decomposes, as a result - catalytic iron nanoparticles are formed and on the surface we have the decomposition of carbon monoxide, as a result – the release of atomic carbon, which is necessary for the growth of carbon nanotubes. The vapor-gas mixture, the entire flow in the reactor is about 12-15 seconds, during this time it is necessary to control all the growth processes. At the output, the nanotubes collect on the filter. It is removed from any substrate (silicon, glass, flexible lavsan, etc.), a polymer film, usually in advance, for better adhesion, rubbed with alcohol or acetonitrile. And as a rule, with the addition of gold chloride – to simultaneously dope the resulting network of nanotubes, which increases

their conductivity by 5-10 times. The film of tubes on the substrate sits tightly, it is not possible to tear off the usual scotch tape. It is planned to measure adhesion due to van der Waals forces between the substrate and nanotubes in numbers with a device that the cat has just bought. With a filter, nanotubes go off easily, because the filter is made in the form of fibers and contact with the tubes is very small. When we push the substrate, these connections arise.

Single-layer carbon nanotubes form a rather high quality randomly oriented networks nanotubes (1-2.5 nm), which is confirmed by the Raman spectra (Fig. 13a): the presence of a radial

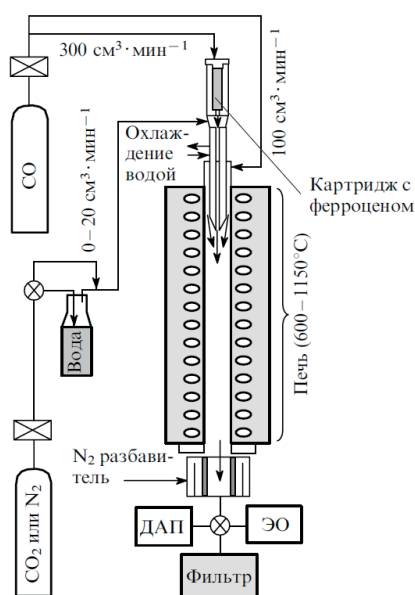


Fig. 12. Aerosol method for the synthesis of single-walled carbon nanotubes (DAP - differential mobility analyzer, EO - electrostatic precipitator)

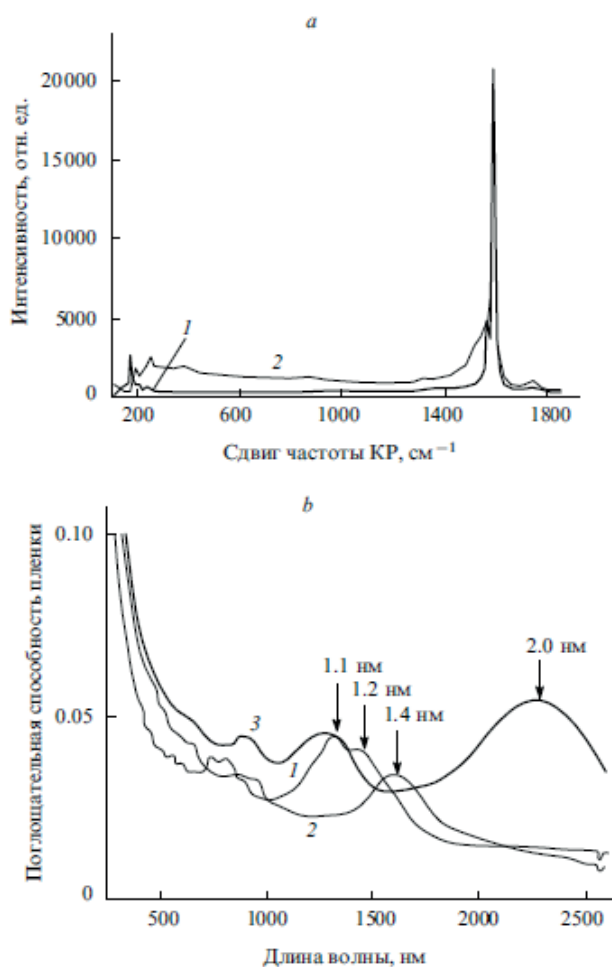


Fig. 13. Results of research of SWCNT synthesized in the process of the ferrocene decomposition: a - Raman spectra for excitation wavelengths 488 (1) and 633 nm (2), b - absorption spectra of SWCNTs synthesized with various additions of carbon dioxide (1 - 0, 2 - 0.5%, 3 - 1.0%) and a temperature of $890^{\circ}C$. The arrows indicate the mean diameters of SWCNTs calculated for electronic transitions between the first Van Hove singularities.

respiratory mode (RDM) at low frequencies ($100\text{--}200\text{ cm}^{-1}$) in Raman spectra indicates the presence of SWCNTs. A special feature of the spectra is a strong Auger band (with a peak at 1592 cm^{-1}) and a low *D*-band intensity (about 1300 cm^{-1}), indicating a small fraction of the disordered carbon in the synthesis products. Fig. 11b – optical absorption spectra of SWCNT at different concentrations of carbon dioxide, the peaks correspond to electron transitions in nanotubes. By changing the concentration of carbon dioxide in the reactor, it is possible to significantly change the diameter of nanotubes, in fact covering the entire spectrum from ultraviolet to near infrared.

A method for preparing electrodes is proposed – dry printing, after the reactor, dry transfer of SWCNT from the filter to any substrate, including elastic one. The size of the filter is now brought to the A3 format. If you make special flow limiters under the filter, you can achieve the formation of patterns from nanotubes with a resolution of about 30 microns. In this case, the requirements for the materials of the substrates: all production takes place at room temperature ($<100^\circ\text{C}$), since polymers do not withstand high temperatures. In addition, one of the requirements is low pressure, it is desirable that the whole process occur at atmospheric pressure, with high speed, and should also be compatible with roll printing. The substrate materials currently used, such as silicon and transparent conductive oxides (ITO, ZnO, Cd_2SnO_4 , ...) can not be used. We need alternative materials. A classic example is indium tin oxide (ITO), which is used in 75% of electronic devices as a conductive top layer applied to the polymer. If it is bent, it breaks at a low angle of bending. While the carbon nanotubes on the plastic in the fatigue test at a radius of 1 mm flexion withstand about 30,000 bending cycles before the degradation of electrical conductivity.

On the other hand, if we are talking about transparent films, it is necessary to mention their

surface resistance. Now with ITO, doped with tin on a flexible substrate, it is possible to obtain about 40 ohm per square with a transparency of 90%.

About the work connected with AkKo Lab: we bought graphene oxide from it, dispersed it, applied it to the surface of nanotubes, obtained a hybrid material, reconstituted at atmospheric pressure and temperature of 300°C , dripped gold chloride AuCl_3 and obtained a good conductivity of 34 ohms per square at 80% transparency.

Our nanotubes can also be used to create thin-film field-effect transistors. So in 2011 on polycrystalline silicon received a ratio of currents of 10^6 , in 2013, mobility and charge mobility surpassed 10^7 .

In addition, our material can be used to create organic light-emitting diodes (OLEDs) and capacitive touch sensors. The first sensor of 2010, our company together with Nokia introduced these nanotubes into mobile phones, cars that contain touch sensors made of single-walled carbon nanotubes by our technology are already being sold.

In addition, our films can be used in solar batteries, on organic dyes, on heterojunctions, when we put carbon nanotubes on the *n*-type silicon, we are doping *p*-type, and thus obtain a *p-n* junction on crystalline silicon of the order of 14%. On amorphous silicon while 2.7%.

Another one of our project is elastic electronics. We had an ambitious goal to combine flexible, transparent and elastic electronics into one component. Carbon nanotubes applied to the elastomer can withstand tens of thousands of tensile tests. On the other hand, these same carbon nanotubes can be used as motion detectors, if applied to a carbon nanotube, which in principle can not be done with metals. Carbon nanotubes, films with stretching occupy the most favorable energy position and when stretched twice the resistance of the material changes by only 1%. The reason for this stability: conducted an in situ study inside an atomic electron microscope to see what happens to nanotubes when stretched.

With a 20-40% stretch, the nanotubes become oriented along the stretch. When we were stretched by 55% and released, wrinkles formed, which ensure the unchangeability of the electrical resistance during stretching. In operation with elastic supercapacitors, the capacitance was not high, but at 120% stretching the characteristics of the supercapacitor do not practically change. That is, it is proved that this material is suitable for high-elastic electronics.

In cooperation with the Lomonosov Moscow State University, work was done to create a loudspeaker made from SWCNT. Here, the SWCNT film is in a freely suspended state, there is no substrate. An example is a SWCNT film $1.0 \times 1.0 \text{ cm}^2$, a thickness of 20 nm, a resistance of 110 ohms, a distance to a microphone of 3 cm. In conventional loudspeakers, there are membranes that push air, in this case nanotubes do not move, the sound is produced by the fact that the film is very quickly heats up and cools – so called thermoacoustic effect. Now we check whether it is possible to use such films for something useful. It turned out that such a film generates an ultrasound up to 100 kHz and a comparison with the literature data shows that this film exceeds the available analogues in its characteristics.

In cooperation with Novosibirsk State University, work was done on the use of the SWCNT film as an IR photodetector (so-called bolometer): a quartz substrate was coated with a hybrid film, gold electrodes for detecting a change in the resistance of the film with heating; this detector is faster than industrial samples in terms of its speed. If you want to force the film to absorb in a narrow IR range, you need to perforate half the film and thus you can force the film to absorb in a certain narrow spectral range.

In addition, our nanotubes can be used as saturable absorbers. A cheap Chinese laser, Er-fiber, was used, a small number of tubes were applied to the tip of this fiber, about 30 ng is sufficient, and depending on the conditions of

use, nanosecond and subpicosecond pulses can be recorded.

Another project – an electronic "nose" based on nanotube networks, the task of digitizing the smell, make this device not only highly sensitive, but also highly selective.

From CNT, which we synthesize by the aerosol method, it is possible to obtain not only a film, but also fibers. It is possible to pull fibers with a diameter of about 20 μm with good mechanical and electrical properties that can be used for many applications – as current collectors in solar cells.

Thus, the aerosol method of synthesizing thin-walled CNTs and preparing transparent electrodes are promising methods for their commercialization in future flexible and elastic electronics. Features of the technology: room temperature, vacuum-free technology, simple and fast process, cheap. The goal is to create a large and low-cost production component for flexible and transparent electronics using R2R roll technology.

9. PRINTER TECHNOLOGY IN ELECTRONICS. Isaykin A.V., Dir. LLC TC "Printing Technologies", Saransk.

Core technology to create printed electronics: Chemical Bath, Spin-coating, Dip-coating, Doctor Blade, Metering Rod, Slot-casting, Spray-coating, Screen Printing, InkJet Printing, Aerosol Jet. There are two markets – the materials market and the equipment market. Our company positions itself as a developer of both printing methods and new materials. Analyzing the relevant literature, we chose the key development factor – the development of stretchable electronics. The base is conductive elastic composites, which have a wide range of applications, mainly in portable electronics. We have concentrated on the development and analysis of commercial products that can cover this niche. At the moment, there are only a limited number of such elastic compositions that have high resistance and stretchability. Often additive methods are used, such as the

use of lamination of textiles, double lamination, the application of conventional polymer phases and post lamination, but these are not exactly elastic composites. After a series of tests, we have developed a composition: elastomer (high stretchability) and conductive filler - electroconductive paste, the characteristics superior to the existing analogues, based on copper, coated with silver (electrodeposition of Cu in the AgNO_3 solution) to reduce the amount of silver in the final product and, accordingly, of the cost by 20-30%. The paste impregnates the fabric due to the capillary effect, silver penetrates inside, envelops the fibers of the fabric, not over the surface, as in lamination. When stretching almost 2 times, the conductivity naturally falls, but remains high enough. Another feature of the approach is the use of reactive additives, MOD-precursors (carboxylic acids), functional additives. In the course of the thermal action, as a result of thermal destruction, they generate *in situ* particles, both micro- and silver nanoparticles. The dispersity of silver nanoparticles is quite high. We use the principle of coating hybridization, filling with various pastes, to obtain layered structures. The composition was successful, together with the Lobachevsky University (Nizhny Novgorod), INGsystems are created, the seal fits into them.

In addition, the company is developing a project with thin-film surfactants. The main problem of electrically conductive pastes is an increased electrical resistance compared to conventional conductors. To solve it, the following approach is applied. A polymer surfactant ($60 \pm 2\%$ by weight) was added to the paste. Drying of printing layers is carried out at an elevated temperature of 120°C with the formation of silver nanoparticles *in situ*, which substantially increases the conductivity. The electrical resistance of the printed layers was reduced by 20-25% without deterioration of adhesion, resistance to weathering and flexibility. This correlates with the world data.

10. 2D PRINTING OF TEST HETEROSTRUCTURES WITH MATERIALS BASED ON GRAPHENE.

Irina V. Antonova, Dr Sci Phys&Math, Senior Researcher Rzhanov Institute of Semiconductor Physics of SB RAS (Novosibirsk).

Within the framework of the RNF 15-12-00008, within 3 years, work was carried out in a new area for us – the creation of graphene suspensions and liquid compositions for 2D printing from graphene-based materials. All approaches known from the literature were studied and a method for obtaining particles by electrochemical stratification of graphite and subsequent treatment with a dispersant (particle thickness 1-3 nm, lateral size 1-5 μm) or ultrasound was selected, breaking them down to smaller particles and obtaining a high yield of single-, two and three-layer particles (**Fig. 14**). Electrochemical stratification of graphite usually produces slightly oxidized (20-30%) graphene, the use of which allows to significantly reduce the annealing temperature (300°C) to restore conductivity. The problem of the stability of suspensions and ink after recycling a number of organic solvents was solved in favor of aqueous solutions.

The films and structures were fabricated using a two-dimensional printing method on a Dimatix Fujifilm DMP-2831 printer equipped with a DMC-11610 print head with 16 nozzle carriers of about 20 μm in diameter. Ink – with particles less than 400 nm. The printing process was realized both on solid and on flexible substrates. The solid substrates

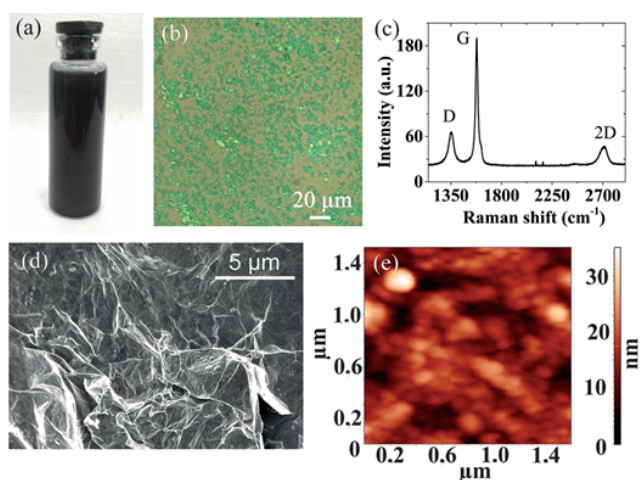


Fig. 14. (a) graphene suspension, (b) optical image of graphene flakes, (c) Raman spectrum of 2-3 nm thick suspension particles, (d and e) SEM and AFM images of films prepared from the graphene suspension.

were silica SiO₂/Si with an oxide thickness of 300 nm, coated with APTES (3-Aminopropyl) threethoxysilane film to ensure good adhesion of the water-based ink. Flexible substrates are polyethylene terephthalate (PET) substrates with an adhesive coating (Lamond), Epson inkjet printers and polyamide films (Kapton).

Resistance of layers of graphene ink: layer > 200 nm – 200 ohm/sq, 20-40 nm – 1-3 kOhm/sq, 3 nm – 16 mOhm/sq. The main work – on films from 1 to 30 nm, droplets of the order of 3 nm had a resistance of the order of megOhms. The maximum mobility of 100 cm²/Vs was observed in films of monolayer or bilayer particles of the order of 1 nm on a SiO₂/Si substrate. As the particle size increases, the mobility decreases sharply. When PEDOT:PSS was added to improve the liquid composition, the mobility decreased during printing and over time the resistance changed much more than when printing simply with graphene.

The second material we use is fluorographene (FG), which is obtained by fluorinating a suspension of graphene in an aqueous solution of hydrofluoric acid. With strong fluorination, we obtain particles with a lateral dimension of 20-50 nm and a thickness of up to 2 nm. Suspensions are absolutely transparent, when printing a film (without surfactant), the surface relief is about 2 nm with a roughness of 0.3 nm. Transparency of films at thicknesses of about 20 nm is 97-98% in the visible range. The low-point leakage (<10⁻⁴ A/cm²), ultra-low charge in a film and on a heterointerface with Si, GsAs, InAs: Q = (1-4) 10¹⁰cm⁻² are measured on the MIS structures on a silicon substrate (FG and contacts) (droplets) Q = (0.5-2) 10¹⁰cm⁻² (film). Such small charges in other materials are unknown.

Another type of suspension that we use is a suspension of G-NMP (graphene in nitromethylpyrrolidone). However, for very small graphene particles, the conductivity of this suspension is absent. We obtain dielectric films with small leakage currents, with photoluminescence from different layers. There are no applications for this suspension yet.

Fluorographene on flexible substrates has good characteristics (leakage currents, breakdown voltage, etc.) and is very promising as a dielectric film for electronics.

A construction of metal-FG-metal (silver suspension + FG) was printed on paper: the number of printed layers is 10-20, the film thickness is 8-16 nm, the leakage current is 10⁻⁸ A/cm², the breakdown voltage is 10⁷ V/cm.

Hybrid transistor structure: a multigraphene film (2 nm) transferred to a printed FG layer or encapsulated FG. The mobility of electrons has increased several times, for holes has not changed. If the FG film was applied to a flexible substrate, CVD graphene was transferred to it and above it was encapsulated FG, the conductivity of graphene increased 5-6 times.

Graphene oxide (OG). The technology of its production is developed, but if used it as a dielectric layer, it is very unstable. Correction of the properties of such OG layers by printing from the top of a thin layer (2-4 nm) of fluorographene, with graphene oxide having a complex relief and no continuous FG layer; however, its stability increased significantly and the leakage currents of FG/GO 0.2-0.02 mA/cm², those. The leakage currents fell by an order of magnitude (**Fig. 15**).

The production of material for memristors is a two-layer structure of FG/PVA. On a porous matrix of polyvinyl alcohol PVA, a thin film of FG with a metallic contact is printed. On the current-voltage characteristic, go to the open

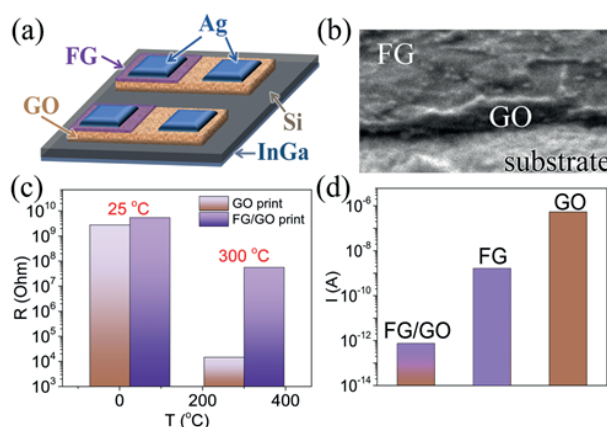


Fig. 15. (a) Test MIS structures with gate dielectrics formed from FG/GO and GO films. (b) SEM image of the two-layer film. (c) Histograms of resistance values in the MIS structures with the FG/GO and GO films before and after an annealing performed at 300°C during 30 min in argon ambient. (d) Histograms of leakage currents across the FG/GO bilayer films, and histograms of leakage currents across the component GO and FG films in the structure.

state, remove the voltage, wait for 4 hours and continue recording – the open state remains, i.e. as an element of memory it works.

The most interesting result obtained by us is the observation of the resistive effect on a composite of FG with vanadium nanoparticles V_2O_5 . The Ag/Fg + V_2O_5 /Ag structure on the flexible substrate exhibited a stable resistive switching effect of ~ 5 -8 orders of magnitude for the FG + V_2O_5 transverse structures with Ag contacts.

Fully printed transistor – printed channel, shutter, metal contacts: substrate – polyimide film, channel from weakly oxidized graphene + annealing 300°C 30 min – 9 k Ω /square, gate insulator – OG + FG, carrier mobility 1-0.2 cm²/Vs, contacts – silver paste 2 ohms/square for a thickness of 400 nm. As a transistor it turned out nothing, the mobility is very small, for bending – 4% at a bending radius of 5 mm. So far – such a beginning.

Graphene dipole antenna at 1.8 GHz. The relief of the edge of the antenna does not exceed 50 μ m, the layer resistance of the graphite layer is 8-20 Ω /sq. The second antenna – 4-6 Ohm/square.

Thus, [3], several variants of suspensions of graphene and slightly oxidized graphene for the formation of conductive layers fluorographene with different degrees of fluorination, and a suspension of graphene functionalized with N-methylpyrrolidone for the production of dielectric layers have been developed. To obtain fluorographene suspensions, a simple and technological fluorination method was developed for the treatment of graphene in an aqueous hydrofluoric acid solution. A Russian patent was obtained and numerous evidence of the fluorination process was obtained. Investigation of the properties of the obtained fluorographene showed that in the case of a relatively low degree of fluorination, a system of quantum dots of graphene embedded in the fluorographene matrix is formed, and the layers obtained from such a slurry exhibit a negative

differential resistance on the current-voltage characteristics, which expands the range of their possible applications. With a greater degree of fluorination of the suspension, films having unique properties of dielectric materials (gate dielectrics, insulating coatings, etc.) are obtained. From the developed suspensions, test instrument structures such as transistors, MIS structures, memristors, capacitors, etc. were printed and investigated.

The main participants of the work are the PhD Med. N.A. Nebogatikova, engineer I.A. Kotin, the leading chemical engineer R.A. Soots, and post-graduate students A.I. Ivanov and E.A. Yakimchuk. Also involved in the project were employees of the laboratory "Graphene Nanotechnologies" of the North-Eastern Federal University named after M.K. Ammosov in the city of Yakutsk under the direction of PhD Phys&Math S.A. Smagulova.

11. CERAMIC "INKS" OF LOW-TEMPERATURE CURING BASED ON INORGANIC MATERIALS. Ivanov A.A., PhD Chem; Tuev V.I., Dr Sci Techn., Dir. Research Institute of LED Technologies of Tomsk State University of Control Systems and Radioelectronics, Tomsk.

In the report with this name, we are not talking about ceramics, but about filled polymers with properties close to ceramic materials. The term "ink" on a serious level is, apparently, used incorrectly. Classes of materials-ink, creating conductive structures, tracks – silver, platinum, copper, as well as materials that create semiconductor structures – polythiophenes, fluorenes and others. To complete the functional range, only dielectric materials – polymethylmethacrylate and others – are missing. But with dielectrics it's not so simple. And the point here is in the solutions of engineering problems, with the removal of heat from semiconductor structures. It is known that the lifetime of reliable semiconductors depends to a large extent on the temperature regime of operation. If at 60°C you can predict

the 50,000th service life of the devices, then at 125°C this lifetime decreases in multiples, and at 150°C you can leave only a limited number of hours or tens of minutes. Therefore, the problem of heat removal during the implementation of engineering solutions is the number one task. Even with the advent of semiconductor light-emitting diodes, this task only worsened. Calculations show that compared to a 40-watt incandescent bulb having an area of 100 cm², a 1-watt LED crystal with an area of 1 mm² requires a substantially higher density of heat dissipation.

I will present some results on the production of materials that can be used in the liquid phase, in the form of ink, for their technological application, with obtaining parameters for thermal conductivity, electrical strength, close to ceramic materials. Ceramics is a sintering material at 1800°C, low-temperature ceramics, widely used in recent times, is 800-1200°C, and the materials I will talk about are 200°C, i.e. this is super-super low-temperature ceramics. The aim of the work was to obtain a material that could be applied with printing technologies and the result of application of which would allow obtaining films with parameters approximating to the parameters of ceramic materials.

As far as the filled polymers are concerned, it is not a secret that polyaluminosilicate is used as a binder here, which, under certain mechanical and chemical treatments, allows to include a relatively large amount of powder that determines the final properties of this product. In the present work, aluminum hydroxide was used. The limitations imposed here are that the film is created on a metal base, on aluminum. Aluminum is chosen here not only because it is light and cosmic material, but based on the chemical affinity of the materials used to create the dielectric layer, and in particular, for this reason, it seems to us that relatively good parameters for the adhesive strength of the films have been obtained. The application

technologies used in the pilot studies, two are screen printing and aerosol printing. The production of ceramic coatings on aluminum surfaces by aerosol printing of the obtained ceramic material was carried out on a Neotech AMT 3D printer of Aerosol Jet 15EX brand, located in OOO NIIIT of OSTEK-Group company in Moscow.

Practically obtained experimentally confirmed technical parameters of dielectric films on a metallic, aluminum base (**Table 1**). The above values of the breakdown voltage, strangely enough, lay on a straight, linear dependence, which in our opinion indicates a high repeatability of deposition of films of different thicknesses. The total value of U_{br} of the obtained insulation coating is 14 ± 0.55 kV/mm.

The value of U_{br} of the sample of the insulation coating (14 kV/mm) is less than the values of U_{br} of the samples of normal Al₂O₃ and AlN ceramics (15.3 and 17.3, respectively). When forming (by screen printing, TP) a layer on a rough aluminum surface with a thickness of more than 100 mm and subsequent low-temperature drying in air at 25°C, during the polycondensation of the polymer matrix, free condensation water forms nanoscale pores and some structural defects that can be seen in photographs cross-section. That causes a smaller value of U_{br} of the sample of insulation coatings compared to UPR of Al₂O₃ and AlN samples, sintered by hot pressing.

Finally, thermal conductivity is the most important parameter for engineering applications. The numerical values of the various powders

Table 1

Electrical strength of insulation coatings

Thickness, mm	Breakdown voltage U_{br} , V
73 ± 0.7	1022 ± 31
54 ± 0.5	756 ± 23
53 ± 0.5	742 ± 22
40 ± 0.4	560 ± 17
27 ± 0.2	378 ± 11
19 ± 0.2	266 ± 8

Table 2

Thermal conductivity of insulation coating

Thickness, mm	Coefficient, W/m·K
73 ± 0.7	18.7 ± 1.7
54 ± 0.5	24.6 ± 2.4
53 ± 0.5	26.7 ± 2.6
40 ± 0.4	30.2 ± 2.9
27 ± 0.2	33.9 ± 3.3
19 ± 0.2	46.5 ± 4.5

obtained in the study are given in **Table 2**. The average thermal conductivity of the coating is 30 ± 2.9 W/m·K with an average coating thickness of 44 ± 0.4 μm. Such a developed material, when used, when designing the electronic component of the base (semiconductor diode housings, complete blocks) allows to provide an acceptable thermal mode of operation of semiconductor devices and operational parameters of the devices being developed.

Experimental results of testing the adhesive strength of the insulation coating have also been obtained. Characteristic curves after a scratch test of a sample of an insulating coating on an aluminum base show that up to 30 Newton per meter is not observed tearing off the material, i.e. accordingly, acoustic emission does not begin and, indirectly, the numerical value of this parameter indicates good adhesion strength of the dielectric coating on the aluminum substrate.

Thus, two important parameters of the dielectric coating have been experimentally confirmed in the values of breakdown voltage and thermal conductivity.

This work was partially supported by the Ministry of Industry and Trade of the Russian Federation..

12. ADDITIVE TECHNOLOGIES FOR GAS SENSORS. ^{1,2}Alexey A. Vasilyev, Dr Sci Techn; ³Nisan AV, ³Potapov GN, ¹Pislyakov A, ³Shakhnovich I, ⁴Samotayev NN, ⁵Tkachev SV, ⁵Kim VP.
¹NRC "Kurchatov Institute", Moscow; ²MFTI, Dolgoprudny, MO; ³RIIT LLC OSTEK enterprise, Moscow, Russia; ⁴NYAU MEPhI, Moscow; ⁵AkKo Lab, LLC.

The printer print of gas sensors is one of the applications of printing technologies, in which the use of high resolution is important. This resolution is possible in such printing technologies as inkjet and aerosol printing. As is known, there are a number of gas sensors: electrochemical, optical (NDIR-non-dispersive infra-red), piezo (microbalance), semiconductor, thermochemical (thermocatalytic), optoacoustic and thermal conductivity. Our subject is semiconductor and thermocatalytic gas sensors.

We have long been working in gas analysis, with gas sensors, semiconductor and thermocatalytic sensors. Their feature is work at a sufficiently high temperature. They use a catalyst, which oxidizes gas-reducing agents with oxygen in the air. And that this chemical reaction proceeds quickly enough, the sensitive layer, semiconducting or simply catalytic, needs to be heated from a temperature of up to 200°C to detect hydrogen from alcohol, to a temperature of 450°C to oxidize a difficult-oxidizing methane molecule.

The technologies used to make such thermocatalytic and semiconductor sensors:

- Volume ceramic technology, the old one, has practically disappeared;
- Wire microcoil for thermocatalytic and semiconductor gas sensors;
- Screen printing – transfer of ink through holes in the printed form;
- Silicon micromachining – silicon microprocessing;
- and finally, what we are now trying to introduce into practice is the technology of ceramic microelectromechanical systems (MEMS).

A modern thermocatalytic sensor used in mines to determine the methane concentration (0.1-10 vol.%) is a small spiral (100 microns in diameter) made of vitrified platinum wire 10 microns in diameter, this spiral is covered with a layer of Al₂O₃ catalyst (about 100 m²/g), doped with platinum and palladium. At an operating temperature of

450°C, such an element consumes about 60 milliwatts; usually a pair of such elements is used – one coated with a catalyst, the other is not. Then the power is in the region of 120-150 milliwatts, in general, a little, but for devices that would like to be used in wireless conditions, networks, cell phones, this power is a bit too much.

We are the only manufacturer in Russia of semiconductor gas sensors manufactured using screen printing technology. The minimum size of the element that can be obtained using this technology is approximately 2.5×0.3×0.1 mm. It is suspended on a 10 mm holder using 10-micron platinum wires. To get a temperature of 450°C, you need to put some electrical power. Today, the minimum that can be achieved in thick-film technology is about 220 milliwatts at 450°C, which is necessary for methane detection. Our goal is to reduce this capacity as much as possible.

One of the options is the work that was carried out with the Italian colleagues (FBK, Trento, Italy) this is the technology of heating up to silicon temperatures. It is a SiO₂/Si₃N₄ silicon substrate, on which a multilayer structure of silicon oxide and silicon nitride is deposited by the CVD method, so that the average stresses in this material are close to zero. A platinum 300×300 micron microheater is formed on it, either by screen printing or inkjet printing, or by some other method. A sensitive layer is deposited, which is a suspension of nanoparticles of a semiconductor oxide, for example, tin oxide in an organic bond. As a result, a film with a thickness of 5-10 microns is obtained, which has a sensitivity to the target gas, and accordingly, in order to heat up to an operating temperature of 450°C, it is necessary to enclose a power of the order of 50 milliwatts in continuous mode (maximum annealing temperature in the furnace is 720°C). Naturally, the concentration of methane can not be measured all the time, you can heat it periodically. Accordingly, using all sorts of

electronic tricks, you can reduce the power to less than a milliwatt, which is quite acceptable in order to work in wireless networks. The lack of this technology - the sensors should not be much. The largest manufacturer of these sensors, which exists in the world, is the Japanese firm Figaro Engineering Inc. (Osaka), about 12 million pieces per year. To start this silicon technology, the initial investment in it is quite large. In addition, all production is a few dozen silicon wafers. The big disadvantage of silicon is that platinum adheres very badly to silicon oxide. In order to obtain a decent adhesion, an adhesion layer of chromium or titanium or tantalum is applied to the platinum. All these metals, unfortunately, at the operating temperature of the sensor 450°C are oxidized. Therefore, platinum exfoliates and the sensor ceases to work.

Several years ago, our competitors appeared on the market - the Japanese firm of Figaro, which now produces silicon MEMSors with the following structure: a microheater suspended on substrates such as legs. It is believed that the membrane structure when heated, and bursts sooner or later. Then when heated, the central part is tucked on these legs and destruction occurs later. Although in general the experiment does not show this.

Another competing firm is the German company Applied Sensor, which is now bought by an Austrian company. Here it is clear that the idea of their Air quality sensor is the same: a microheater on a thin dielectric membrane, a droplet of a gas-sensitive layer is deposited on top, which is tin oxide doped with antimony and a supported palladium catalyst (SnO₂Sb₂O₅/Pd).

To deal with all this, we moved on to another substrate material - aluminum oxide, obtained by anodizing the metal. Platinum, unlike SiO₂/Si₃N₄, adheres well to aluminum oxide, so to produce heaters from platinum there is no need to apply additional adhesion layers, you can simply spray platinum. It can be seen that such a

heater can be heated to a high temperature, for example, to a temperature of 680°C.

The goal is to develop a microheater platform without any shortcomings of existing MEMS devices manufactured using silicon technology:

- a comprehensive technology that requires clean rooms that do not match the scale of production of sensors
- incompatibility of materials used in silicon technology (Si, SiO₂/Si₃N₄-membrane, Pt)
- low efficiency of Pt spraying process and high consumption of precious metal during spraying
- bending of the membrane during temperature cycling, leading to destruction of the microheater.

The mentioned problems of MEMS, in which silicon technology is applied, are the difficulties with adhesion, the high cost of the process. In addition, to spray platinum, spraying is used, which leads to huge unproductive costs of the metal. Therefore it is clear that it is necessary to apply platinum only where it is necessary.

We used those devices that were already mentioned here: Ink-jet Printer Dimatix DMP 2831, which is located in AkKoLab, and the aerosol printing equipment that was in OSTEK, now - in MIPT. If an ink with a viscosity of about 10 centipoise can be used in inkjet printing, then in this installation, when spraying with airflow, an ink with a viscosity of up to 1000 centipoises can be used, i.e. 10 centipoise is ethylene glycol, i.e. from practical point of view 1000 centipoise is glycerol. Accordingly, the jet of aerosol enters the print head, here it is focused by a jet of air and as a result, an aerosol jet containing a solvent and metal particles with a diameter of 10 microns is obtained at the output. The jet retains parallelism at a distance of up to 10 mm. Respectively, can be printed in a non-contact manner, which is important when using thin Si₂SiO₄ membranes and ceramic ones. The ink was made in AkKo Lab, based on silver, gold and platinum. We used platinum, platinum particles in them ranging in size from 3 to 8 nm, solvent - ethylene glycol.

These inks are a suspension of platinum particles, they are not granulated, so they can be used in both inkjet and aerosol printing.

As a basis for our sensors, we used two types of materials. These are films of thin 12 micron aluminum oxide, which was obtained by anodic oxidation of an aluminum metal, with an area of 40×60 mm (thick film technology standard). It is sturdy, it can be put on two supports - it does not collapse under the influence of its own weight. It is easy to process the film, i.e. it is possible to make such structures of a cantilever type, the cat is made understandable for what: it is necessary to heat up to a high temperature the working part of this sensor - the tip of this triangle - so as to obtain the smallest dissipated power. Those heat the working part to a high temperature so that the power spent on it is as low as possible. Therefore, in order to limit the heat sink for this material, a cantilever structure with a heater at the tip of this triangle was used.

The structure of the alumina film has a porous structure, as usual for anodic aluminum; but because the characteristic dimensions of our heaters are units and tens of microns, and the dimensions of these pores are tens and hundreds of nm, this strongly does not hinder us. And at the same time greatly reduces the thermal conductivity of this material in the lateral direction. The thermal conductivity of the film is of the order of 1 W/m·K, in contrast to 20-24 for bulk aluminum oxide. This structure was printed here in AkKo Lab. Received a cantilever type heater, with a laser this triangle is cut so as to form a structure with an end portion heated to an operating temperature of 450°C. The dependence of power on temperature shows that at 450°C we consume about 65 milliwatts, which is quite comparable to the power typical for silicon MEMS devices, which have a power of about 50 milliwatts. Therefore, this technology proves to be quite competitive in comparison with the technologies of silicon MEMS.

The same microheater was printed with an aerosol seal. The differences are as follows. For

Dimatix printer it is difficult to draw smooth curves with a distance between them of the order of 100 microns. In our case, the distance between the lines at the end of the heater is 300 microns. For the Dimatix, a curve with a radius of 100-150 microns is difficult to draw. Aerosol printing allows this, so you can make such a heater. The width of the aerosol line, which is fairly well resolved, is about 40 microns.

The second material that was used to make these microheaters - so-called LTCC, i.e. this is glass ceramics with a sintering temperature of about 850°C. We ordered thin membranes from this LTCC ceramics, because the ceramic that is commercially available, 100 microns thick, is a very thick, very large heat sink. So a 100 micron ceramic was used, A thin film of the same LTCC ceramics was pressed over the aperture, 30 microns thick. On this membrane - the same structure and the upper material was removed by the laser. The result was a suspended structure in the air, lines 50 microns thick, and a platinum coating thickness of about 1 micron. The thermal characteristics of LTCC ceramics turned out to be worse than aluminum oxide, at a necessary temperature, they had a power of about 150 milliwatts. And it was suspected that the heat dissipation is determined by the thermal conductivity of the ceramic and the thermal conductivity of platinum, and at thicknesses that differ by a factor of 2, the characteristics were virtually identical. I.e. the main heatsink goes on LTCC ceramics, cheap and convenient for use, although the characteristics are somewhat worse than that of aluminum oxide.

So, the microsensor is an aerosol-drawn platinum ink heater, mounted in the TO-8 casing, the window was cut out with a laser, the entire upper material was removed and a drop of a gas-sensitive standard SnO₂/Pd-tin dioxide doped with palladium was applied to the tip with the same technology. Within 250 milliseconds, the heater reaches the desired temperature of 450°C. Accordingly, cooling also occurs quickly.

The sensor should only be heated for the duration of measuring the presence of methane. I.e. heat it for 250 milliseconds to 450°C, measure the response of the sensor, which depends on the concentration of methane and some time to wait. According to GOST (Russian National Standard), it is necessary to carry out measurements at least once every 20 seconds. Accordingly, the duty cycle is of the order of a hundred. And if the power required to heat the operating temperature is 70 milliwatts, then the power can be reduced by a factor of 100. This already becomes quite acceptable for portable devices such as cell phones, i.e. the average power is less than a milliwatt.

A smart module (smart sensor unit) has also been installed, which has a mounted controller on the board, which controls the heating of this sensor, which measures the resistance of the sensitive layer. All sensors have an inherent drawback - sensitivity to water, to moisture of air. Therefore, on the same board, a humidity sensor is also mounted. It makes it possible to compensate for the departure of the sensor characteristics with varying humidity of the ambient air. All parts of the sensor are modular, they can be removed and calibrated in the laboratory.

The last task is to determine the quality of the gas. In Europe, the gas they buy from us, in winter, when it is cold and the gas consumption increases, it is mixed with nitrogen. As a result, in the gas that enters the kitchen, nitrogen is up to 40%. And under the new law in the European Union it is required to determine not only the gas consumption in cubic meters, but also its quality. The simplest way to determine the quality of a gas is to determine its thermal conductivity. The power required to maintain a constant temperature of the sensor heater is linearly dependent on the methane concentration in the gas mixture (CH₄-N₂). This is determined by the developed sensor on the LTCC ceramic.

Thus, it is shown that the use of aerosol and inkjet printing on a thin aluminum membrane

made by anodic oxidation of aluminum foil allows the production of microcircuits compatible with Si MEMS properties.

The combination of thin alumina membranes with additive technology of application of a functional element makes it possible to produce gas sensors with high operating temperature ($>600^{\circ}\text{C}$) and process temperature ($>1000^{\circ}\text{C}$).

The proposed approach allows to save precious metals used for the formation of functional elements, and allows the manufacture of sensors on relatively simple equipment.

This approach is promising for medium-scale production of sensors. The existing aerosol printer is sufficient to produce ~ 2000 chip sensors per hour.

13. CONCLUSION

Sergey P. Gubin and speakers in conclusion Albert G. Nasibulin, Irina V. Antonova and Viktor A. Bykov noted the high level and extraordinary usefulness of the carried out seminar. The general opinion of its participants is that the continuation of the seminar is super-urgent.

REFERENCES

1. Buslaeva EY. Grafenika. Russian Seminar S.P. Gubina (Moscow). *Radioelektronika. Nanosistemy. Informatsionnye Tekhnologii (RENSIT)*, 2011-2017 (in Russ.).
2. Moisala A, Nasibulin AG, Brown DP, Jiang H, Kiriachchev L, Kauppinen EI. Single-walled carbon nanotube synthesis using ferrocene and iron pentacarbonyl in a laminar flow reactor. *Chem.Eng.Sci*, 2006, 61(13):4393-4402.
3. Antonova IV, Kotin IA, Kurkina II, Ivanov AI, Yakimchuk EA, Nebogatikova NA, Vdovin VI, Gutakovskii AK, Soots RA. Graphene/Fluorinated Graphene Systems for a Wide Spectrum of Electronics Application. *Journal of Material Sciences & Engineering*, 2017, 6(5):1000379. doi: 10.4172/2169-0022.1000379.

OBJECT-ORIENTED LOGIC PROGRAMMING OF 3D INTELLIGENT VIDEO SURVEILLANCE SYSTEMS: THE PROBLEM STATEMENT

^{1,2}Alexei A. Morozov, ¹Olga S. Sushkova, ¹Alexander F. Polupanov

¹Kotel'nikov Institute of Radioengineering and Electronics of RAS, <http://www.cplire.ru>
Moscow 125009, Russian Federation

²Moscow State University of Psychology & Education, <http://www.mgppu.ru>
Moscow 107045, Russian Federation

morozov@cplire.ru, o.sushkova@mail.ru, sashap55@mail.ru

Abstract. An approach to the 3D intelligent video surveillance based on the means of the object-oriented logic programming is proposed. In contrast to the conventional 2D video surveillance, the methods of 3D vision provide reliable recognition of parts of the human body that makes possible a new statement of the problem and efficient practical application of methods of people behaviour analysis in the video surveillance systems. The logic-based approach to the intelligent video surveillance allows easy definition of people complex behaviour in terms of simpler activities and postures. The goal of this work is to implement the advantages of the logic programming approach in the area of 3D intelligent video surveillance.

Keywords: : intelligent video surveillance; 3D vision; object-oriented logic programming; Actor Prolog; Kinect; skeleton; complex event recognition; machine vision; technical vision; Prolog to Java translation

UDC 681.3.06

Bibliography – 61 references

Received 29.11.2017

RENSIT, 2017, 9(2):205-214

DOI: 10.17725/rensit.2017.09.205

CONTENTS

1. INTRODUCTION (205)
 2. THE OBJECT-ORIENTED LOGIC PROGRAMMING OF THE INTELLIGENT VIDEO SURVEILLANCE SYSTEMS (207)
 3. AN EXAMPLE OF LOGICAL INFERENCE ON 3D DATA (208)
 4. CONCLUSION (210)
- REFERENCES (211)

1. INTRODUCTION

The 3D video surveillance term has different meanings in research papers:

1. Initially, this term was associated with advanced video surveillance systems supporting real-time 3D visualization of indoor environment, buildings, and people to be monitored, as well as application of virtual and augmented reality technologies in the video surveillance [1]–[4].
2. This term could be associated also with so-called 3D approaches to motion recovery from 2D images [5].

1. Nowadays, this term could be associated with using 3D/2.5D data acquisition equipment [6] like time-of-flight (ToF) cameras, structured light sensors, stereo cameras, laser scanners (LiDARs) [7], and Flash Ladars [8] in video surveillance.

Availability of 3D data acquisition equipment leads to considerable progress in video surveillance related research areas such as background subtraction and tracking people [9], [10], person identification [11], [12], face recognition [13], posture recognition [14], [15], gesture recognition [16], people counting [17], human activity recognition [18], etc. because the use of the 3D/2.5D data makes possible to solve many complicated problems of computer vision caused by the presence of shadows, variations in illumination, view-point changes, cluttered background, and occlusions. And a more important point is in that this technological advance enables progress in solving complex intelligent video surveillance problems [19]

like human-human interaction recognition and prediction [20], abnormal event detection for healthcare systems [21]-[23], unusual events detection [24], the behaviour of customers [25], monitoring of people with disabilities [26], [27], aggressive behaviour and anger detection [28], gait recognition [29] and biometric surveillance [30], and analyzing the human motion to aid clinical decision making [31], [32].

In contrast to the conventional 2D video surveillance, the methods of 3D vision provide reliable recognition of the parts of the human body that makes possible a new statement of the problem and efficient practical application of methods of people behaviour analysis in the video surveillance systems. According to [33], people behaviour is a kind of activity which is a response to some stimuli (internal, external, conscious, or unconscious). For example, such interactions of people as a friendly handshake, a fight, the stealing of a suitcase from another person, etc. could be forms of behaviour. Analysis of the behaviour requires information about the context and other factors influencing it [33]. This information can include video scene geometry, place and presence of objects, time constraints, etc. Thus, the availability of exact information about the co-ordinates of the parts of the body and scene geometry provided by means of the 3D vision is a key to the automation of people behaviour analysis, recognition, and understanding.

Mathematical logic and logic programming were recognized as convenient means for video scene context description and analysis. The idea of the logic programming based approach to the people behaviour analysis is in usage of logical rules for description and analysis of people activities. Knowledge about the human body structure, object properties, time constraints, and scene geometry is encoded in the form of the rules in a logic language and is applied to the output data of some low-level procedures of detection of people and objects.

This idea was developed in the framework of the conventional 2D intelligent video surveillance, and there are a lot of studies based on it. The usage of temporal logic programs in the W⁴ real-time system for representation of actions and analysis of people movements was reported in [34]. The VidMAP video surveillance system that combines real-time computer vision algorithms with the Prolog-based logic programming had been announced in [35]. Later this research group has proposed an extension of the predicate logic with the bilattice formalism that permits processing of uncertainty in the reasoning about the video scenes [36]. The VERSA general purpose framework for defining and recognizing events in live or recorded surveillance video streams was described in [37]. The VERSA system is based on SWI-Prolog. A real-time complex audio-video event detection based on the Answer Set Programming approach was proposed in [38]. Heuristic rules based on a temporal logic are used for describing semantics of video scenes in [39]. A system [40] was designed for recognition of so-called long-term activities (such as "fight" or "meeting") consisting of sequences of short-term activities (such as "walking", "running", "active movement on the spot", "standstill", and "sharp movements") using a logic programming implementation of the Event Calculus. Later this approach was extended to handle the uncertainty that occurs in human activity recognition [41]. The ProbLog probabilistic logic language was used for this purpose. A Prolog-based video surveillance framework for robust detecting abandoned objects was described in [42]. It is believed that the system automatically identifies interrelations between the observed people in order to draw a conclusion about who exactly owns the observed objects, and thus reduce the probability of a false alarm.

Curiously there are not so many papers that utilize logic programming for 3D video data processing. The method of recognition of

long-term activities [40] was adapted [26] for processing the data collected with the help of Kinect. The monitoring system is intended for the analysis of the behaviour of a person in a support room. As reported in [26], the skeleton data were not used for the analysis of long-term activities though the author calculates so-called Activity Level coefficient on the base of the average displacement of all tracked and inferred joints of the skeleton. The probabilistic approach to the long-term activity recognition [41] was adapted to the development of a distributed monitoring system [43] that provides health-care assistance in a smarthome setting. A reasoning engine based on the Description Logics (DL) formalism was used for Kinect-based posture and gesture recognition [44]. Prolog rules were used in the RoboSherlock system [45] to distinguish between actions such as "take", "put", "fill", "push". The logical inference takes into account context information about the properties of the objects. For example, to recognize the "fill" action, it is necessary to know that the object manipulated by a person is a container, food, or an ingredient [45].

The logic-based approach to the intelligent video surveillance has the following obvious advantages [26]:

1. One can easily incorporate domain knowledge into the recognition process.
2. Reasoning about the behaviour of people can be very difficult, but for the developer of the system of intelligent video surveillance, it always remains fundamentally understandable.
3. One can easily define a complex activity in terms of simpler activities.

Our goal is to implement these advantages of the logic approach in the area of the 3D intelligent video surveillance by means of the object-oriented logic programming.

2. THE OBJECT-ORIENTED LOGIC PROGRAMMING OF THE INTELLIGENT VIDEO SURVEILLANCE SYSTEMS

The method of the object-oriented logic programming of the intelligent video surveillance systems was developed in [46]-[52]. The distinctive features of the method are usage of the Actor Prolog object-oriented logic language [53]-[55] and translation of the logic programs of intelligent video surveillance to the Java language [47], [56]. In Actor Prolog the text of a logic program consists of separate classes [53]. Parallel processes represent a kind of instances of classes [54]. The object-oriented means of the logic language allow one to split a program to interacting parallel processes that implement various stages of image processing and scene analysis while translation to the Java language provides a high performance sufficient for analyzing real-time video, as well as reliability and stability of the work of the intelligent video surveillance software.

A conventional approach to recognition of human activity includes low-level and high-level stages of the video processing. In the case of the 2D video surveillance, the low-level stage includes background subtraction of a video image, detection of people and cars in the video image, construction of the trajectories of moving objects, evaluation of the velocities of the objects, etc. The high-level stage includes logical analysis of graphs of the trajectories that are supplied by the low-level analysis algorithms and displaying the results on the screen [50], [51]. The low-level stage of the video processing is implemented in Java [57] in special built-in classes of Actor Prolog.

Since the 2D video surveillance cannot provide a stable recognition of human body parts in most real-world applications, the graphs are used for describing trajectories of blobs (separated areas of a foreground image). The graphs include information about the coordinates and the velocities of the blobs, as

well as a set of statistical metrics describing the regularity of the motion [48]. The blob motion statistics is collected by the low-level analysis procedures and is used for discrimination of running people, people riding bicycles, and cars in the video scene. Usually simple fuzzy inference is implemented for this purpose on the base of the statistical metrics and standard arithmetical predicates of the logic language.

In the case of the 3D video surveillance, the goals of the low-level video analysis are essentially different. For instance, the standard software of the Kinect 2 time-of-flight camera can provide a ready for use foreground blobs, as well as up to six skeletons of people to be monitored [6], [18], [19], [58]-[61]. Thus, the minimal pre-processing of the data can include just a conversion of the images of the skeletons into the terms of the logic language. The high-level stage of the video data processing can be implemented in accordance with the former principles but the information about the video scene is essentially more complete, that gives an opportunity to infer much more of logical consequences on the semantics of the video scene.

3. AN EXAMPLE OF LOGICAL INFERENCE ON 3D DATA

Let us consider a simple logic program that analyses 3D data collected using the Kinect 2 ToF camera.

The data include depth maps and images of skeletons of people, but the program has to analyze the images of the skeletons only and the depth maps are to be used only for the visualization of the video scene. Each skeleton contains 25 joints of various statuses (See **Fig. 1**). The statuses of joints of skeleton can be the following:

1. Tracked – the corresponding part of the body is directly observed by the camera.
2. Inferred – the position of the joint is a hypothetical one.
3. Unknown – the device has no information about this joint.

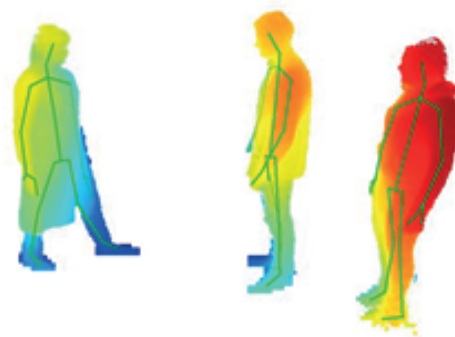


Fig. 1. The images of skeletons and depth maps are the input data of the logic program. The depth maps are indicated by colours.

Thus, the following set of domains (data types) can be defined in Actor Prolog to describe the data structures to be processed:

DOMAINS:

Skeletons = Skeleton*.

The Skeletons type is a list of elements of the Skeleton type.

```
Skeleton = {
    identifier: INTEGER,
    head: SkeletonJoint,
    spine: SkeletonSpine,
    left_arm: SkeletonArm,
    right_arm: SkeletonArm,
    left_leg: SkeletonLeg,
    right_leg: SkeletonLeg
}.
```

The Skeleton type is an underdetermined set [53] of Actor Prolog. The names of the elements of the skeleton as well as the names of corresponding types are obvious:

```
SkeletonSpine = {
    neck: SkeletonJoint,
    shoulder: SkeletonJoint,
    mid: SkeletonJoint,
    base: SkeletonJoint
}.
```

```
SkeletonArm = {
    shoulder: SkeletonJoint,
    elbow: SkeletonJoint,
    wrist: SkeletonJoint,
    hand: SkeletonJoint,
    tip: SkeletonJoint,
    thumb: SkeletonJoint
}.
```

```
SkeletonLeg = {
    hip: SkeletonJoint,
    knee: SkeletonJoint,
    ankle: SkeletonJoint,
    foot: SkeletonJoint
}.
SkeletonJoint = {
    status: SkeletonJointStatus,
    position: VertexPosition3D,
    orientation: JointOrientation3D
}.
```

The status of a joint is a symbol. Each joint is characterized by a position in 3D space, i.e. by three numbers, by orientation, i.e. by four numbers, and by two pairs of 2D co-ordinates that correspond to this joint and are obtained from the infrared and colour images:

```
SkeletonJointStatus =
    'TRACKED'; 'INFERRED'; 'UNKNOWN'.
VertexPosition3D = {
    point: Point3D,
    velocity: Point3D,
    acceleration: Point3D,
    mapping1: Point2D,
    mapping2: Point2D
}.
JointOrientation3D = q(
    Numerical,
    Numerical,
    Numerical,
    Numerical).
```

```
Point3D = p(Numerical, Numerical, Numerical).
Point2D = p(Numerical, Numerical).
```

Suppose that images of skeletons are transferred from the device in real time. Let us declare a set of predicates analyzing the 3D data:

```
PREDICATES:
imperative:
analyse_skeletons(Skeletons) - (i);
nondeterm:
a_hand_of_a_person
    (Skeletons, INTEGER, VertexPosition3D)
    - (i, o, o);
determ:
is_near_a_head_of_a_colleague
    (Skeletons, INTEGER, VertexPosition3D)
    - (i, i, i);
```

The `analyse_skeletons` predicate checks whether there are at least two persons in the video scene and one person punches in the face another person. If there are such persons, the predicate outputs a message in the screen (see **Fig. 2**). Here is the definition of the predicate:

```
CLAUSES:
analyse_skeletons(S):-
    a_hand_of_a_person(S, Id, P),
    is_near_a_head_of_a_colleague(S, Id, P), !,
    graphic_window ? draw_text(
        0.93, 0.08,
        "A punch in the face is detected!").
analyse_skeletons(_).
```

The `a_hand_of_a_person` predicate is nondeterministic. This predicate returns co-ordinates of hands of persons recognized in the scene. Note, that in the Actor Prolog language, the `==` operator corresponds to the `=` ordinary unification of the standard Prolog.

```
a_hand_of_a_person([S|_], Id, P):-
    S == {
        identifier: Id,
        left_arm: {
            hand: {
                status: 'TRACKED',
                position: P|_
            }
        }
    }|_.
a_hand_of_a_person
    ([S|_], Id, P):-
    S == {
        identifier: Id,
        right_arm: {
            hand: {
                status: 'TRACKED',
                position: P|_
            }
        }
    }.
```

A punch in the face is detected!



Fig. 2. A punch in the face is detected by the logic program.

```

    |_}
    |_}.
a_hand_of_a_person([_|R], Id, P) :-
    a_hand_of_a_person(R, Id, P).

```

The following definition is used for the detection of the punch in the face. Execution of the `is_near_a_head_of_a_colleague` predicate succeeds, if given 3D coordinates of some person's hand are close enough to the coordinates of the head of another person. The predicate checks whether the person punches in the face of another person, but not in his own face. For brevity, the velocity of the movement of the hand and the duration of the contact are not taken into consideration, but in a real intelligent visual surveillance application these attributes are to be checked to provide acceptable specificity of the recognition procedure.

```

is_near_a_head_of_a_colleague
    ([S|_], Id1, P1) :-
    S == {
        identifier:Id2,
        head:{
            status:'TRACKED',
            position:P2|_}
        |_},
    Id1 <> Id2,
    is_near(P1, P2), !.
is_near_a_head_of_a_colleague
    ([S|_], Id1, P1) :-
    S == {
        identifier:Id2,
        head:{
            status:'TRACKED',
            position:P2|_}
        |_},
    Id1 <> Id2,
    is_near(P1, P2), !.
is_near_a_head_of_a_colleague([_|R], Id, P) :-
    is_near_a_head_of_a_colleague(R, Id, P).

```

The `is_near` predicate is auxiliary. It checks whether the distance between the given co-ordinates is small enough. The predicate is defined using the built-in arithmetical predicates of Actor Prolog:

```

is_near({point:p(X1, Y1, Z1) |_},
        {point:p(X2, Y2, Z2) |_}) :-
    Delta == ?sqrt(
        ?power(X1-X2, 2) +
        ?power(Y1-Y2, 2) +
        ?power(Z1-Z2, 2)),
    Delta < 0.15, !.

```

For brevity, predicates implementing the data transferring from the outer world into the program are not considered here. One can find a detailed example of this kind in [50]. The `analyse_skeletons` predicate is to be called from time to time in the logic program to analyze images of skeletons recognized in 3D video frames transferred from the outside.

Note that the key point of this example is not recognition of the punch in the face (or recognition of a handshaking) that is a simple problem, but in that much more complex logical formulae can be automatically checked in the same way. For example, a logic program can check whether a person shakes hands with all people in the room or not, i.e. a program can make some conclusions on the social status of the person or social relations between all the people in the room. The same technique can be used to solve urgent problems of intelligent visual surveillance, such as recognizing armed attacks, demonstrating threatening poses, robberies, etc.

4. CONCLUSION

A method of the logic object-oriented programming for processing the data obtained from the equipment for 3D data acquisition in the intelligent video surveillance systems was developed. The Actor Prolog object-oriented logic language and translation of the logic programs of intelligent video surveillance to the Java language were used. The object-oriented means of the Actor Prolog logic language allow us to split a program into interacting parallel processes that implement various stages of image processing and scene analysis while translation to the Java language provides a high performance sufficient for analyzing real-time video, as well

as reliability and stability of the work of the intelligent video surveillance software. One can download the software for free from the Web Site [52].

The application of methods of the logic object-oriented programming for 3D data processing gives exciting prospects in the area of intelligent video surveillance. Progress in this research area can be achieved by the development of efficient low-level 3D data processing algorithms, logic programming languages and systems for general purpose, and advanced logical methods of 3D data processing.

ACKNOWLEDGMENT

Authors are grateful to Ivan A. Kershner and Renata A. Tolmatcheva for the help in the preparation of 3D video samples and Angelos Barmpoutis for his J4K [59] library that was used for the data collection.

This research is supported by the Russian Foundation for Basic Research, grant No. 16-29-09626-ofi_m.

REFERENCES

1. Sebe IO, Hu J, You S, Neumann U. 3D video surveillance with augmented virtual environments *First ACM SIGMM international workshop on Video surveillance. ACM*, 2003:107-112.
2. Ott R, Gutiérrez M, Thalmann D, Vexo F. Advanced virtual reality technologies for surveillance and security applications. *International Conference on Virtual Reality Continuum and Its Applications. ACM*, 2006:163-170.
3. Barnum P, Sheikh Y, Datta A, Kanade T. Dynamic seethroughs: Synthesizing hidden views of moving objects. *Mixed and Augmented Reality (ISMAR 2009). IEEE*, 2009:111-114.
4. DeCamp P, Shaw G, Kubat R, Roy D. An immersive system for browsing and visualizing surveillance video. *International Conference on Multimedia. ACM*, 2010:371-380.
5. Gavrilu DM. The visual analysis of human movement: A survey. *Computer Vision and Image Understanding*, 1999, 73(1):82-98.
6. Chen L, Wei H, Ferryman J. A survey of human motion analysis using depth imagery. *Pattern Recognition Letters*, 2013, 34(15):1995-2006.
7. Benedek C. 3D people surveillance on range data sequences of a rotating Lidar. *Pattern Recognition Letters*, 2014, 50:149-158.
8. Stettner R, Bailey H, Silverman S. Three dimensional Flash LADAR focal planes and time dependent imaging. *International Journal of High Speed Electronics and Systems*, 2008, 18(2):401-406.
9. Hansen DW, Hansen MS, Kirschmeyer M et al. Cluster tracking with time-of-flight cameras. *Computer Vision and Pattern Recognition Workshops (CVPRW'08), IEEE*, 2008:1-6.
10. Silvestre D. Video surveillance using a time-of-flight camera. *Master's thesis, Informatics and Mathematical Modelling*, Technical University of Denmark, 2007.
11. Satta R, Pala F, Fumera G, Roli F. Real-time appearance-based person re-identification over multiple Kinect™ cameras. *VISAPP*, 2013:407-410.
12. Sinha A, Chakravarty K, Bhowmick B. Person identification using skeleton information from Kinect. *The Sixth International Conference on Advances in Computer-Human Interactions (ACHI 2013)*, 2013:101-108.
13. Krishnan P, Naveen S. RGB-D face recognition system verification using Kinect and FRAV3D databases. *Procedia Computer Science*, 2015, 46:1653-1660.
14. Diraco G, Leone A, Siciliano P. Human posture recognition with a time-of-flight 3D sensor for in-home applications. *Expert Systems with Applications*, 2013, 40(2):744-751.
15. Ibañez R, Soria Á, Teyseyre A, Campo M. Easy gesture recognition for Kinect. *Advances in Engineering Software*, 2014, 76:171-180.
16. Raheja J, Minhas M, Prashanth D et al. Robust gesture recognition using Kinect: A

- comparison between DTW and HMM. *Optik International Journal for Light and Electron Optics*, 2015, 126(11):1098-1104.
17. Hsieh C-T, Wang H-C, Wu Y-K et al. A Kinect-based people-flow counting system. *Intelligent Signal Processing and Communication Systems (ISPACS 2012)*. IEEE, 2012:146-150.
 18. Aggarwal JK, Xia L. Human activity recognition from 3D data: A review. *Pattern Recognition Letters*, 2014, 48:70-80.
 19. Lun R, Zhao W. A survey of applications and human motion recognition with Microsoft Kinect. *International Journal of Pattern Recognition and Artificial Intelligence*, 2015, 29(5).
 20. Alazrai R, Mowafi Y, Lee C. Anatomical-plane-based representation for human-human interactions analysis. *Pattern Recognition*, 2015, 48(8):2346-2363.
 21. Rougier C, Auvinet E, Rousseau J et al. Fall detection from depth map video sequences. *International Conference on Smart Homes and Health Telematics*. Springer, 2011:121-128.
 22. Lee Y-S, Chung W-Y. Visual sensor based abnormal event detection with moving shadow removal in home healthcare applications. *Sensors*, 2012, 12(1):573-584.
 23. Mastorakis G, Makris D. Fall detection system using Kinect's infrared sensor. *Journal of Real-Time Image Processing*, 2014, 9(4):635-646.
 24. Wang C, Liu H. Unusual events detection based on multi-dictionary sparse representation using Kinect. *Intern. Conf. on Image Processing, IEEE*, 2013:2968-2972.
 25. Popa M, Koc AK, Rothkrantz LJ et al. Kinect sensing of shopping related actions. *International Joint Conference on Ambient Intelligence*, Springer, 2011:91-100.
 26. Johanna M. Recognizing activities with the Kinect. A logic-based approach for the support room. *Master's thesis, Radboud University Nijmegen*, 2013.
 27. Lau TB, Ong AC, Putra FA. Non-invasive monitoring of people with disabilities via motion detection. *International Journal of Signal Processing Systems*, 2014, 2(1):37-41.
 28. Patwardhan A, Knapp G. Aggressive actions and anger detection from multiple modalities using Kinect. // arXiv preprint arXiv:1607.01076. – 2016.
 29. Preis J, Kessel M, Werner M, Linnhoff-Popien C. Gait recognition with Kinect. *International Workshop on Kinect in Pervasive Computing*. Newcastle, UK, 2012.
 30. Savage R, Clarke N, Li F. Multimodal biometric surveillance using a Kinect sensor. *Proceedings of the 12th annual security conference*, Las Vegas, USA, 2013.
 31. Chaaraoui AA, Padilla-López JR, Flórez-Revuelta F. Abnormal gait detection with RGB-D devices using joint motion history features. *Automatic Face and Gesture Recognition (FG)*, IEEE, 2015,7:1-6.
 32. Leightley D, Yap MH, Hewitt BM, McPhee JS. Sensing behaviour using the Kinect: Identifying characteristic features of instability and poor performance during challenging balancing tasks. *Measuring Behavior*, 2016.
 33. Borges PVK, Conci N, Cavallaro A. Video-based human behavior understanding: A survey. *IEEE Transactions on Circuits and Systems for Video Technology*, 2013, 23:1993-2008.
 34. Haritaoglu I, Harwood D, Davis L. W⁴: Who? When? Where? What? A real time system for detecting and tracking people. *FG 1998*, Nara, Japan, 1998:222-227.
 35. Shet V, Harwood D, Davis L. VidMAP: Video monitoring of activity with Prolog. *AVSS-2005, IEEE*, 2005:224-229.
 36. Shet V, Singh M, Bahlmann C et al. Predicate logic based image grammars for complex pattern recognition. *International Journal of Computer Vision*, 2011, 93(2):141-161.
 37. O'Hara S. VERSA—video event recognition for surveillance applications. *M.S. thesis. University of Nebraska at Omaha*, 2008.
 38. Machot F, Kyamakya K, Dieber B, Rinner B. Real time complex event detection for resource-limited multimedia sensor networks. *AMMCSS-2011*, 2011:468-473.

39. Lao W, Han J, de With PHN. Flexible human behavior analysis framework for video surveillance applications. *International Journal of Digital Multimedia Broadcasting*, 2010, Article ID 920121:1-9.
40. Artikis A, Sergot M, Paliouras G. A logic programming approach to activity recognition. *International Workshop on Events in Multimedia (EiMM 2010)*, NY, USA. ACM, 2010:3-8.
41. Skarlatidis A, Artikis A, Filippou J, Paliouras G. A probabilistic logic programming event calculus. *Theory and Practice of Logic Programming*, 2014, 9:1-33.
42. Ferryman J, Hogg D, Sochman J et al. Robust abandoned object detection integrating wide area visual surveillance and social context. *Pattern Recognition Letters*, 2013, 34(7):789-798.
43. Katzouris N, Artikis A, Paliouras G. Event recognition for unobtrusive assisted living. *Hellenic Conference on Artificial Intelligence*, Springer, 2014:475-488.
44. Ruta M, Scioscia F, Summa MD et al. Semantic matchmaking for Kinect-based posture and gesture recognition. *International Journal of Semantic Computing*, 2014, 8(4):491-514.
45. Worch J-H, Bálint-Benczédi F, Beetz M. Perception for everyday human robot interaction. *KI - Künstliche Intelligenz*, 2016, 30(1):21-27.
46. Morozov AA, Vaish A, Polupanov AF et al. Development of concurrent object-oriented logic programming platform for the intelligent monitoring of anomalous human activities. *International Joint Conference on Biomedical Engineering Systems and Technologies*, Springer, 2015, 511:82-97.
47. Morozov AA, Polupanov AF. Intelligent visual surveillance logic programming: Implementation issues. *CICLOPS-WLPE 2014, ser. Aachener Informatik Berichte no. AIB-2014-09*, T. Ströder & T. Swift eds., RWTH Aachen University, 2014:31-45. <http://aib.informatik.rwth-aachen.de/2014/2014-09.pdf>.
48. Morozov AA, Polupanov AF. Development of the logic programming approach to the intelligent monitoring of anomalous human behaviour. *OGRW2014*, Koblenz, Univ. of Koblenz-Landau, 2015, 5:82-85. https://kola.opus.hbz-nrw.de/files/915/OGRW_2014_Proceedings.pdf.
49. Morozov AA, Sushkova OS, Polupanov AF. An approach to the intelligent monitoring of anomalous human behaviour based on the Actor Prolog object-oriented logic language. *RuleML 2015 DC and Challenge*, Berlin, CEUR, 2015. <http://ceur-ws.org/Vol-1417/paper7.pdf>.
50. Morozov AA. Development of a method for intelligent video monitoring of abnormal behavior of people based on parallel object-oriented logic programming. *Pattern Recognition and Image Analysis*, 2015, 25(3):481-492. <http://www.cplire.ru/Lab144/pria481.pdf>.
51. Morozov AA, Sushkova OS. Real-time analysis of video by means of the Actor Prolog language. *Computer Optics*, 2017; Special issue 3 (November): 97-105. DOI: 10.18287/2412-6179-2016-40-6-947-957.
52. Morozov AA, Sushkova OS. The intelligent visual surveillance logic programming Web Site [Electronic resource], 2017. Access mode: <http://www.fullvision.ru> (29.11.2017).
53. Morozov AA. Actor Prolog: an object-oriented language with the classical declarative semantics. *IDL 1999*, Eds. K. Sagonas, P. Tarau. Paris, France, 1999:39-53. <http://www.cplire.ru/Lab144/paris.pdf>.
54. Morozov AA. Logic object-oriented model of asynchronous concurrent computations. *Pattern Recognition and Image Analysis*, 2003, 13(4):640-649. <http://www.cplire.ru/Lab144/pria640.pdf>.
55. Morozov AA. Operational approach to the modified reasoning, based on the concept of repeated proving and logical actors. *CICLOPS 2007*, Eds. S. Abreu, V. S. Costa.

- Porto, Portugal, 2007:1-15. <http://www.cplire.ru/Lab144/ciclops07.pdf>.
56. Morozov AA, Sushkova OS, Polupanov AF. A translator of Actor Prolog to Java. *RuleML 2015 DC and Challenge*, Eds. N. Bassiliades, P. Fodor, A. Giurca et al. Berlin, CEUR, 2015. <https://www.csw.inf.fu-berlin.de/ruleml2015-ceur>.
57. Morozov AA. A GitHub repository containing source codes of Actor Prolog built-in classes [Electronic resource]. 2017. Access mode: <https://github.com/Morozov2012/actor-prolog-java-library>.
58. Han J, Shao L, Xu D, Shotton J. Enhanced computer vision with Microsoft Kinect sensor: A review. *IEEE Transactions on Cybernetics*, 2013, 43(5):1318-1334.
59. Bampoutis A. Tensor body: Real-time reconstruction of the human body and avatar synthesis from RGB-D. *IEEE Transactions on Cybernetics*, 2013, 43(5):1347-1356.
60. Han F, Reily B, Hoff W, Zhang H. Space-time representation of people based on 3D skeletal data: A review. ArXiv preprint [arXiv:1601.01006v2](https://arxiv.org/abs/1601.01006v2) [cs.CV], 2016.
61. Presti LL, Cascia ML. 3D skeleton-based human action classification: A survey. *Pattern Recognition*, 2016, 53:130-147.

NUMERICAL MODELING OF THE PROCESS OF DETECTION OF KARST CAVITIES IN RAILWAY EMBANKMENTS BY A GRID-CHARACTERISTIC METHOD

¹Vladimir S. Egiyan, ^{1,2}Alena V. Favorskaya, ¹Aram A. Mkrtchyan, ^{1,2}Igor B. Petrov, ^{1,2}Nikolay I. Khokhlov, ^{1,2}Vasiliy I. Golubev

¹Moscow Institute of Physics and Technology, <http://mipt.ru>

Dolgoprudny, Moscow region 141700, Russian Federation

²Scientific Research Institute of System Development of RAS, <https://www.niisi.ru>

Moscow 117218, Russian Federation

vladimir.yeghiyan@phystech.edu, aleanera@yandex.ru, aramaram94@mail.ru, petrov@mipt.ru, k_h@inbox.ru, w.golubev@mail.ru

Abstract. Over the past 160 years, railways are one of the main elements of the top track structure throughout the world. They serve to direct the wheels when they move and directly perceive and transmit pressure to the underlying elements. Despite all the efforts of engineers, karst cavities can form under the rails due to severe operating conditions. One of the priority tasks is the development of methods for their detection in railway embankments by solving a series of direct problems. The purpose of this paper is to study the propagation of elastic waves in a railway embankment. We used a grid-characteristic method on curvilinear structural grids, which makes it possible to efficiently solve the tasks of monitoring the state of the railway embankment and paths, including taking into account the large number of integrity violations, to take into account the dynamic interactions in the system of rolling stock - the path, to obtain a complete wave pattern. A comparative analysis of calculations of a series of calculations with a variable geometry of the computational domain was carried out. Comparison of the propagation processes of elastic waves in the presence and absence of karst inclusions in the soil under the embankment is made, comparison of signals diagnosed in these cases from rails is given.

Keywords: computer simulation, grid-characteristic method, structural hexahedral grids, railway transport safety, karst cavities

UDC 519.63

Bibliography – 10 references

Received 14.11.2017

RENSIT, 2017, 9(2):215-220

DOI: 10.17725/rensit.2017.09.215

CONTENTS

1. INTRODUCTION (215)
 2. MODEL AND METHOD (216)
 3. RESULTS AND DISCUSSION (217)
 4. CONCLUSION (219)
- REFERENCES (219)

1. INTRODUCTION

To solve the real problems of monitoring of the state of rolling stock and tracks it is necessary to take into account the dynamic interactions in the system of the rolling stock - the path, to study the spatial dynamic wave

pattern, to take into account the characteristic properties of the dynamic system of equations of deformable solid body [1]. Currently used methods are approximate and do not allow us to reproduce the complete wave picture of the processes occurring in the structure under consideration. While the study of these processes will make it possible to make diagnostics of the rolling stock and ways more efficient.

Since the system of equations for the mathematical model of the state of a continuous linearly elastic medium [2] is

hyperbolic and a high-precision calculation of wave processes is required, it is optimal to use the grid-characteristic method [3-7].

2. MODEL AND METHOD

In this work the system of linear elasticity is used [2]

$$\rho \partial_t \bar{v} = (\nabla \cdot \sigma)^T, \tag{1}$$

$$\partial_t \sigma = \lambda (\nabla \cdot \bar{v}) \mathbf{I} + \mu (\nabla \otimes \bar{v} + (\nabla \otimes \bar{v})^T). \tag{2}$$

Equation (1) is the local motion equation. Here ρ – material density, \bar{v} – velocity, σ – stress tensor. Equation (2) is related to the Hook’s. Here λ, μ – Lamé parameters.

For numerical solution of system (1), (2) the grid-characteristic method on curvilinear structured meshes was used that allows to build correct numerical algorithms for calculating boundary points and points lying on the interfaces of two media with different Lamé parameters and (or) densities. In 2D case it can be written as

$$\partial_t \bar{q} + \mathbf{A}_1 \partial_{x_1} \bar{q} + \mathbf{A}_2 \partial_{x_2} \bar{q} = 0. \tag{3}$$

In equation (3) \bar{q} denotes vector from 2 components of velocity and 3 components of stress tensor

$$\bar{q} \in \{v_1, v_2, \sigma_{11}, \sigma_{22}, \sigma_{12}\}^T.$$

Initially we split our system be directions into 2 independent systems:

$$\frac{\partial \bar{q}}{\partial t} = \mathbf{A}_j \frac{\partial \bar{q}}{\partial x_j}. \tag{4}$$

Both of them are hyperbolic and can be written as:

$$\frac{\partial \bar{q}}{\partial t} = \mathbf{\Omega}_j^{-1} \mathbf{\Lambda}_j \mathbf{\Omega}_j \frac{\partial \bar{q}}{\partial x_j},$$

$\mathbf{\Omega}_j$ – matrix from Eigen vectors, $\mathbf{\Lambda}_j$ – diagonal matrix from Eigen values. For all directions $\mathbf{\Lambda}$ can be written as (don’t use index j further):

$$\mathbf{\Lambda} = \text{diag}\{c_p, -c_p, c_s, -c_s, 0\},$$

where $c_p = \sqrt{(\lambda + 2\mu) / \rho}$ – P-wave velocity, $c_s = \sqrt{\mu / \rho}$ – S-wave velocity.

Using $\bar{q} = \mathbf{\Omega} \bar{p}$ both systems (4) splits into independent transport equations:

$$\frac{\partial \bar{q}}{\partial t} + \mathbf{\Lambda} \frac{\partial \bar{q}}{\partial x} = 0.$$

Each 1D equations are solved with grid-characteristic or finite-different schemes.

Finally, the solution can be obtained by

$$\bar{q}^{n+1} = \mathbf{\Omega}^{-1} \bar{p}^{n+1}.$$

At the Moscow Institute of Physics and Technology under the supervision of Corresponding Member of the Russian Academy of Sciences Igor B. Petrov a research software was developed that uses the described method. The program implements the use of TVD-difference schemes of the second order of accuracy [8], 15 different limiters. In the calculations, the superbee limiter [9] and grid-characteristic schemes of the 2-4 order of accuracy are mainly used [10]. **Fig. 1** shows a graph of the acceleration of the software when using MPI technology, which indicates a high degree of its parallelization.

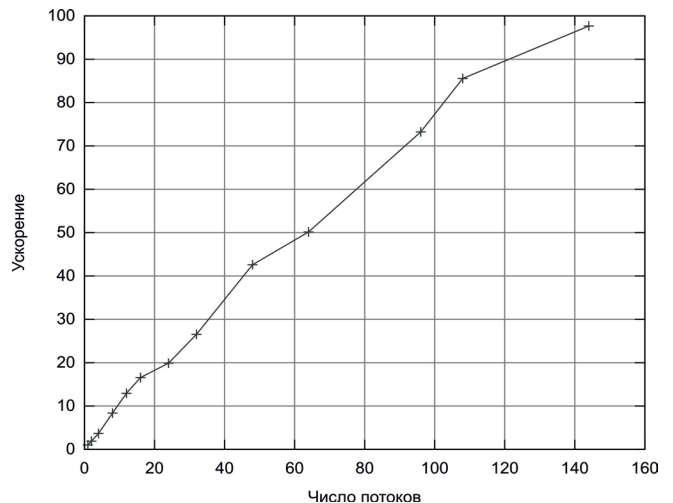


Fig. 1. Computation speedup with MPI and mesh with 64 million nodes.

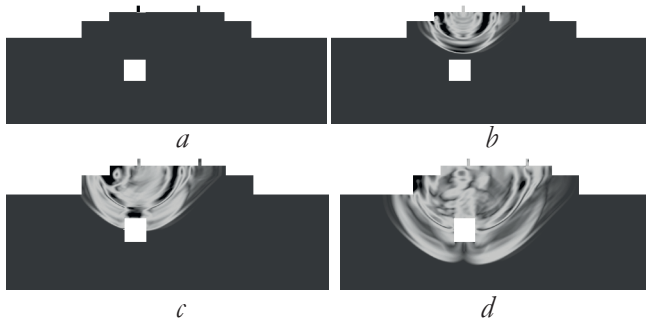


Fig. 2. Wave processes in embankment. a) Initial perturbation, b) Perturbation propagation, c) First seismic response creation, d) Second seismic response creation.

3. RESULTS AND DISCUSSION

Fig. 2 shows the propagation of elastic waves in an embankment with a karst inclusion. Fig. 2a shows the initial perturbation. Fig. 2b shows the further propagation of elastic waves in the rails, embankment and ground. Fig. 2c shows the creation of the first response from the karst inclusion, and Fig. 2d – the second response. In Fig. 2a - 2d gradation of gray shows the velocity modulus. The calculations were carried out by a grid-characteristic method on a grid consisting of 200,000 nodes, the boundaries of the integration region are free, karst inclusion is

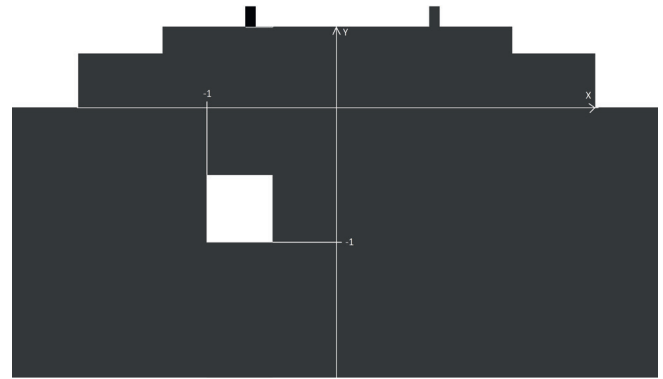


Fig. 3. Embankment with coordinate lines that determine the location of the karst cavities.

also given by a free boundary, the condition of complete adhesion is used at the contact boundaries between the railway embankment and rails.

Figures 4-8 show the dependencies (seismic traces) obtained from the left and right rails for different sizes and locations of the cavities. On all graphs, the black line corresponds to the calculation without karst inclusion, and the gray scale line – with karst inclusions at different places. Fig. 3 shows an embankment with coordinate lines.

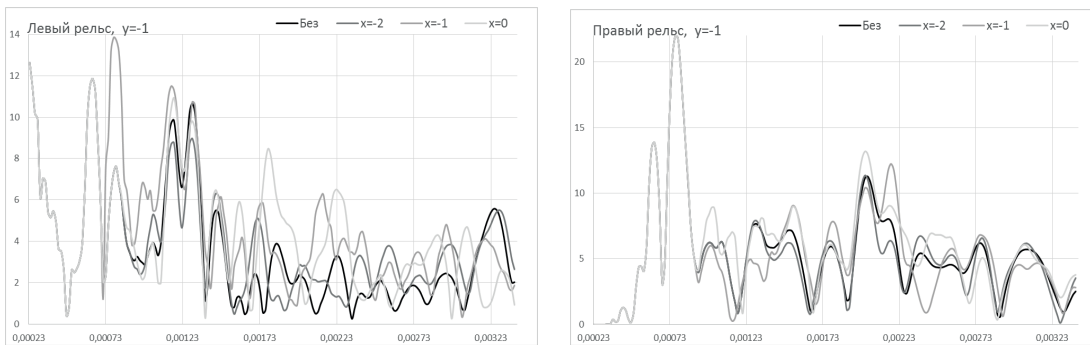


Fig. 4. Functions $v(t)$, cavern size – (0.5×0.5) , depth – $y = -1$.

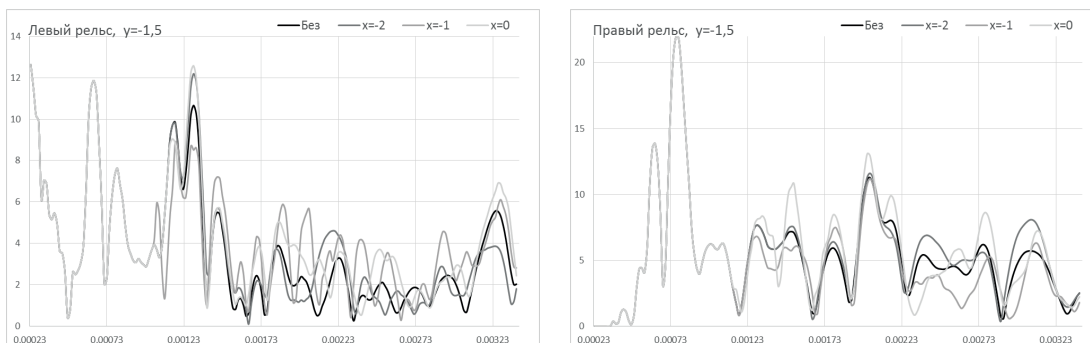


Fig. 5. Functions $v(t)$, cavern size – (0.5×0.5) , depth – $y = -1.5$.

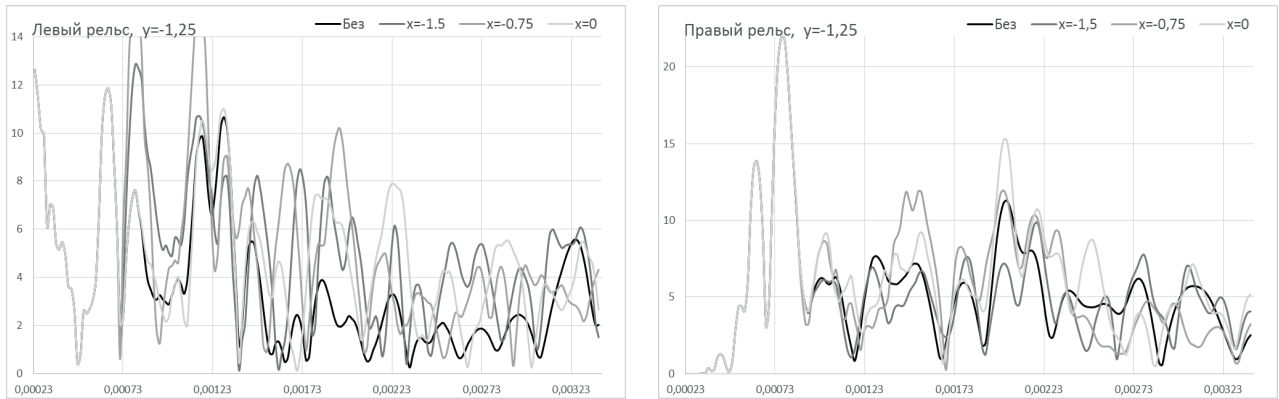


Fig. 6. Functions $v(t)$, cavern size – (0.75×0.75) , depth – $y = -1.25$.

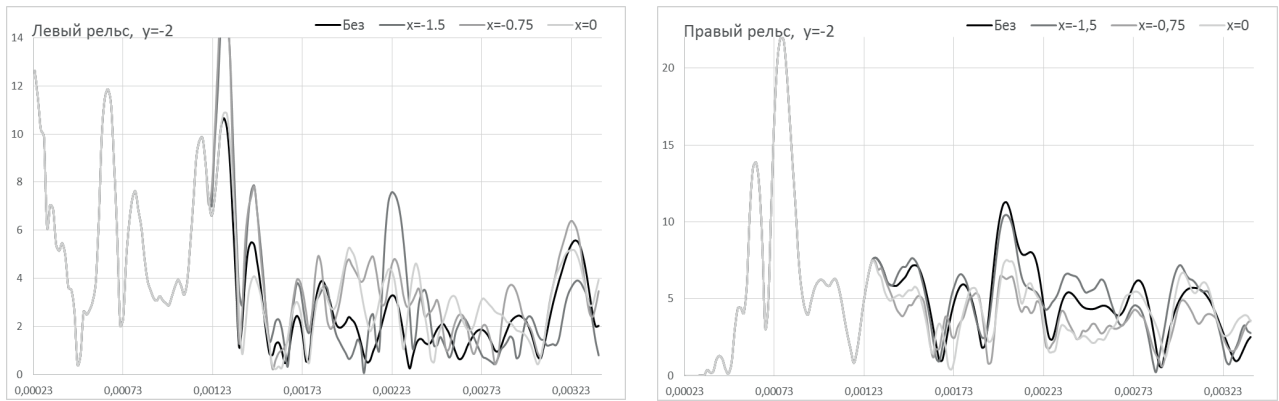


Fig. 7. Functions $v(t)$, cavern size – (0.75×0.75) , depth – $y = -2$.

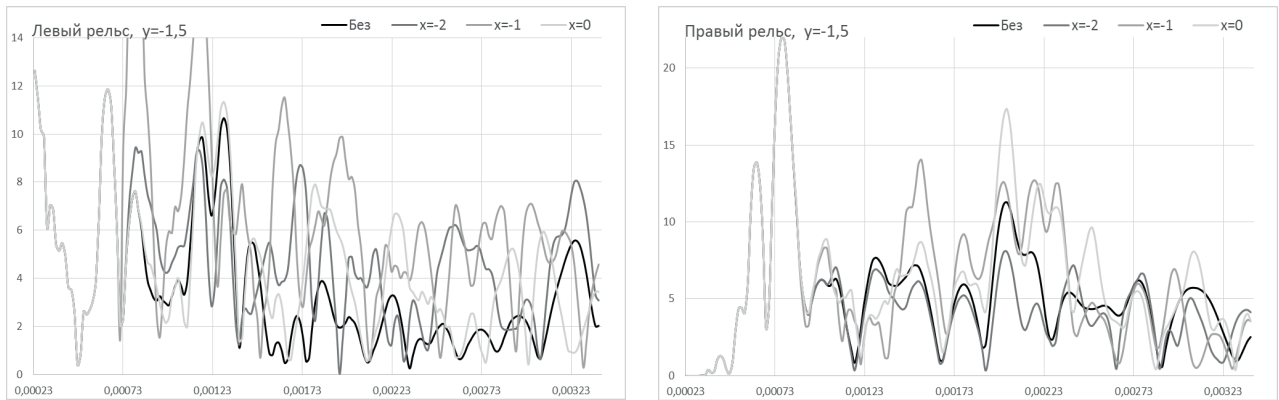


Fig. 8. Functions $v(t)$, cavern size – (1.0×1.0) , depth – $y = -1.5$.

Fig. 4-8 depict dependencies obtained from the left and right rails for three different sizes of the cavity. Fig. 4-5: cavern size 0.5×0.5 , Fig. 6-7: cavern size 0.75×0.75 and Fig. 8: cavern size 1.0×1.0 . On each graph, it is written from which rail the data were measured and the location of the karst cavity (see Fig. 3).

Fig. 4 shows plots in the case of a cavern with a size of 0.5×0.5 and a depth of $y = -1$.

At the beginning all the lines on the graphs are coincide. This means that the wave reflected from the cavern did not reach the rail, and at some point in time the discrepancy between the measurement results with the cavern (lines with gray gradation) and without (black line) is already visible. Comparing the data obtained from the left and right rails, we see that on the left rail the discrepancy begins

earlier than on the right, since the initial disturbance was placed on the left rail.

Similar conclusions can be drawn for **Fig. 5-8**. Comparing the data with the different sizes of the cavern, we see that in the case of large caverns, the lines diverge more than in the case of small caverns, since the reflection line of the wave is longer and therefore the waves are more reflected. Let's compare the data of caverns with different depths under the ground. And we will see that the deeper the cavern lies, the weaker the reflected wave and therefore it is impossible to detect deep caverns. But in this case, there is less likelihood that the cavern will interfere with the movement of the train. And so it is not necessary to detect deep-lying caverns.

Based on the results of measurements, it can be argued that in all cases it is more accurate to locate and determine the location and size of the cavity under the left rail than under the right (initial disturbance of the wave was placed on the left rail).

4. CONCLUSION

In this article we present developed methods for the detection of karst cavities on railway embankments by solving a number of direct problems. A comparative analysis of the calculations obtained by the grid-characteristic method was carried out. Comparison of the propagation of elastic waves in the presence and absence of karst inclusions in the soil under the embankment is made, a comparison of the signals registered in these cases at rails is given. Comparing the results, we see that this method can accurately determine the location and size of the cavity. The further direction of the work is the solution of the inverse problem by the comparison of calculated and experimental data.

The reported study was funded by RFBR and JSC Russian Railways according to the research project № 17-20-01096.

REFERENCES

1. Cannon DF, Edel KO, Grassie SL, Sawley K. Rail defects: an overview. *Fatigue & Fracture of Engineering Materials & Structures*, 2003, 26(10):865-886.
2. Novatskii VK. *Teoriya uprugosti* [Elastic Theory]. Moscow, Mir Publ., 1975, 872 p.
3. Petrov IB, Kholodov AS. Numerical study of some dynamic problems of the mechanics of a deformable rigid body by the mesh-characteristic method. *Zhurnal vychislitel'noy matematiki i matematicheskoy fiziki* [Computational Mathematics and Mathematical Physics], 1984, 24(3):61-73 (in Russ.).
4. Golubev VI, Gilyazutdinov RI, Petrov IB, Khokhlov NI, Vasyukov AV. Simulation of dynamic processes in three-dimensional layered fractured media with the use of the grid-characteristic numerical method. *Journal of Applied Mechanics and Technical Physics*, 2017, 58(3):539-545.
5. Kvasov IE, Pankratov SA, Petrov IB. Numerical simulation of seismic responses in multilayer geologic media by the grid-characteristic method. *Matematicheskoe modelirovanie* [Math Models Comput Simul], 2011, 3(2):196-204 (in Russ.).
6. Petrov IB, Favorskaya AV, Sannikov AV, Kvasov IE. Grid-characteristic method using high-order interpolation on tetrahedral hierarchical meshes with a multiple time step. *Matematicheskoe modelirovanie*, 2013, 5(5):409-415 (in Russ.).
7. Muratov MV, Petrov IB. Estimation of wave responses from subvertical macrofracture systems using a grid

- characteristic method. *Matematicheskoe modelirovanie*, 2013, 5(5):479-491 (in Russ.).
8. Harten A. High resolution schemes for hyperbolic conservation laws. *Journal of Computational Physics*, 1997, 135(2):260-278.
 9. Roe PL. Characteristic-Based Schemes for the Euler Equations. *Annual Review of Fluid Mechanics*, 1986, 18:337-365.
 10. Kholodov AS, Kholodov YA. Monotonicity criteria for difference schemes designed for hyperbolic equations. *Zhurnal vychislitel'noy matematiki i matematicheskoy fiziki*, 2006, 46(9):1560-1588 (in Russ.).

LIGHT DIFFRACTION BY FRACTALS: COMPARISON OF EXPERIMENTAL DATA WITH THE OBTAINED BY NUMERICAL METHODS FOURIER IMAGES OF THE OBJECT PICTURES

Galina V. Arzamastseva, Mikhail G. Evtikhov, Feodor V. Lisovsky, Ekaterina G. Mansvetova

Kotel'nikov Institute of Radioengineering and Electronics, Fryazino Branch, Russian Academy of Sciences, <http://fire.relarn.ru>

Fryazino, Moscow region 141120, Russian Federation

arzamastseva@mail.ru, emg20022002@mail.ru, lisf@df.ru, mansvetova_eg@mail.ru

Abstract. An experimental investigation of diffraction of the collimated light beam (with a wavelength of 0.63 μm) in the zone of Fraunhofer by obtained with computer images of fractals, which are transferred onto a transparent film using an imagesetter with a resolution of 1333 points/cm (3386 dpi) and the spot size of 7.5 μm . Diffraction pattern were visually observed on the screen and recorded using a digital camera and then transferred to the computer for processing. The objects of study were various prefractals of 4th-9th generations: the "classic" (the Sierpinski carpet, a fractal of Vicsek, the Koch snowflake and less known (eg. of L-systems)). Observed in experiments diffraction patterns were compared with digitally obtained ones that is, with the Fourier-images of the prefractal pictures, approximated by a mesh function on a uniform square grid at different values of the used in calculation parameter p , determining the ratio between the ratio of the grid period and the smallest prefractal element size. The relation between the values of the parameters p and the degree of compliance of a digital diffraction patterns to the observed experimentally was determined.

Keywords: light diffraction, mesh function, fractal, Fourier image, digital method, experiment

UDC 51.74; 535.42

Bibliography – 18 references

Received 25.09.2017

RENSIT, 2017, 9(2):221-229

DOI: 10.17725/rensit.2017.09.221

CONTENTS:

1. INTRODUCTION (221)
 2. EXPERIMENTAL CONDITIONS (222)
 3. PROCEDURE FOR FOURIER-IMAGES DETERMINATION OF PREFRACTAL PICTURES (222)
 4. INVESTIGATION RESULTS AND DISCUSSION (223)
 5. CONCLUSION (227)
- REFERENCES (228)

1. INTRODUCTION

Interest in theoretical and experimental study of electromagnetic waves diffraction by flat fractals that emerged at the end

of the last century, was not so much due to epistemological reasons, how many opportunities of practical application. In particular, it was shown that the analysis of the distribution of the diffracted radiation in the zone of Fraunhofer allows quite easy to define the essential characteristics of fractal objects – Hausdorff dimension [1]. It soon became clear that this does not necessarily actually accomplish quite time-consuming experiments on the observation of diffraction and the processing of the obtained results, but rather to obtain a graphics image of a fractal (more precisely, prefractal of high enough generation),

digitize it and continue to use methods of Fourier analysis.

In most cases, to determine the fractal dimension anybody operates in this manner, so the number of works devoted to the study of diffraction itself, is relatively small [2-7]. It is almost not studied the questions remain whether there are differences between real and digital diffraction pattern and what conditions to meet their identity needs to satisfy the procedure for digitizing and processing the pictures of fractals. The aim of this work is to answer these questions.

2. EXPERIMENTAL CONDITIONS

A first and necessary step for the implementation of experiments on the observation of diffraction is the creation of black-and-white raster pictures of the selected prefractions on the computer using specially designed software. Then, the resulting pictures were automatically printed onto a transparent film with imagesetter having resolution of 1333 points/cm (3386 dpi) and the spot size of 7.5 μm . The smallest fractal element was formed from 4-10 points, that is, its linear size was in the range of 30 to 75 microns. The described method of picture forming made it possible to obtain very high contrast, almost unattainable for traditional photography.

In **Fig. 1** the block diagram of experimental setup used for observation of the diffraction pattern forming in the Fraunhofer zone after the passage of the light beam through the transparent film with prefractional picture on its surface

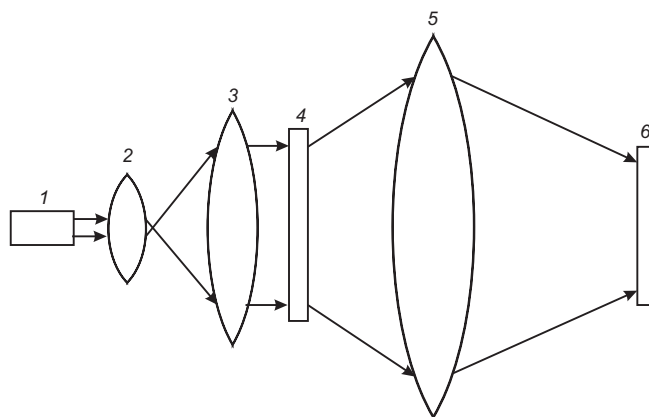


Fig. 1. A block diagram of the optical setup for observing diffraction pattern in the Fraunhofer zone.

is shown. A narrow beam of light with a wavelength of 0.63 microns from a helium-neon laser 1 is expanded and collimated using a system of confocal lenses 2 and 3 to diameter 5 to 8 cm and then directed onto the transparent film 4 with the picture of a fractal object. The lens 5 forms an image of the diffraction pattern in the plane of diffraction, where the screen 6 is mounted. Instead of screen one can use a computer coupled with a digital camera and subject the observed diffraction pattern to the necessary treatment.

3. PROCEDURE FOR FOURIER-IMAGES DETERMINATION OF PREFRACTAL PICTURES

Created with help of computer black-and-white raster pictures of prefractions were approximated by a grid function on a uniform grid with number of nodes $n_1 \times n_2$, where the values n_1 and n_2 were chosen sufficiently large (up to 4096) in order to ensure adequate approximation of the smallest details and to have the opportunity to explore generation of prefractions with high numbers of generations. For thus digitized pictures using fast Fourier

transform one can determine the values of the Fourier component squared modules, i.e. the spectral distribution of intensity I of diffracted radiation in the zone of Fraunhofer. To display the intensity I of the diffraction maxima on the 2D-plane, one can use representation of I values in the form of circles with radius proportional to intensity (or logarithm of it), where coefficient of proportionality is chosen for reasons of optimal demonstrativeness of images; to reach that additional Gaussian blur of circles was also used.

Used in the present work a procedure for determination of fractal object picture Fourier-images (i.e., "digital diffractograms"), previously described and applied to study the fractal-like domain structures in magnetic films [8], later was applied to the real test objects (mono- and bi-periodical domain structures), when it was possible in the visible range of wavelengths to observe directly and photograph the diffraction pattern by the "transmission" mode [9]. Afterwards similar numerical methods have been used for many other fractal objects [10-15].

For all the studied geometric fractals on diffraction patterns, experimentally obtained by optical method, and digital diffractograms there is a difference between central and peripheral parts. Localized near the center portion has a radial-ring structure of the location of diffraction maxima and has the self-similarity inherent for any fractal objects, while the having no self-similarity peripheral part characterized by an equidistant arrangement of

diffraction maxima along the defined number of radial directions (rays). For the first time this fact drew the attention of the authors of article [2] devoted to the study of optical Fraunhofer diffraction on the classic Koch snowflake, where they are to refer to the central and peripheral parts used the terms "fractal part" and "lattice part" and linked the appearance of the latter with the fact that in a two-dimensional set of elements forming the fractal, one can select a one-dimensional diffraction gratings consisting of equally oriented elements (eg. segments). Later this mechanism was discussed in detail on the example of the family of the generalized process of the Koch fractals [14, 15].

Although in all the above cases it was possible to speak about the good correspondence between the experimentally observed and digital diffractograms, it is almost not studied the questions remain whether there are differences between real and digital diffraction pattern and what conditions to meet their identity needs to satisfy the procedure for digitizing and processing the pictures of fractals. The aim of this work is to answer these questions.

4. INVESTIGATION RESULTS AND DISCUSSION

The main attention was paid to studying the influence of the parameter p equal to the ratio of the dimensional size of the smallest element of prefractal to the period of the grid, on the degree of compliance of a digital diffractograms to the experimentally observed diffractograms

patterns at different values of p which in the calculations was varied by changing the period of the grid for the same computer-generated raster image of the selected prefractal. If the value of p is close to one, only fractal part of the real diffraction patterns is displayed on the digital diffractogram; with increasing of p the lattice part appears, which with the growth of p monotonically approaches to the existing in the real diffraction pattern. We studied the fractals of two types, in which the smallest element ("seed") is either a square or a line segment.

Let's start the presentation with two described in detail in [11] fractals L -systems with the "seed" in the form of a square [16-18]; then – fractals $LS1$ and $LS2$. Algorithms of construction of these fractals can be represented using the following recurrence relations, showing successive transformation of a single seed of a square on the complex plane [11]. Note that these algorithms contain a transform that uses only integer translation of the object along the real and (or) the imaginary axis, and turns only at angles that are multiples of $\pi/2$.

If one selects the orientation of the coordinate system on the complex plane so that the imaginary axis was directed horizontally to the right and the real axis is horizontal down, and place a single seed box (set $Z^{(0)}$) in the first quadrant (the coordinates of the vertices are $(0,0)$, $(0,i)$, $(1,i)$, and $(1,0)$), then the $LS1$ prefractal any order (generation) $Z^{(n)}$ obtained by operation of merging sets \cup with the help of recursion relations [11]:

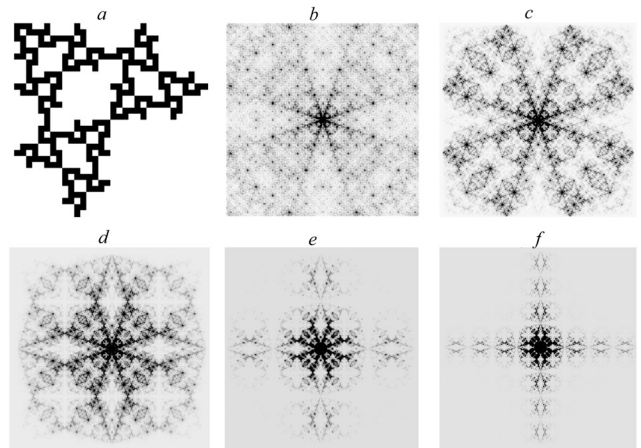


Fig. 2. Prefractal $LS1$ of 4th-generation picture (a) and digital diffractograms for prefractal of 7th generation with values of p equal to 0.5 (b), 1.0 (c), 2.0 (d), 4.0 (e) and 8.0 (f).

$$Z^{(n+1)} = Z^{(n)} \cup (iZ^{(n)} + (1+i)2^n) \cup (-iZ^{(n)} + (1+i)2^n). \quad (1)$$

For a fractal $LS2$ chain of consecutive transformations for set in a form of a single square seed is given by the expressions [11]

$$Z^{(n+1)} = Z^{(n)} \cup (-Z^{(n)} + (2+i)2^n) \cup (-Z^{(n)} + (1+2i)2^n). \quad (2)$$

Fig. 2a shows an image of prefractal $LS1$ of the 4th generation; digital diffractogram for prefractal of 7th generation with the parameter p values equal to 0.5, 1.0, 2.0, 4.0 and 8.0 are shown in Fig. 2b-2f, respectively. It is seen that the structure of the digital diffraction patterns is very strongly dependent on the parameter p , especially at small values of it (see Fig. 2b), when there is a stark contrast to the experimentally obtained for prefractal of the same generation diffraction pattern, shown in **Fig. 3**. Nevertheless, even at $p = 1$ (the cell size of the grid functions is equal to the size of the smallest element of prefractal), the digital diffraction pattern (Fig. 2c) clearly displays fractal part, although lattice part is completely absent. This result does not depend on the prefractal generation

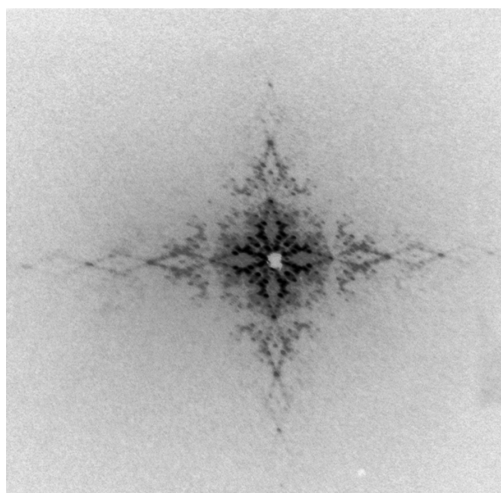


Fig. 3. Experimental diffraction pattern for prefractal LS1 of 4th-generation.

number; but for high generations details of the fractal part of the digital diffractogram manifest more clearly.

At $p \geq 2$ on digital diffractogram appears lattice part, which increases with a further decrease of cell size of the grid functions with respect to the size of the smallest element of prefractal (Fig. 2d-f). Comparison digital diffraction pattern

(Fig. 2f) with the experimental one (Fig. 3) shows that they coincide with a high degree of accuracy. About this testify and close-up (in two different scales) central part pictures of digital and experimental diffraction patterns, which are given next in Fig. 4a,c and Fig. 4b,d.

Similar results were obtained for a fractal LS2, the picture of which for prefractal of 4-th generation are shown in Fig. 5a and digital diffractogram for prefractal of 9-th generation at $p = 1$ – in Fig. 5b and at $p = 4$ – in Fig. 5c. Experimental diffraction pattern for

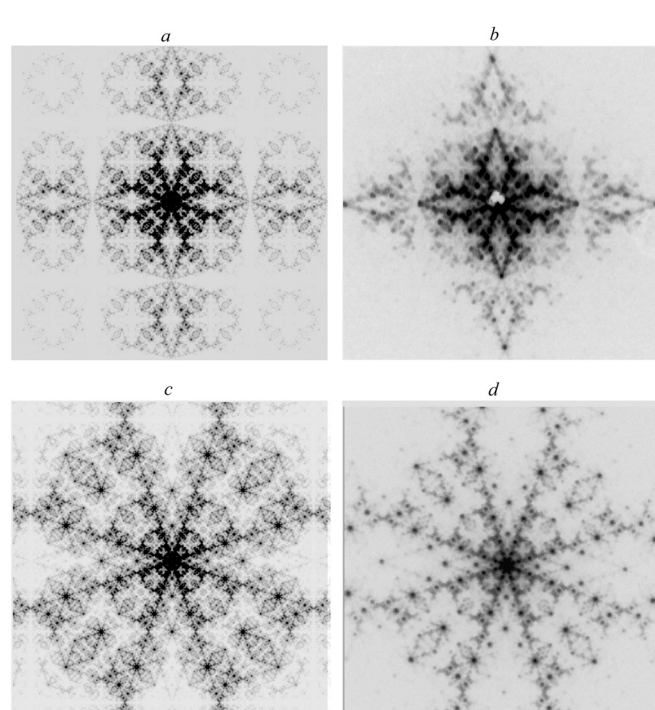
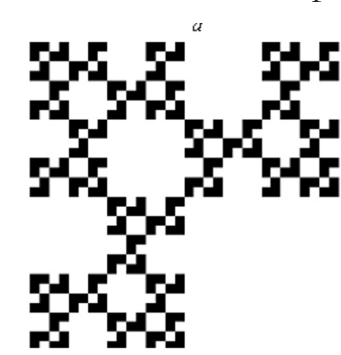


Fig. 4. Close-up (in two different scales) pictures of central part of the digital (a,c) and experimental (b,d) diffraction patterns from prefractal LS1 of 7th-generation.

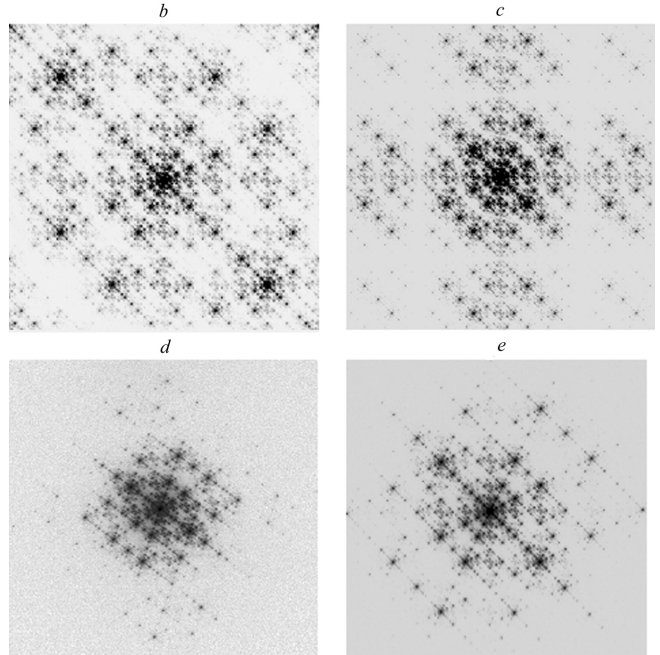


Fig. 5. Picture of prefractal LS2 of 4th-generation (a), digital diffractograms for prefractal of 9th generation with values of equal to 1.0 (b) and 4.0 (c), and picture of the experimental diffractogram for prefractal of 9th generation in two different scales (d - general appearance, e - close-up central part).

prefractal of 9-th generation is shown in two different scales in Fig. 5d (general appearance) and Fig. 5e (close-up) are well consistent with the calculated at $p = 4$.

The comparison of experimental and digital diffraction patterns was conducted and for other objects: Vicsek fractal, Sierpinski carpet and Koch snowflake. Fig. 6a shows the image of 3rd generation Vicsek prefractal, and Fig. 6b and Fig. 6c – the digital diffractograms of 5th generation prefractal for $p = 1$ and for $p = 8$.

Experimental diffraction patterns for prefractal of 5-th generation shown in two different scales in Fig. 6d (general appearance) and Fig. 6e (close-up) are in good agreement with the calculated for $p = 4$. Sierpinski carpet of the 3rd generation is shown in Fig. 7a, and Fig. 7b and Fig. 7c presents the calculated diffraction pattern for this prefractal of 4th generation with $p = 1$ and $p = 9$, respectively. Experimental diffractogram for prefractal of the same generation at two different scales is shown in Fig. 7d

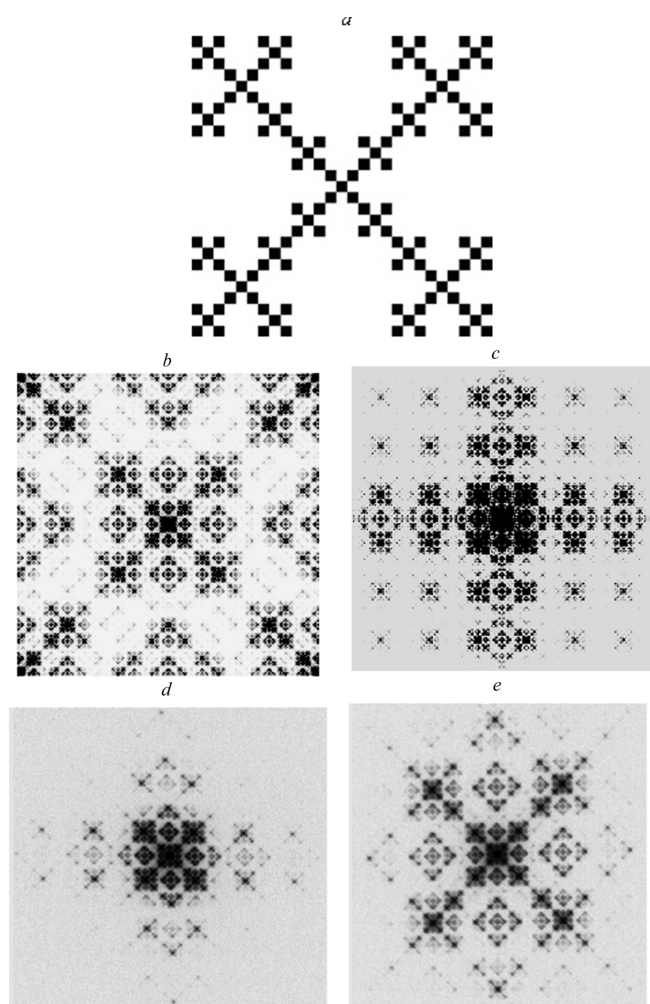


Fig. 6. Picture of Vicsek prefractal of 3rd-generation (a), digital diffractograms for prefractal of 4th generation for $p = 1$ (b) and $p = 9$ (c), and picture of the experimental diffractogram for prefractal of 4th generation in two different scales (d - general appearance, e – close-up central part).

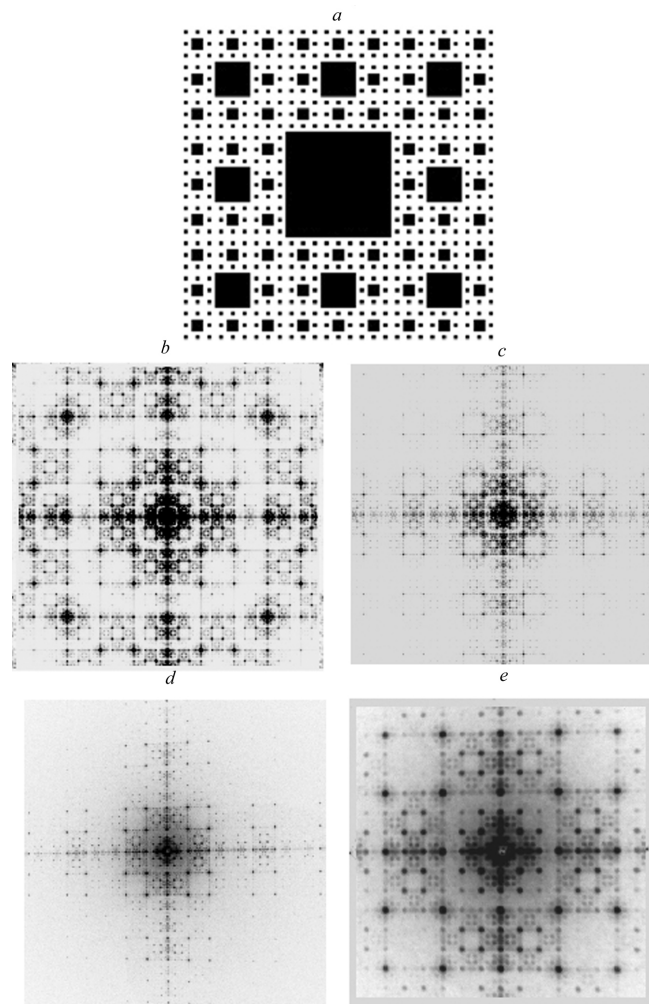


Fig. 7. Picture of Sierpinski carpet of the 3rd generation (a), digital diffractogram for prefractal of 5th generation for $p = 1$ (b) and $p = 9$ (c), and picture of the experimental diffractogram for prefractal of 5th generation in two different scales (d - general appearance, e – close-up central part).

(general appearance) and Fig. 7e (close-up central part). Experimental and

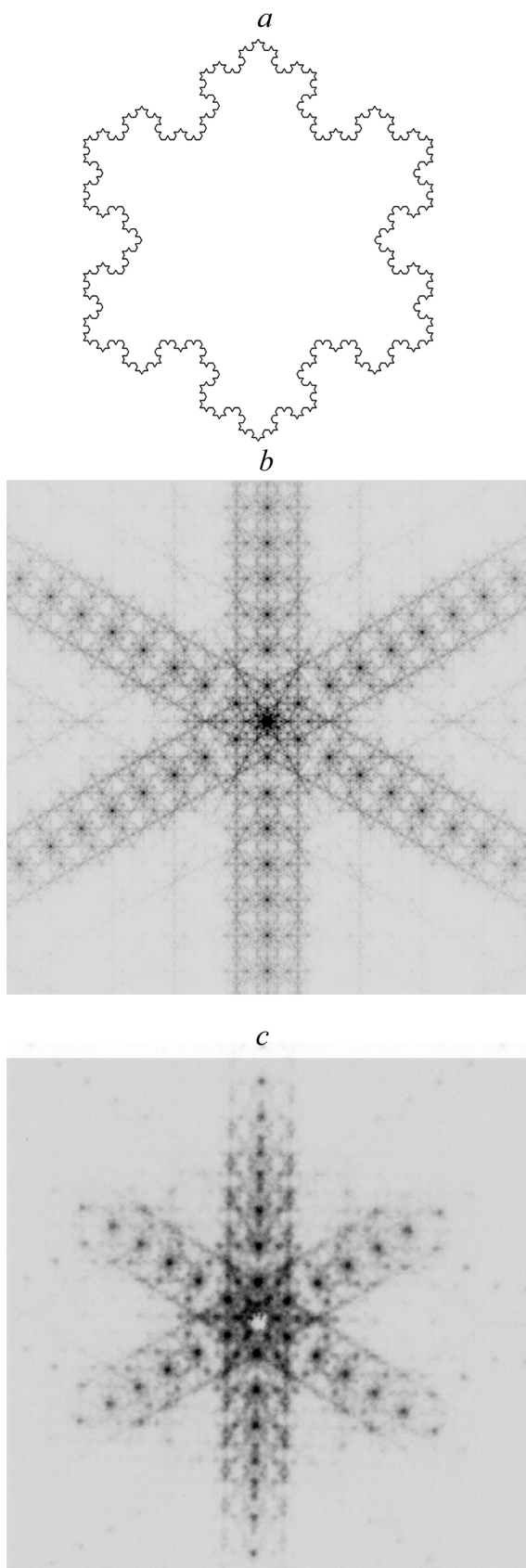


Fig. 8. Koch snowflake of the 4th generation picture (a) and digital (для p) (b) and experimental (c) diffraction patterns.

digital diffractograms for 5th generation Vicsek prefractal with $p = 8$ and for 4th generation Sierpinski carpet with $p = 9$ fully correspond to each other.

The Koch snowflake is fundamentally different from the discussed above fractals, the fact that the element of minimal size in it is not a square, but a segment of line which cannot be displayed by one cell of the grid functions and to adequate representation it in calculations, one needs more cells. Therefore, in consideration of diffraction by the Koch snowflake by using the fast Fourier transform it should be automatically established the condition $p \geq 2$, under which the digital diffraction pattern is in good agreement with experimental one and lattice part is present. Almost coincident with each other digital (at $p = 20$) and experimental diffraction patterns for represented in **Fig. 8a** the 4-th generation Koch snowflake, are shown in Fig. 8b and Fig. 8c, respectively.

5. CONCLUSION

Analysis of all the obtained experimental and digital diffraction patterns showed that with increasing generation number of prefractal per unit leads to enlarging of fractal part by m times, where m is the scale factor. Additional confirmation of this conclusion was obtained in [14], where was obtained the digital diffractogram for the generalized Koch curve with an arbitrary apex angle α , scale factor of which varied from 2 (when $\alpha \rightarrow 0^\circ$) to 4 (when $\alpha \rightarrow 180^\circ$). For fractals LS1 and LS2, the scaling factor is 2, and for a fractal

of Vicsek, Sierpinski carpet, and classic Koch snowflake equals 3. The result for the Koch snowflake is the same as that found in [2], the authors relied not only on the results of the experiments, but also on rigorous analytical calculations. In the limit, as the generation number of prefractal leads to infinity, the fractal part should completely displace the lattice.

The results of investigations of diffraction on different fractal objects show that if the condition $p \geq 2$ is met when the size of the smallest element of prefractal more than two times the period of the grid functions obtained by fast Fourier transform digital diffraction pattern are in good agreement with the experimental ones. Received any way diffractograms have not only fractal, but also the lattice part, which arises from the fact that the generation number of prefractal always bounded above. When $p < 1$ the digital pattern is far from experimentally observed, and for values $1 \leq p < 2$ digital methods correctly reflect only the central (fractal) part.

REFERENCES

1. Alain C, Cloitre. M. Phys. Rev. B, 1986, 33(5): 3566-3569.
2. Uozumi J, Kimura H, Asakura T. J. Mod. Optics, 1990, 37(6): 1011-1031.
3. Sakurada Y, Uozumi J, Asakura T. Opt. rev., 1994, 1(1): 3-7.
4. Uozumi J, Kimura H, Asakura T. J. Mod. Optics, 1991, 38(7):1335-1347.
5. Sakurada Y, Uozumi J, Asakura T. J. Optics. A: Pure Appl. Optics, 1992, 1: 29-40.
6. Chabassier G, Angéli B, Heliodore F, Le Mehauté A. J. Optics. A: Pure Appl. Optics, 1992, 1: 41-54.
7. Bo Hou, Gu Xu, Wen W, Wong GK L. *Appl. Phys. Lett.*, 2004, 85(25): 6125-6127.
8. Arzamastseva GV, Evtikhov MG, Lisovsky FV, Lukashenko LI. *Trudy XIX Mezhdunarodnoi shkoly-seminara "Novye magnitnye materialy microelektroniki"*, Moscow, 2004, p. 632-634 (in Russ.).
9. Arzamastseva GV, Evtikhov MG, Lisovsky FV, Mansvetova EG, Temiryazeva MP. *ZhETP*, 2008, 134(2): 282-290. (in Russ.).
10. Arzamastseva GV, Evtikhov MG, Lisovsky FV, Mansvetova EG. *Izv. RAS, ser. fiz.*, 2010, 74(10):1430-1432 (in Russ.).
11. Arzamastseva GV, Evtikhov MG, Lisovsky FV, Mansvetova EG. *Radioelektronika. Nanosistemy. Informatsionnye Tekhnologii (RENSIT)*, 2012, 4(2): 93-107 (in Russ.).
12. Arzamastseva GV, Evtikhov MG, Lisovsky FV, Mansvetova EG. *Electromagnitnye volny i electronnye sistemy*, 2012, 17(7): 29-32 (in Russ.).
13. Arzamastseva GV, Evtikhov MG, Lisovsky FV, Mansvetova EG. *Electromagnitnye volny i electronnye sistemy*, 2012, 17(7): 48-58 (in Russ.).
14. Arzamastseva GV, Evtikhov MG, Lisovsky FV, Mansvetova EG. *RENSIT*, 2016, 8(1): 81-90 (in Russ.).
15. Arzamastseva GV, Evtikhov MG, Lisovsky FV, Mansvetova EG. *RENSIT*, 2016, 8(2): 207-214 (in Russ.).

- 16.Lindermayer A. J. *Theor. Biol.*, 1968,
18(3):280-299.
- 17.Lindermayer A. J. *Theor. Biol.*, 1968,
18(3):300-315.
- 18.[http://lcni.uoregon.edu/~dow/
Geek_art/Binary_fractals/Binary_
fractal_images.html](http://lcni.uoregon.edu/~dow/Geek_art/Binary_fractals/Binary_fractal_images.html).

GRAFENIKA [GRAPHENICS]. RUSSIAN GUBIN'S SEMINAR (MOSCOW)

Vladimir I. Grachev

Editorial Board of "Radioelektronika. Nanosistemy. Informatsionnue tekhnologii (RENSIT)", <http://www.rensit.ru>
Moscow 125009, Russian Federation
grachev@cplire.ru, vigrach@yandex.ru

Abstract. The information on the seminar "GRAFEN: MOLECULES AND 2D-CRYSTAL", which was held since 2011 in Moscow, is presented. The seminar became the basis of the first graphene conference in Russia. By now the seminar has completed its work.

Keywords: seminar, graphene, molecule, crystal, production methods, graphene physics and chemistry, graphene-based devices, carbon nanoelectronics

PACS: 01.10 Fv

RENSIT, 2017, 9(2):230

DOI: 10.17725/rensit.2017.09.230

Russian Seminar "GRAPHENE: MOLECULE AND 2D-CRYSTAL (material, physics, chemistry, electronics, photonics, biomedical applications)" under the direction of prof. SP Gubin operates from November 2011. Seminar sessions are held once a month, mainly in the boardroom VNIAlmaz in Gilyarovskogo str., 65. The seminar is supported by LLC "AkKoLab". Programms of seminars are available at <http://www.akkolab.ru>. The seminar organizers see it as a discussion platform to discuss new ideas and concepts, review the results and the exchange of experience of researchers in the booming grafenika - an interdisciplinary field of modern science. The seminar was attended by officials from various scientific institutions of Moscow and Moscow region - Kurnakov Institute of General and Inorganic Chemistry RAS, Nesmeyanov Institute of Organoelement Compounds of RAS, Semenov Institute of Chemical Physics RAS, Kotel'nikov Institute of Radio Engineering and Electronics RAS, Institute of Microelectronics Technology RAS, Institute of Problems of Chemical Physics RAS, Landau ITP RAS, National Research Centre "Kurchatov Institute", Moscow State University Faculties of Chemistry and Physics, Moscow Institute of Physics and Technology, National Research Nuclear University "MEPhI", People's Friendship University of Russia, LLC "AkKoLab", Open Joint Stock Company (JSC) "VNII Almaz", LLC "Karbonlayt", JSC NIIGrafit and others, as well as invited members of scientific institutions in Russia, Commonwealth of Independent States (CIS) and foreign countries. The audience for each session - about fifty participants. In the four-hour meeting with a break heard and discussed the 3-4 reports, news review and submitted poster presentations. The journal RENSIT is published semi-annual reports of this seminar: list of reports indicating affiliated authors and submitted abstracts.

In 2015, on the basis of the seminar, the first All-Russian conference "GRAFEN: MOLECULES AND 2D-CRYSTAL" was proposed and organized with international participation, largely assuming the functions of the seminar and extending its audience to the all-Russian one. The conference is registered in the Russian Foundation for Basic Research (RFBR) under the Government of the Russian Federation as a periodic, every 2 years, on the basis of the A.V. Nikolaev Institute of Inorganic Chemistry of Siberian Branch of the Russian Academy of Sciences.

Radioelectronics. Nanosystems. Information Technologies (abbr. RENSIT)

Certificate El. no. FS77-60275 on 19.12.2014 of the Ministry of Telecom and Mass Communications of Russian Federation, Moscow

ISSN: 2414-1267online. [Http://www.rensit.ru](http://www.rensit.ru). Publisher - Vladimir I. Grachev. 2017, 30 Dec.

Computer printing, page-proofs, graphics, photos of work - the editors RENSIT.